universität innsbruck

Realization of a Zeeman Slower Based on Permanent Magnets as a Source of Cold Dysprosium Atoms

Niclas Höllrigl, 11777230
Innsbruck, May 2024

Masterarbeit

eingereicht an der Universität Innsbruck, Fakultät für Mathematik, Informatik und Physik zur Erlangung des akademischen Grades

Master of Science

Masterstudium Physik

Betreuer: Univ.-Prof. Dr. Rudolf Grimm und Dr. Emil Kirilov
Institut für Experimentalphysik
Fakultät für Mathematik, Informatik und Physik

Abstract

This thesis reports on the design, simulation and realization of a compact Zeeman Slower for dysprosium (Dy) that is based on permanent magnets. For the lanthanide series of elements, such a device has not yet been realized except for ytterbium. Dysprosium is a highly magnetic element whose long-range and anisotropic interactions make it an excellent candidate to perform quantum simulations of exotic spin models. For a new generation of experiments we require the complexity of the immanent cooling and trapping stages to be considerably reduced for ease of maintenance, and reduction of points of failure. For this purpose, we engineered a Zeeman slower that can easily be mounted, does not rely on electric currents and, thus, does not require water cooling while being twice as compact as our present setups. In particular we present the design process, which was primarily based on numeric optimization, the engineering techniques used to realize the device and its final characterization. This is accompanied by a discussion of the utilized laser systems, optical setups and stabilization schemes. During the development of the apparatus, attention was already paid for being able to adapt it to varying specifications and other species. The magnetic field could be engineered to closely resemble the corresponding theoretical calculation. In conducting a stand-alone characterization experiment, we observe a clear signature of decelerated atoms, demonstrating the functionality of our design. Despite not reaching the desired extraction velocity due to limitations of the vacuum apparatus, we successfully overcame numerous technical challenges. These advancements pave the way for the development of similar devices that can be integrated more compactly inside vacuum systems, and therefore offering promising prospects for future experiments.

Kurzfassung

Diese Arbeit befasst sich mit dem Entwurf, der Simulation und der Realisierung eines hochkompakten Zeeman-Slowers für Dysprosium (Dy), der auf Permanentmagneten basiert. Ein derartiger Aufbau wurde für schwere Elemente der Gruppe der Lanthanide bisher lediglich für Ytterbium demonstriert. Dysprosium ist ein sehr stark magnetisches Element. Seine weitreichende und anisotropische Dipol-Dipol Wechelwirkung macht es zu einem idealen Kandidaten für die Quantensimulation exostischer Spinmodelle. Für eine neue Generation von Experimenten wollen wir die Komplexität der grundlegenden Kühl- und Fallenmechanismen erheblich reduzieren, um die Wartung zu erleichtern und Fehlerquellen auszuschließen. Daher haben wir einen Zeeman-Slower entwickelt, der sich leicht aufbauen lässt und nicht auf elektrischen Strömen basiert. Dieser Apparat verzichtet somit auch auf eine aufwändige Wasserkühlung und ist zusätzlich nur halb so groß wie bereits bestehende Aufbauten. Wir beschreiben insbesondere den Entwicklungsprozess, der sich stark auf numerische Optimierungsmethoden stützt, sowie die zur Realisierung des Geräts grundlegenden technischen Verfahren und seine abschließende Charakterisierung. Darüber hinaus werden die verwendeten Lasersysteme, optischen Aufbauten und Stabilisierungsverfahren diskutiert. Es wurde bei der Entwicklung des Zeeman-Slowers darauf geachtet, dass das Verfahren einfach an abweichende Spezifikationen und sogar andere Elemente angepasst werden kann. Das magnetische Feld konnte in guter Übereinstimmung mit der theoretischen Berechnung realisiert werden. Bei der Durchführung eines eigenständigen Experiments zur Charakterisierung des Aufbaus beobachten wir eine eindeutige Signatur abgebremster Atome, was die Funktionalität unseres Designs klar zeigt. Obwohl die gewünschte Extraktionsgeschwindigkeit aufgrund von Limitierungen der Vakuumapparatur nicht erreicht wird, haben wir zahlreiche technische Herausforderungen gemeistert. Diese Fortschritte ebnen den Weg für die Entwicklung ähnlicher Geräte, die sich noch kompakter in Vakuumsysteme integrieren lassen und daher vielversprechende Aussichten für zukünftige Experimente bieten.

Contents

1. Introduction

1.1. General Background

The quantum nature of matter is complex and fundamentally different from our classical understanding, which makes it hard, if not impossible, to explore it by classical means. This challenge was notably articulated by Richard Feynman during a conference talk in 1981, where he famously shared his pioneering thoughts on the fundamental limitations of simulating a quantum mechanical nature with classical computers [1]. It was just at the same time as Feynman gave his speech that laboratories in the USSR first observed the deceleration of beams of neutral atoms by means of a counterpropagating laser beam [2]. Soon after, by adding a spatially varying magnetic field, American physicists demonstrated the first Zeeman slower (ZS) [3], which was followed by the development of numerous new techniques for laser cooling and trapping of neutral atoms, ultimately leading to the observation of the first Bose-Einstein condensates (BEC) of rubidium [4], sodium [5] and possibly lithium [6, 7] more than ten years later. These were only the initial milestones for a whole new field in the domain of atomic, molecular and optical (AMO) physics, the study of ultracold quantum gases. Since then, a total of fifteen different bosonic species have been brought to quantum degeneracy. This includes erbium [8], thulium [9] and europium [10], to name the most recent additions. Apart from that, a vast interest for experiments on degenerate gases of fermions, and various mixtures of species with fermionic and/or bosonic statistics has evolved in the scientific community [11–15]. Given their tunability of trapping geometry and interactions, wide selection of bosonic and fermionic elements, scalability and accessibility of internal degrees of freedom, ultracold quantum gases provide a rich platform for the investigation of intriguing many-body phenomena and exotic phases of matter that also have their analogues in other physical systems which elude our direct observation. Prominent examples of such systems include, but are not limited to the domain of condensed matter, where the understanding of high-temperature superconductivity is a major scientific goal [16].

The kind of interactions within the system generally depends on the choice of atomic or molecular species being used by an experimentalist. In the case of alkali and alkaline-earth elements the physics is governed by short-ranged and isotropic contact interaction, the strength of which can be well controlled, e.g. by tuning an external

magnetic field across a Feshbach resonance [17]. When working with highly magnetic lanthanide atoms, the experimental toolbox is extended to long-range and anisotropic dipole-dipole interactions. In such dipolar quantum gases, the control over this new kind of interaction allows for the observation of a roton mode in the dispersion relation, droplets and supersolid states [18]. Alternative systems with strong dipole moment include atoms in highly excited Rydberg states [19] and diatomic molecules [20].

The physics mediated by dipolar interactions are particularly well suited to realize several theoretical models for magnetic systems, such as the Hubbard, Heisenberg or Ising model [21, 22]. To explore these models in the context of ultracold systems, the atoms are loaded in an optical lattice, generated by superimposed laserbeams. This results in a periodic trapping potential with tunable depth, spacing and geometry. In recent years, the evolution of optical lattice experiments has been accompanied by the development of quantum gas microscopes (QGM) with single lattice-site resolution [23, 24]. Although the technical difficulties to resolve lattice spacings on the order of optical wavelengths are noteworthy, the prospects of being able to image the dynamics of such an artificial crystal in-situ, makes this research field grow rapidly. In addition to the development of microscopes with ever higher resolution, the magnification of the density distribution by means of matter wave optics has emerged as a promising technique for enhanced imaging [25].

In the NewLanD experiment at the Institute for Quantum Optics and Quantum Information (IQOQI) in Innsbruck, such a new apparatus for simulating quantum magnetism in optical lattices has been constructed [26]. For us, the element dysprosium (Dy) is a favourable choice. First and foremost, Dy possesses the largest magnetic moment among all elements and therefore provides strong dipolar interactions. Also, the set of atomic energy levels is very rich, as it is commonly the case for the lanthanide family due to their special arrangement of electronic orbitals. This allows for many transitions with variable properties that can be used for laser cooling, trapping and fast imaging. Finally, we plan on using a set of nearly degenerate states of opposite parity to map the many body long range dipole-dipole interaction (DDI) onto a dressed degenerate isospin. The dressing and additional parity mixing is achived by a microwave coupling of the above states. Once projected onto the isospin, the DDI has both magnetic and electric character [27]. This prospect is in its accessibility, so far, unique to dysprosium and is predicted to further enhance the interaction strength and possibly allow for the simulation of the XYZ Heisenberg model with the rates of its terms being highly tunable and lattice dependent.

1.2. Motivation

As the degree of control we have over various systems of ultracold atoms grows steadily, so does the complexity of each new experiment. It is therefore an ongoing effort to identify possibilities to simplify, miniaturize and optimize a given setup. In the preceding section, we presented a wide range of experiments with a variety of scientific prospects. However, their underlying principle is similar. Initially, the species of interest, in either solid or liquid form, has to be brought into the gaseous phase. Only then the atoms can be trapped, cooled, and eventually experimented on. Thus, a source of hot atomic vapour is the starting point of any such experiment. Using dispensers for this purpose is a convenient method used for alkali elements. For elements with a high melting point, e.g. erbium or dysprosium, however, a high-temperature oven has to be used. The mean velocity of the gaseous atoms after emission from this source is typically on the order of hundreds of $\mathrm{m\,s^{-1}}$. To to shift the velocity distribution more towards trappable velocities on the order of tens of $\mathrm{m\,s^{-1}}$, either a Zeeman slower or two-dimensional magneto optical trap (2D MOT) is regularly used. For Dy, loading from a 2D MOT of Dy has only recently been demonstrated [28]. Instead, we will be focusing on the simplification of common Zeeman slower setups.

The working principle of a Zeeman slower is based on resonant light scattering from a counterpropagating laser beam. A magnetic field is used to counteract the changing Doppler shift during deceleration and is usually generated by a set of coils, i.e., a tapered solenoid through which a high electric current is passed. This generates heat that needs to be dissipated in some way. In his Nobel lecture, William D. Philips told the anecdote that the first Zeeman slowers to ever be built used wet towels and fans for cooling [29]. Since then these devices have undergone a steady development with modern setups featuring internal water cooling and good control over the magnetic field profile [30]. Nevertheless, the requirement for high currents and water cooling imposes the need for additional powersupplies, hoses, and devices for control, thus introducing numerous points of failure (PoF) and complexity to the experiment. An approach to abandon the usage of tapered solenoids and replace them with permanent magnets has first been demonstrated for an atomic clock with strontium [31] with arrays of adjustable magnets that could be tuned individually. A more recent apparatus for ytterbium uses a fixed array of magnets with various dimensions [32]. For these and similar setups the magnetic field vector is pointing transversal to the direction of propagation of the atoms, implicating that only half of the incident light can contribute to the slowing transition. For species that require large amounts of laser intensity, this can become a major problem. Thus, longitudinal field Zeeman slowers were soon proposed [33] and realized [34].

1.3. Outline

This thesis reports on the design, simulation and characterization of a new kind of longitudinal Zeeman slower for dysprosium, realized with permanent magnets. In Chapter 2, we discuss general properties of Dy and introduce some of its intriguing prospects in the context of the NewLanD experiment in Innsbruck. This is followed by Chapter 3 where we give a detailed description of the Master project itself. This includes the design, simulation and setup of a permanent magnet Zeeman slower for Dy. The apparatus is then experimentally characterized in Chapter 4. This also includes the optics, lasers and locking setups that have been built. We conclude in Chapter 5 and provide additional information in the Appendix.

2. Atomic Dysprosium and the NewLanD Experiment

The chemical element dysprosium (Dy) is a soft, silvery-gray colored metal with atomic number 66. It is a member of the lanthanide group[1] in the periodic table of elements and was discovered in Paris 1886 by the French chemist Paul-Émil Lecoq de Boisbaudran through spectral analysis of an impure holmium sample. The new element was named dysprosium, from the Greek *dysprósitos* meaning 'hard to get at', due to the difficulties one had to overcome to separate pure dysprosium from erbium and holmium. The natural abundance of Dy within the earths crust is on the order of $5(1)\,\mathrm{mg\,kg^{-1}}$. There, it is mostly found in xenotime, gadolinite, euxenite, and monazite minerals. Due to its relatively high cross section for thermal neutrons, Dy is mainly used as detector material for measuring neutron flux in nuclear reactors. It is also a component of special alloys for new magnetic materials, which are of particular interest for the recently emerging renewable energy market [35, 36].

In our field of ultracold quantum gases, Dy is outstanding due to its ground state magnetic moment being the largest of all known elements beside holmium. In addition to that, Dy possesses a rich atomic energy spectrum with convenient transitions for laser cooling and trapping. These properties made it the ideal candidate for dipolar physics in magnetic quantum gases [18], ever since the first Bose-Einstein condensate (BEC) of Dy has been achieved in 2011 [37]. The complex level scheme of Dy also includes a pair of nearly degenerate states with opposite parity. Said feature is currently the center of interest for the NewLanD experiment as it promises the attainability of a mixed state possessing both, a high magnetic and electric dipole moment with high tunability [27].

This chapter aims at providing a solid reference on the general properties of Dy, followed by a discussion of the atomic energy spectrum. This includes the most common transitions for cooling and trapping as well as the doublet of nearly degenerate states of opposite parity. Lastly, we give an overview on how the NewLanD experiment is expected to utilize said fruitful feature.

[1] Also referred to as rare-earth elements although the abundance of many lanthanides is not particularly low compared to other groups of elements [35].

2.1. General Properties

The nucleus of dysprosium is composed of 66 protons and a number of neutrons varying between the seven naturally occurring stable isotopes listed in Tab. 2.1. Taking the weighted average over the mass of all stable isotopes yields a value of 162.5 u. The high fraction of 0.4379(6) fermionic particles present in a sample of dysprosium makes the investigation of fermionic quantum gases feasible. Due to their non-vanishing nuclear spin, these fermionic isotopes feature hyperfine structure and isotope shift. Our work focuses primarily on the most abundant bosonic ^{164}Dy isotope. Dysprosium melts at 1407 °C and boils[2] at 2562 °C. It is thus solid at standard conditions with a density of 8.56 g cm^{-3} at 20 °C [35]. Proposed by Ref. [39] and, more recently, pointed out by Refs. [40] and [41], a phenomenological description of the vapor pressure as a function of temperature for many solids is given by the Antoine equation,

$$\log_{10}(p_{\mathrm{vap}}) = A - \frac{B}{C+T}, \tag{2.1}$$

where A, B and C are empirical parameters and dependent on the material of interest. By applying this relationship to the vapor pressure measurements shown in Fig. 2.1, for dysprosium, one finds $A_{\mathrm{Dy}} = 6.919(5)$, $B_{\mathrm{Dy}} = 1.017(2) \times 10^4\,\mathrm{K}$ and $C_{\mathrm{Dy}} = -2.36(2) \times 10^2\,\mathrm{K}$. The pressure is hereby given in units of hPa. A comparison of the vapor pressure of Dy and other elements that have recently been used in atomic physics experiments, shows that similar to erbium and chromium, dysprosium imposes challenging requirements on the oven temperature. To attain a typical gas pressure on the order of a few Pa, one thus requires temperatures exceeding 1200 K.

Table 2.1.: List of all seven fermionic and bosonic dysprosium isotopes found in nature. All data has been taken from Ref. [43].

Isotope	Mass (u)	Abundance		Nuclear Spin	Statistics
^{156}Dy	155.924 278	5.6(3)	$\times 10^{-4}$	0	boson
^{158}Dy	157.924 405	9.5(3)	$\times 10^{-4}$	0	boson
^{160}Dy	159.925 194	2.329(18)	$\times 10^{-2}$	0	boson
^{161}Dy	160.926 930	0.1889(4)		5/2	fermion
^{162}Dy	161.926 795	0.2548(4)		0	boson
^{163}Dy	162.928 728	0.2490(4)		5/2	fermion
^{164}Dy	163.929 171	0.2826(6)		0	boson

[2] The exact boiling point of Dy is still under debate with values ranging from 2560 °C to 2600 °C. For a comparison, see Ref. [38].

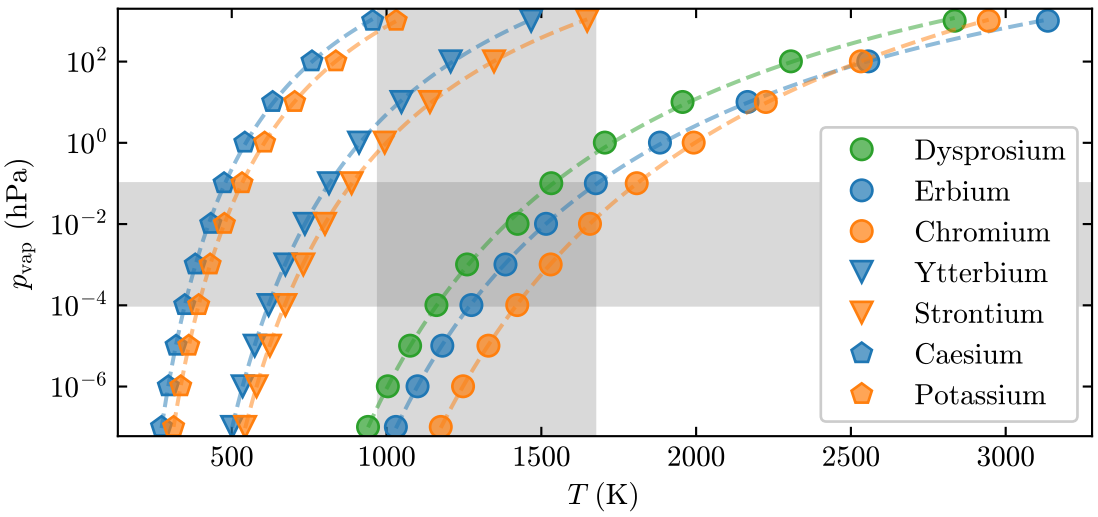

Figure 2.1.: Vapor pressure as a function of temperature for a variety of elements. The vertical gray shaded area represents the range of use of our effusive oven, while the horizontal gray shaded area shows the typical vapor pressure for ultracold atom experiments. The data points have been taken from [42]. A fit of the Antoine equation, as in Eq. (2.1), has been applied and is shown as dashed line for each element. The respective results for dysprosium are given in the main text.

2.1.1. Ground-State Configuration

It is often found among the lanthanides that the valence electrons are submerged under filled orbitals of higher principal quantum number. This so-called submerged shell configuration leads to a complex level scheme and high orbital angular momentum. These features are particularly pronounced in Dy. By assigning the 66 Dy electrons according to the Aufbau principle, one finds that the electronic ground-state of dysprosium is given by

$$\left[1\,\mathrm{s}^2\,2\,\mathrm{s}^2\,2\,\mathrm{p}^6\,3\,\mathrm{s}^2\,3\,\mathrm{p}^6\,3\,\mathrm{d}^{10}\,4\,\mathrm{s}^2\,4\,\mathrm{p}^6\,4\,\mathrm{d}^{10}\,5\,\mathrm{s}^2\,5\,\mathrm{p}^6\right]\,4\,\mathrm{f}^{10}\,6\,\mathrm{s}^2, \tag{2.2}$$

where we have used standard spectroscopic notation[3]. This term is usually abbreviated as $[\mathrm{Xe}]\,4\,\mathrm{f}^{10}\,6\,\mathrm{s}^2$, where the expression in brackets equals the electronic configuration of the noble gas xenon (Xe). The $4\,\mathrm{f}$ orbital is only partially filled and submerged beneath the $6\,\mathrm{s}$ orbital. The term symbol of the ground state is thus found by applying Hund's rules on that partially filled $4\,\mathrm{f}$ orbital [44] with angular momentum $l = 3$ and 10 valence electrons in the following three steps.

[3]Atomic orbitals are written as nl^e, where n is the principal quantum number, l is the orbital quantum number (for historical reasons $\mathrm{s} = 0$, $\mathrm{p} = 1$ $\mathrm{d} = 2$ $\mathrm{f} = 3$ ...) and e is the number of electrons that occupy the orbital.

1. There exist seven magnetic sublevels, numbered by the magnetic quantum number m, ranging from $m = -3$ to $m = +3$. Each of these states can occupy up to two electrons. The configuration which maximizes the multiplicity $2S + 1$ is energetically favored, with S being the spin quantum number. Thus, the 10 electrons are distributed in such a way that only three of the 7 states are filled with two (paired) electrons whereas four states are only partially filled with so-called unpaired electrons. This corresponds to $S = 4 \times 1/2 = 2$.

2. For a given multiplicity, the unpaired electrons occupy the states such that the angular momentum L is maximized. This is the case when $m_l = \{0, 1, 2, 3\}$ are filled with an unpaired electron. Thus $L = 1 + 2 + 3 = 6$.

3. Eventually, one can determine the total angular momentum quantum number J by considering the interaction of spin and angular momentum, i.e., spin orbit coupling. Given that the $4\,\mathrm{f}^{10}$ orbital is filled to more than half of its capacity, we find $J = |S + L| = 8$.

When written in term notation[4] the Dy ground state thus is a ${}^5\,\mathrm{I}_8$ state.

The high angular momentum quantum number in the dysprosium ground state predominantly gives rise to the exceptionally high magnetic dipole moment μ_m. It can be calculated from the magnetic quantum number m_j of the given state within the total angular momentum manifold, the Landé factor g_j and the Bohr magneton μ_B according to

$$\mu_m = m_j g_j \mu_\mathrm{B}. \tag{2.3}$$

For the fermionic Dy isotopes one needs to replace m_j by m_F and g_j by g_F to account for the non-zero nuclear spin. The equation for calculating the Landé factors g_j and g_f can be found in many textbooks e.g. Ref. [45] and is given by

$$g_j = 1 + \frac{J(J+1) - L(L+1) + S(S+1)}{2J(J+1)}, \tag{2.4a}$$

$$g_f = g_j \times \frac{F(F+1) - I(I+1) + J(J+1)}{2F(F+1)}. \tag{2.4b}$$

In this simple picture, one finds $g_j = 1.2917$. However, it has been pointed out in Ref. [46] that further corrections, namely the Schwinger correction [47, 48], a correction of the spin-orbit interaction as well as relativistic and diamagnetic effects have to be taken into account. Thus, a corrected value of $g_j = 1.2370$ has been suggested. Experimental results [49] yield a value of $g_j = 1.241\,586\,7(10)$, which we

[4] The term symbol is a concise description of the angular momentum quantum numbers of a state. It is written in the form ${}^{2S+1}L_J$, with S, L and J being the quantum numbers defined in the main text.

will subsequently use. For the state with $m_j = 8$, i.e., the fully polarized ground-state in bosonic dysprosium, one obtains $\mu_m = 9.932\,694(8)\,\mu_\mathrm{B}$. For the fermionic Landé factor, given g_j and Eq. (2.4b), we find $g_F = 0.9459708(8)$. For the fully polarized fermionic ground-state with $m_F = 21/2$ this results in a magnetic moment of $\mu_m = 9.932\,693(9)\,\mu_\mathrm{B}$.

2.1.2. Hyperfine Structure and Isotope Shift

The bosonic Dy isotopes do not posses nuclear spin and therefore do not have a hyperfine structure. For the fermionic ^{161}Dy and ^{163}Dy with nuclear spin $|\boldsymbol{I}| = 5/2$, the nucleus has a magnet moment $\boldsymbol{\mu}_I = g_I \mu_\mathrm{N} \boldsymbol{I}$, with the Landé factor of the nucleus g_I and the nuclear magneton $\mu_\mathrm{N} \approx \mu_\mathrm{B}/1836$. The interaction of $\boldsymbol{\mu}_I$ with the total angular momentum of the electron $\boldsymbol{J}$ leads to an effective energy shift, given by

$$\Delta E_{IJ} = A \langle \boldsymbol{I} \cdot \boldsymbol{J} \rangle = \frac{A}{2} \left[F(F+1) - I(I+1) - J(J+1) \right], \tag{2.5}$$

where A is the hyperfine structure constant that is proportional to μ_I/I and the magnetic field B_e produced by the electrons at the position of the nucleus. One can further extend this by also considering the electric quadrupole interaction, which stems from the fact that the nucleus is in fact not a point charge. One then arrives at the final expression

$$\Delta E_\mathrm{HFS} = AK + B \frac{\frac{3}{2}K(2K+1) - I(I+1)J(J+1)}{2I(2I-1)J(2J-1)}, \tag{2.6}$$

with $K = (F(F+1) - J(J+1) - I(I+1))/2$ and B being the quadrupole constant that can be determined experimentally [50, 51].

In addition to that, depending on the number of neutrons, and thus the mass of the nucleus, the atomic energy levels are shifted also. This effect is also found among the bosonic isotopes and can be resolved within the Doppler-free spectroscopy presented in Chap. 4. In Tab. 2.2, the coefficients A, B and the isotope shift $\Delta\nu_m$ relative to the most abundant ^{164}Dy are listed for the ground-state as well as the excited state of the 421 nm cooling transition utilized in this work.

2.2. Atomic Energy Spectrum

Atomic species with submerged shell configuration are known to offer a rich spectrum of excited states and Dy is no exception in this regard. Currently, there are 739 energy levels known of which 406 have even parity and 333 have odd parity [53, 54]. A partial level diagram[5] is shown in Fig. 2.2 for the domain where typical lasercooling transitions are found.

[5] A full level diagram of dysprosium is shown in Fig. A.2

Table 2.2.: List of hyperfine structure constants A and B for the ground-state and excited state of the 421 nm transition for the fermionic ^{161}Dy and ^{163}Dy isotopes. For the 421 nm transition, also the isotope shifts $\Delta\nu_m$ for ^{161}Dy, ^{163}Dy and the bosonic ^{162}Dy isotope, relative to the transition of the most abundant ^{164}Dy isotope are given. The data has been taken from [49, 52].

		A (MHz)	B (MHz)	$\Delta\nu_m$ (MHz)
ground-state	^{161}Dy	−116.2322	1091.5748	
$4f^{10}6s^2$	^{163}Dy	162.7543	1153.8684	
excited state	^{161}Dy	−86.90	1747.4	1635
$4f^{10}6s6p$	^{162}Dy			913.2
	^{163}Dy	121.62	1844.9	616.3

2.2.1. Optical Transitions Suitable for Laser Cooling

Inside the subset of levels accessible within the optical domain there exist only a few cyclic[6] transitions, due to the large number of possible decay channels. This condition, a common feature of lanthanides, made it challenging to apply laser-cooling schemes on Dy. Given the high magnet moment, dysprosium has formerly been magnetically trapped [56], until the discovery of the broad 421 nm transition [57, 58]. Said transition, going from the ground state at $J = 8$ to an excited state at $J' = 9$, can be described as the workhorse of lasercooling of Dy. The excited state has a lifetime of $\tau = 4.94\,\text{ns}$, i.e., photons can be scattered at a rate of $\Gamma = 2\pi \times 32.2\,\text{MHz}$ with the branching ratio to metastable states being 7×10^{-6} [58]. The drawback of such a broad line is the relatively high Doppler temperature of $T_\text{D} = 773\,\mu\text{K}$, which requires further cooling before the atoms can be loaded into an optical dipole trap (ODT). Also, the very high saturation intensity $I_\text{sat} = 562\,\text{W}\,\text{m}^{-2}$ imposes challenging hardware requirements, as high power laser-sources in the blue are only sparsely available. For the deceleration of an atomic beam in a Zeeman slower, however, the 421 nm transition is the best choice for us. For subsequent cooling stages one is advised to either use the 626 nm or 741 nm transitions, which are promising candidates for a narrow line magneto-optical trap (MOT) [59, 60]. The 626 nm transition is an intermediate choice in this regard, with $T_\text{D} = 3.3\,\mu\text{K}$ and $v_\text{cap} = 85\,\text{mm}\,\text{s}^{-1}$. This transition is narrow yet sufficiently strong and thus well-suited for fluorescence imaging spectroscopy for quantifying the velocity distribution of the atomic beam in our experiment. A 741 nm laser-source is currently under construction in the NewLanD experiment. Said transition makes it

[6] We also refer to transitions that are quasi-cyclic, i.e., cyclic on the timescale of the experiment as cyclic.

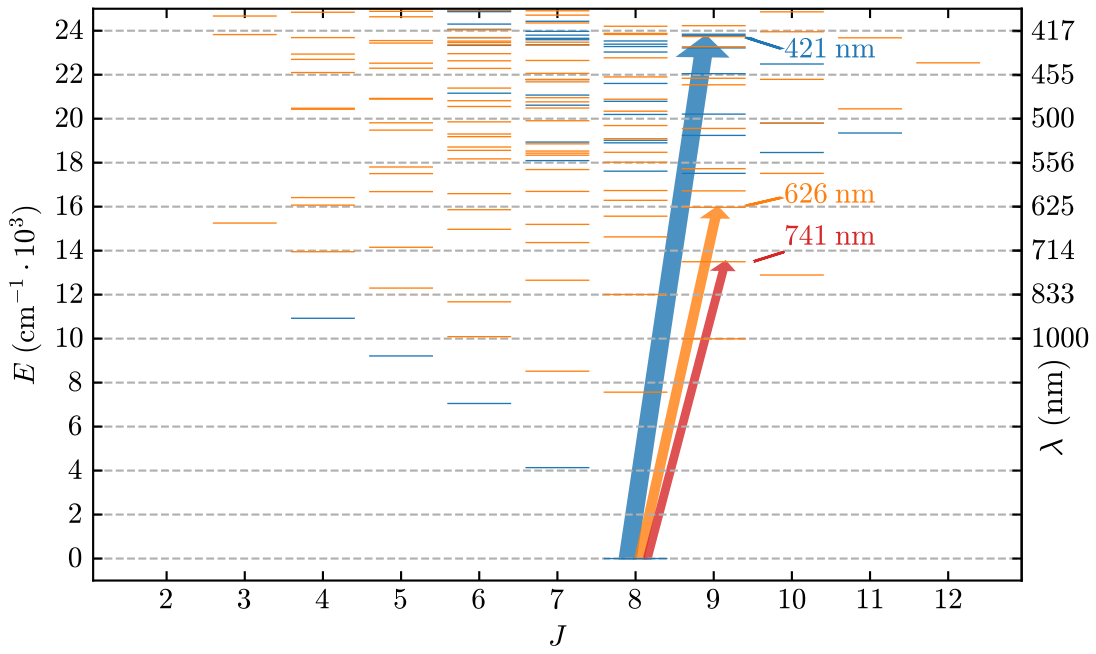

Figure 2.2.: Dysprosium level diagram for the optically accessible domain. Levels with even (odd) parity are shown in blue (orange) and ordered by their total angular momentum J. The energy E with respect to the ground state is given as inverse length and corresponding wavelength λ. All data, conveniently accessible via [55], has been taken from [53, 54].

possible to Doppler-cool the atoms down to a few tens of nK. All three transitions mentioned are summarized in Tab. 2.3 for comparison.

2.2.2. Nearly Degenerate States of Opposite Parity

The complex level scheme emerging from the previously described submerged shell configuration also increases our chances to find groups of states with special properties. In particular, the discovery of two nearly degenerate states of opposite parity, termed opposite parity doublet (OPD), at 19 797.96 cm^{-1} [62, 63] has made Dy a major candidate for fundamental measurements of the variation of the fine-structure constant [64] and possible parity violating effects originating from the interaction of atoms with cosmic fields [65, 66]. The two states of the OPD have a difference in energy of less than 300 MHz. Such a pair of states could also serve as a potentially groundbreaking platform for the observation of phenomena regarding quantum magnetism and previously unexplored lattice models [67–69]. Unfortunately, the aforementioned OPD offers neither sufficient lifetime nor strong enough interactions to achieve these prospects. However, a more suitable OPD, separated by 35 GHz has been proposed

Table 2.3.: Overview of the most commonly used transitions for laser-cooling of dysprosium. The wavelength λ and the transition rate Γ have been taken from the respective references [59, 61]. All other quantities can be derived. This includes the lifetime $\tau = 1/\Gamma$, natural linewidth $\Delta\nu = \Gamma/(2\pi)$, saturation intensity $I_{\mathrm{sat}} = \pi hc\Gamma/(3\lambda^3)$, Doppler temperature $T_{\mathrm{D}} = \hbar\Gamma/(2k_{\mathrm{B}})$ and Doppler velocity $\sqrt{\hbar\Gamma/(2m)}$. Furthermore we calculate the recoil temperature $T_{\mathrm{recoil}} = h^2/(mk_{\mathrm{B}}\lambda^2)$, recoil velocity $v_{\mathrm{recoil}} = h/(\lambda m)$ and MOT capture velocity $v_{\mathrm{cap}} = \Gamma\lambda/(2\pi)$, where we have used the average mass of Dy $m = 162.5$, the Planck constant h, reduced Planck constant $\hbar$, Boltzmann constant k_{B} and the speed of light c.

		421 nm [59]	626 nm [61]	741 nm [59]
Measured values	λ	421.291 nm	626.082 nm	740.963 nm
	Γ	$2.02 \times 10^8\,\mathrm{s}^{-1}$	$8.5 \times 10^5\,\mathrm{s}^{-1}$	$1.12 \times 10^4\,\mathrm{s}^{-1}$
Derived values	τ	4.94 ns	1.17 µs	1.68 µs
	$\Delta\nu$	32.2 MHz	136 kHz	1.78 kHz
	I_{sat}	$562\,\mathrm{W\,m}^{-2}$	$0.72\,\mathrm{W\,m}^{-2}$	$0.57\,\mathrm{mW\,m}^{-2}$
	T_{D}	773 µK	3.3 µK	43 nK
	v_{D}	$198\,\mathrm{mm\,s}^{-1}$	$12.9\,\mathrm{mm\,s}^{-1}$	$1.5\,\mathrm{mm\,s}^{-1}$
	T_{recoil}	659 nK	298 nK	213 nK
	v_{recoil}	$5.8\,\mathrm{mm\,s}^{-1}$	$3.9\,\mathrm{mm\,s}^{-1}$	$3.3\,\mathrm{mm\,s}^{-1}$
	v_{cap}	$13.6\,\mathrm{m\,s}^{-1}$	$85\,\mathrm{mm\,s}^{-1}$	$1.3\,\mathrm{mm\,s}^{-1}$

for this purpose[7] recently [27]. It consists of an odd-parity $[\mathrm{Xe}]\,4\mathrm{f}^{10}\,6\mathrm{s}\,6\mathrm{p}$ state at $17\,513.33\,\mathrm{cm}^{-1}$ and an even-parity $[\mathrm{Xe}]\,4\mathrm{f}^{10}\,5\mathrm{d}\,6\mathrm{s}$ state at $17\,514.50\,\mathrm{cm}^{-1}$. Let the odd (even) state be labeled $|a\rangle$ ($|b\rangle$) in shorthand notation. They have angular momentum $J_a = 10$ and $J_b = 9$, individual lifetimes of $\tau_a = 28.1\,\mathrm{s}$ and $\tau_b = 33.6\,\mu\mathrm{s}$ respectively and a reduced transition dipole moment of $\langle a|\hat{d}|b\rangle = 8.16\,\mathrm{D}$, where $\hat{d}$ is the dipole operator. After polarizing and coupling these states with experimentally accessible static magnetic and electric fields (100 G and $5\,\mathrm{kV\,cm}^{-1}$) an effective induced electric dipole moment $d_{\mathrm{eff}} = 0.224\,\mathrm{a.u.}$ and permanent magnetic dipole moment $\mu^* = 13\,\mu_{\mathrm{B}}$ is predicted. The length scale where dipolar interactions dominate is termed dipolar length $a_{\mathrm{d}} = md_{\mathrm{eff}}/\hbar^2$ and can be used to compare the interaction strength across different platforms. For the Dy OPD we expect $a_{\mathrm{d}} = 2299\,a_0$, where a_0 is the Bohr radius. This is comparable to experimental results with $^{40}\mathrm{K}^{87}\mathrm{Rb}$ diatomic molecules or $^{168}\mathrm{Er}_2$ Feshbach molecules yielding $a_{\mathrm{d,KRb}} = 1834\,\mathrm{a.u.}$ and $a_{\mathrm{d,Er}} = 1143\,\mathrm{a.u.}$ respectively [71, 72]. The coupling of $|a\rangle$ and $|b\rangle$ is generally chosen such that the major portion of the mixed state is in $|a\rangle$ with only a small fraction of $|b\rangle$. This is due to the fact that

[7] For the purpose of high-precision measurements these states were known and considered already before, but precise theoretical estimates were missing at the time [70].

the even state $|b\rangle$ does decay much faster. Decreasing the portion of $|b\rangle$, however, also decreases the effective dipole moment. Given the previously discussed dipolar length, the lifetime is expected to be on the order of several ms.

As these calculations are promising, one may think of possibilities to realize such states experimentally. Given the metastable nature of both states, they are not accessible via a one-photon transition from the ground-state $|g\rangle$. The current approach followed by the NewLanD experiment is the use of a stimulated Raman adiabatic passage (STIRAP) scheme to adiabatically transfer the population from the ground-state into one of the OPD states with high efficiency [73]. A level diagram visualizing this method as well as the states and transitions involved is shown in Fig. 2.3 (a). STIRAP is a two photon process thus requiring two distinct lasers termed pump[8]- and Stokes-laser. In our case a pump-laser at a wavelength of 418.6 nm for coupling the ground-state with the intermediate $[\mathrm{Xe}]\,4\,\mathrm{f}^{10}\,6\,\mathrm{s}\,6\,\mathrm{p}(8;1)^\circ$ state, and a 1571 nm Stokes-laser to couple the intermediate state with the target state $|b\rangle$. In order to transfer population from the ground-state into the target state, the two light-fields are applied as overlapping pulses with the Stokes pulse acting before the pump pulse. This counterintuitive order fundamentally distinguishes the STIRAP scheme from diabatic methods of population transfer such as π-pulses. This alleged conundrum can be understood by the fact that the Hamiltonian of the system features special eigenstates named adiabatic or dressed states which can be used to adiabatically transfer the population from $|g\rangle$ to $|b\rangle$ without ever populating the intermediate state. The scheme is robust against minor details, such as pulse shape and exact timing, yet is limited by the large difference in linewidth of the two transitions involved. In our case, the pulses have to be on the order of a few µs. Finally, a π-pulse in the microwave domain or DC electric field is then applied to mix $|a\rangle$ and $|b\rangle$. The following section aims at giving a short introduction to the physics that can possibly be explored.

2.3. Prospects for Dipolar Physics in the NewLanD Experiment

As already briefly mentioned in Sec. 1.1 the NewLanD experiment has been set up to simulate spin models of quantum magnetism in optical lattices, including but not limited to the generalized XYZ Heisenberg model

$$\hat{H}_{\mathrm{XYZ}} = \sum_{\langle i,j\rangle} \frac{\alpha_{ij}}{r_{ij}^3} \left[(\beta - \gamma\cos 2\phi_{ij})\,\hat{S}_i^x \hat{S}_j^x + (\beta + \gamma\cos 2\phi_{ij})\,\hat{S}_i^y \hat{S}_j^y \right] + \Delta_{ij}\hat{S}_i^z \hat{S}_j^z + \sum_i H_i \hat{S}_i^z, \tag{2.7}$$

[8] In some literature also labeled anti-Stokes.

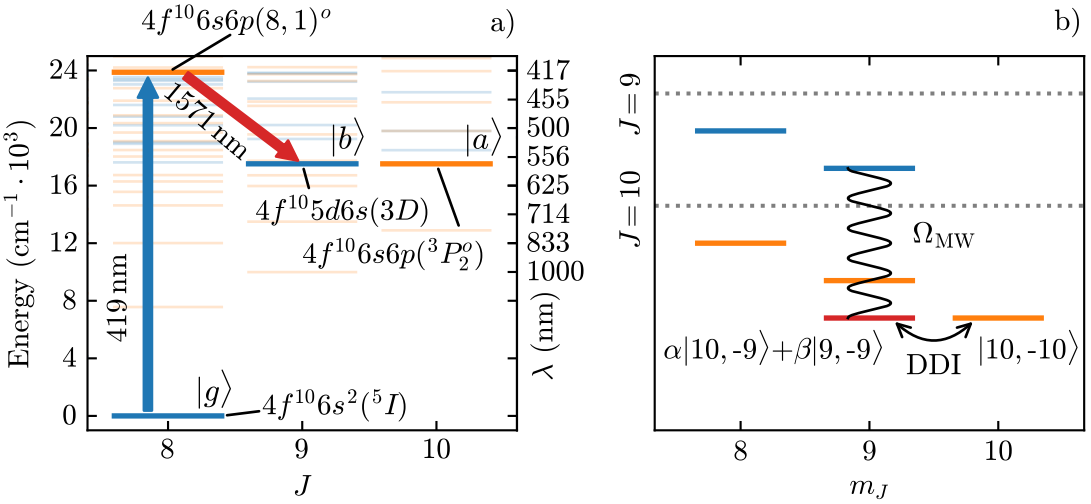

Figure 2.3.: Nearly degenerate states of opposite parity (OPD). The level diagram on the left (a) shows the two states of interest, termed $|a\rangle$ and $|b\rangle$, within the Dy level diagram. The ground state as well as the intermediate state we plan to perform STIRAP on is also highlighted with the respective wavelengths of the STIRAP transitions. On the right (b) we show the manifold of magnetic sublevels for the OPD states. The microwave transition used for mixing the states is indicated as Rabi frequency Ω_{MW}. A strong dipole-dipole interaction (DDI) is predicted between the mixed state $\alpha\,|10,-9\rangle+\beta\,|9,-1\rangle$ (red) and the maximally polarized $|10,-10\rangle$ state.

where $\hat{S}_i^x$ denotes the spin-operator of atom i for direction x and H_i is the local effective magnetic field. The realization of systems with strong dipolar interactions and tunable rates α_{ij} and Δ_{ij}, by means of mixing nearly degenerate opposite parity states has primarily been explored with diatomic molecules of the alkali family [74–79]. Usually, such species are brought to quantum degeneracy individually. The efficient preparation of ultracold molecules with dipole moments on the order of a few Debye has, however, posed challenging demands on experimental setups, leading to high complexity and low lattice filling fraction. Moreover, the inherent symmetry of the isospins chosen in the rotational manifold of the molecular ground state typically render a symmetric XXZ model, i.e., $\gamma = 0$ [20]. A widely studied alternative are atoms in highly excited Rydberg states [80–84] which, in turn, are short lived and sensitive to thermal radiation. For simple systems of single-species alkali atoms it has been proposed that magnetic interactions could be mediated by super-exchange [85]. This mechanism is also exploited in a proposal to load atoms in a p-band to realize even more exotic models [68]. As the super-exchange interaction strength is proportional to t^2/U, where t is the tunneling rate and U is the on-site interaction energy, these systems require temperatures on the order of pK. Together with the

difficulty of completely filling the p-band, this makes these systems not yet realizable experimentally.

Atoms with high magnetic moment in the ground state, such as dysprosium or erbium have dipolar interaction strengths on the order of 0.1 D, i.e., an order of magnitude less than typical diatomic molecules. They however benefit from the relative simplicity of experimental setups. Together with optical lattices in the UV domain and a proper magnification technique before imaging, such as the aforementioned matter optic magnifier, these species can be used to simulate models of quantum magnetism. This approach, yet, poses difficulties in changing the respective rates of the model and conceptual differences [18, 86].

While still benefiting from the simplicity of a single species experiments, the limitations of the just mentioned systems could be overcome by not using the ground state, but utilizing the aforementioned rich level scheme of Dy, namely the OPD presented in Sec. 2.2.2 in the following way. We consider a 2D system of Dy atoms in the $x-y$ plane that has been prepared in state $|b\rangle$ as described before. Let a magnetic field $\vec{B} = B\vec{e}_z$ point perpendicular to that plane and a oscillating electric field $\vec{E} = E\exp(i\omega t)\,\vec{e}_z$, i.e., a microwave, be polarized in the same direction. As shown in Fig. 2.3, the microwave dresses the states $|10,-9\rangle$ and $|10,-10\rangle$ within the manifold of magnetic sublevels of the OPD states $|a\rangle$ and $|b\rangle$ respectively [87, 88]. The $|10,-10\rangle$ state will be unaffected by this dressing as it lacks a counterpart in the $J=9$ manifold. The Landée g-factors of the OPD states are $g_\mathrm{a} = 1.3$ and $g_\mathrm{b} = 1.32$ respectively. We can therefore safely assume that the Zeeman shift will not change the detuning δ of the microwave. Now let $|1\rangle = |10,-10\rangle$ and $|2\rangle = \alpha\,|10,-9\rangle + \beta\,|9,-9\rangle$ with $\alpha = \sin\theta$ and $\beta = \exp(i\omega t)\cos\theta$ where we define the mixing angle $2\theta = \cos^{-1}\left(-\delta/\sqrt{\delta^2+\Omega^2}\right)$. Those two states can be brought to degeneracy by applying a magnetic field, i.e., a Zeeman shift of $g\mu_\mathrm{B}B = \hbar/2\cos(2\theta)$, where we use $g = 1.3$. We restrict ourselves to small mixing angles, as the lifetime of the dressed state is significantly shortened when rapidly decaying state $|b\rangle$ contributes more. At this point, it should be emphasized that the mixing angle θ and the energy of the mixed state can be tuned individually by varying the two free parameters δ and Ω.

The general Hamiltonian of the dipole-dipole interaction

$$\hat{H}_\mathrm{DDI} = \frac{\hat{\vec{d}}_i\hat{\vec{d}}_j - 3(\vec{e}_{ij}\cdot\hat{\vec{d}}_i)(\vec{e}_{ij}\cdot\hat{\vec{d}}_j)}{r_{ij}^3}, \tag{2.8}$$

where $\hat{\vec{d}}_i$ is the dipole operator acting on the i-th atom, $\vec{e}_{ij}$ is the unit vector connecting the two atoms and r_{ij} is their distance, can be rewritten to

$$\hat{H}_\mathrm{DDI} = \frac{\sqrt{6}}{r_{ij}^3}C^{(2)}(\vec{r_{ij}})\cdot\left(\hat{\vec{d}}_i\otimes\hat{\vec{d}}_j\right)^{(2)}, \tag{2.9}$$

with $C^{(2)}(\vec{r}_{ij}) = \sqrt{4\pi/5}\, Y_m^{(2)}(\vec{r}_{ij})$, where $Y_m^{(2)}(\vec{r}_{ij})$ is the second rank spherical harmonic of degree m. We can then write out the relevant components of this Hamiltonian

$$\hat{H}_0 = \frac{1}{r_{ij}} \frac{\hat{d}_1^i \hat{d}_{-1}^j + \hat{d}_{-1}^i \hat{d}_1^j}{2} + \hat{d}_0^i \hat{d}_0^j, \tag{2.10}$$

$$\hat{H}_{\pm 2} = -\frac{3}{2r_{ij}} \hat{d}_1^i \hat{d}_1^j e^{-2i\phi_{ij}} + h.c., \tag{2.11}$$

where the subscript of the dipole operators denotes the magnetic quantum number and ϕ_{ij} is the azimuthal angle of the vector $\vec{r}_{ij}$. The $\hat{H}_{\pm 1}$ component vanishes in the planar geometry. This can be projected in the $|1\rangle$, $|2\rangle$ basis such that we arrive at the XYZ Hamiltonian of Eq. 2.7 with an additional term of the form

$$\sum_{\langle i,j \rangle} \gamma \left(\hat{S}_i^x \hat{S}_j^y + \hat{S}_i^y \hat{S}_j^x \right) \sin 2\phi_{ij}. \tag{2.12}$$

In terms of the states $|1\rangle$ and $|2\rangle$ the spin operators have been defined in the usual way $\hat{S}_i^z = 1/2(|1\rangle_i \langle 1|_i - |2\rangle_i \langle 2|_i)$, $\hat{S}_i^x = 1/2(|1\rangle_i \langle 2|_i + |2\rangle_i \langle 1|_i)$ and $\hat{S}_i^y = 1/2i(|1\rangle_i \langle 2|_i - |2\rangle_i \langle 1|_i)$. The rate α_{ij} scales with d^2/ϵ_0 for electric DDI or $\mu_0 m^2$ for magnetic DDI, where d and m are the electric and magnetic dipole moments respectively. The spin-orbit part of the DDI yields $\gamma \neq 0$ and therefore a breaking of symmetry in x and y. The other rates depend on the exact configuration of the two states and the Clebsch-Gordan coefficients that connect them. Coming back to the statement that the degeneracy of states $|1\rangle$ and $|2\rangle$ can be maintained for different choices of the mixing angle θ, we see that these rates are tunable and dependent on the lattice geometry via ϕ_{ij}. The relative strength of electric and magnetic interactions can be chosen aswell.

3. Simulation and Realization of a Permanent Magnet Zeeman Slower for Dy

In the preceding chapter we introduced ultracold dysprosium as a prolific and versatile experimental platform featuring handles for cooling and trapping as well as unique possibilities for the exploration of quantum magnetism and exotic lattice models. We now bridge the gap between said concepts and the main tasks of this thesis, which include the design, simulation and realization of a permanent magnet Zeeman slower for dysprosium and the planning and building of a basic vacuum apparatus. The major challenge thereby was to find a way to reduce the experimental complexity of established setups. Despite the fact that much work has been done in the small field of permanent magnet Zeeman slowers, to our knowledge, these devices have never been utilized for heavy lanthanide atoms with broad transitions like Dy. The present chapter aims to address this deficiency by demonstrating a simple, yet effective setup.

3.1. Concept

A typical experiment in atomic physics relies on the preparation of a gaseous atomic sample in an ultra high vacuum (UHV) environment. One typically uses thermal atoms as a starting point, which are then decelerated by a Zeeman slower or 2D MOT and then captured and cooled in a 3D MOT, which then loads into an optical dipole trap (ODT), magnetic trap, optical lattice or a combination of these. Our work is confined to the first two parts, i.e., does not include the trapping of an atomic cloud. Without going into too much detail, we now want to give a rough overview of the experimental setup as depicted in Fig. 3.1. Following this overview, the subsequent sections are dedicated to the individual parts in more detail. We start with the oven section, where dendritic chunks of Dy are heated to generate a hot atomic vapor. The geometry of the oven cell already yields some initial collimation of the atomic beam. The following vacuum chamber (cube 1) is not strictly required[1] but can be used to

[1] For the measurements on the final setup shown in the subsequent chapter this component has been omitted. It has, however, been considered in the design process and is therefore presented here.

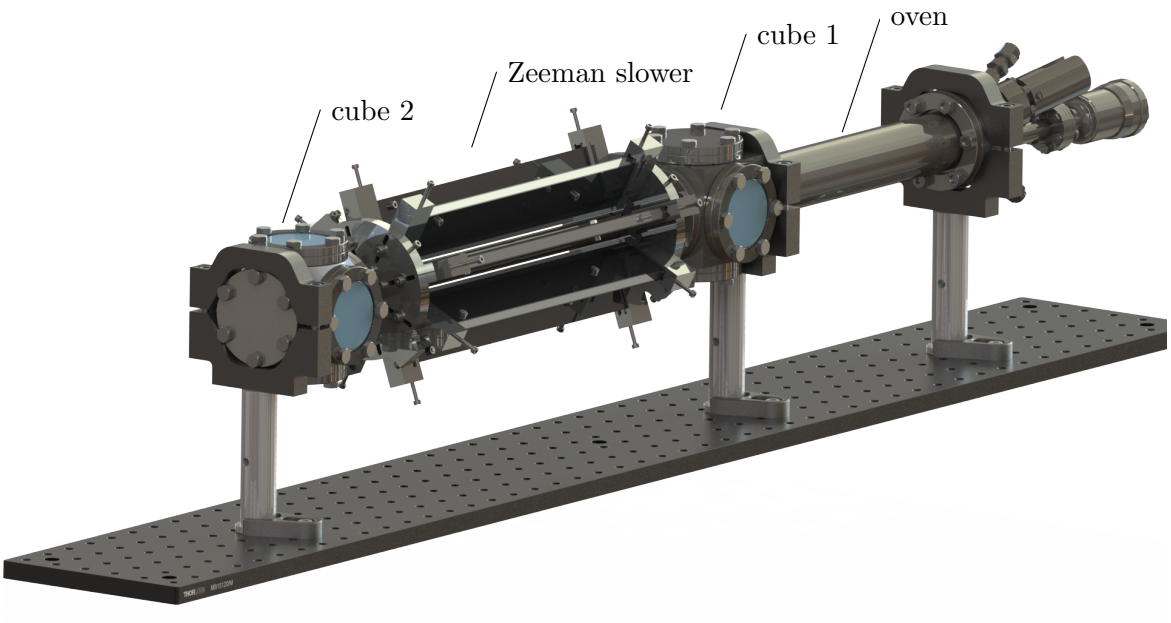

Figure 3.1.: Rendering of the vacuum apparatus. The oven (right) provides us with a beam of hot Dy vapor that can be characterized in the first small vacuum chamber (cube 1) before entering the Zeeman slower. The slow beam emerging from there is measured in the second chamber (cube 2) which also allows us the couple the Zeeman slower laser beam into the tube via an in-vacuum mirror.

characterize the spread and velocity distribution of the beam emerging from the oven. It could also be used for an additional transversal cooling stage. Proceeding along the setup we see the major part of the experiment that is, the permanent magnet Zeeman slower consisting of eight aluminum plates filled with permanent magnets. These plates are suspended on aluminum clamps that allow for slight adjustment of the plate position. Finally we use another small vacuum chamber (cube 2) to quantify the performance of the Zeeman slower. This chamber also features an in-vacuum mirror to deflect the slowing beam, coming from one of the viewports on the side, into the Zeeman slower tube. With this outline being given, we now focus on these parts individually, beginning in chronological order with the effusion oven.

3.2. Effusive Oven

Although various different kinds of sources for thermal atomic beams are known [89], the high melting point of dysprosium makes it challenging to construct an apparatus capable of producing a sufficient number of atoms. We thus operate a commercial high-temperature effusion cell [90] at 1100 °C to generate a thermal atomic beam. An

introduction to the physics of thermal beams, as well as simple ways to improve an oven setup, shall be given in the present section. A more detailed description of the construction of a custom oven, even for multiple species, is given in Ref. [91]. The objective of this section is to examine the process of generating a thermal atomic beam. Emphasis will be placed on the apparatus itself and the parameters affecting the beam quality.

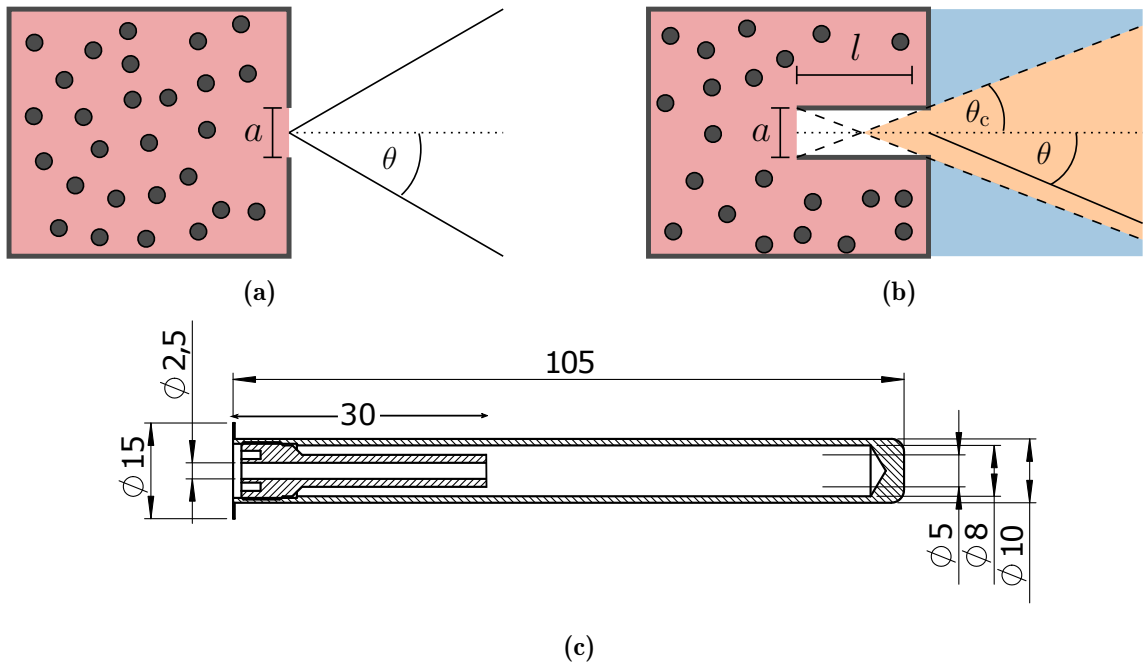

Figure 3.2.: Modeling an effusive source. **(a)** Schematic drawing of an effusion cell, modeled as a cosine emitter, with a thin-walled aperture a. **(b)** Schematic of a simple collimation setup where the aperture has been replaced by a tube of diameter a and length l. The small (large) angle regime is shown in orange (blue). **(c)** The crucible used in our setup, provided by the company MBE (see Ref. [90]). Dimensions are given in mm.

3.2.1. Cosine Emitter

An effusion cell in its most basic implementation is shown schematically in Fig. 3.2a. It can be thought of as an insulated box filled with chunks of source material and heated to a temperature T. An atomic or molecular vapor at pressure p, dependent on the vapor pressure of the material, forms inside the cell and can only escape through a small aperture of diameter a. We consider a gas of Dy atoms, modeled by an ideal gas inside of such a simplified effusion cell. Our starting point for estimating the atom flux emerging from the apparatus is the knowledge of the number density n of atoms inside the oven. At known oven temperature T, the number density can be calculated from the vapor pressure p_{vap} by means of the ideal gas equation $n = p_{\mathrm{vap}}/k_{\mathrm{B}}T$. Given

the Antoine coefficients, found in Sec. 2.1, p_{vap} can be estimated for any temperature T via Eq. (2.1). For a typical atomic beam experiment, the oven temperature, i.e., number density has to be chosen such that collisions between atoms are negligible. The low-pressure regime, in which said condition is fulfilled, is referred to as effusive or transparent regime, in contrast to the hydrodynamic or viscous regime at higher pressure. We can quantify the distinction between these regimes by considering the mean free path λ_{mf} of a single atom, given by

$$\lambda_{\mathrm{mf}}^{-1} = \sqrt{2}\pi\sigma_0^2 n, \tag{3.1}$$

with σ_0 being the diameter of the atom. An oven is operating in the effusive regime whenever λ_{mf} is larger than the oven aperture a, the relevant length scale of the apparatus. The atom speed, i.e., the velocity after integration over the full solid angle follows the Maxwell Boltzmann distribution

$$f(v) = 4\pi \left(\frac{m}{2\pi k_{\mathrm{B}} T}\right)^{\frac{3}{2}} v^2 \, \mathrm{e}^{-\frac{mv^2}{2k_{\mathrm{B}}T}}, \tag{3.2}$$

where the expectation value of the distribution is given by $\bar{v} = \sqrt{8k_{\mathrm{B}}T/\pi m}$ and the speed with maximum probability is $\hat{v} = \sqrt{2k_{\mathrm{B}}T/m}$. Following the formalism presented in Refs. [92, 93], one can then show with basic kinetic arguments that the flux emerging from a hole of area $A = \pi a^2/4$ as depicted in 3.2a is given by

$$\Theta = \frac{1}{4} n \bar{v} A. \tag{3.3}$$

In analogy to Lambert's law for a diffusely reflecting surface, we can determine the proportion of Θ that is emitted into the solid angle $\mathrm{d}\Omega = 2\pi \sin(\mathrm{d}\theta)$. One can assume that every point of the aperture emits atoms isotropically into all spatial directions. The angular distribution is thus given by

$$f(\theta) = \cos(\theta)/\pi, \tag{3.4}$$

such that the integral over the full half-space is 1. The flux ϑ into a cone with opening angle θ measured from the axis perpendicular to the hole is then given by

$$\vartheta(\theta) = 2\pi\Theta \int_0^{\theta} f\left(\tilde{\theta}\right) \sin\left(\tilde{\theta}\right) \mathrm{d}\tilde{\theta} = \Theta \sin^2(\theta). \tag{3.5}$$

A typical experiment can only capture atoms traveling within a small angle from the center axis. For the radius of our Zeeman slower tube $r = 7\,\mathrm{mm}$ and the approximate distance between oven and the main chamber (cube 2), we find an efficiency $\eta = \vartheta/\Theta \approx 0.05\,\%$. It is therefore beneficial to alter the angular distribution such that emission into larger angles is partially suppressed.

3.2.2. Collimation Setups

There are various different collimation setups available, some of which are presented in Ref. [93]. A simple yet fruitful approach is to replace the thin walled aperture with a tube of length l and inner diameter a. For the model depicted in Fig. 3.2b it can be shown that the total flux is reduced to $\Theta' = W \times \Theta$ with

$$W = \frac{8a/3l}{8a/3l + 1} \tag{3.6}$$

being the Clausing factor for a tube. As before, we have neglected atom-atom collisions[2]. Intuitively, we expect the angular distribution to change considerably. To quantify that, one has to consider two angular regimes, separated by the critical angle $\theta_c = \arctan(a/l)$. In the large angle regime $\theta > \theta_c$ the atomic beam only consists of particles that have undergone collisions with the walls of the tube, whereas for $\theta < \theta_c$ there are also atoms present that went straight through the tube. One can show that the angular distribution is given by

$$f'_{\theta>\theta_c}(\theta) = \frac{\cos(\theta)^2}{\pi^2 \sin(\theta)} \frac{8a}{3l} \frac{(1-W)}{W} + \frac{\cos(\theta)}{2\pi}, \tag{3.7a}$$

$$f'_{\theta<\theta_c}(\theta) = \frac{2\cos(\theta)}{\pi^2 W} \left[(1 - \frac{W}{2}) R(p) + \frac{2}{3}(1-W) \frac{1-(1-p^2)^{3/2}}{p} \right] + \frac{\cos(\theta)}{2\pi}, \tag{3.7b}$$

with $p = \tan(\theta) l/2a$ and $R(p) = \arccos(p) - p\sqrt{1-p^2}$ for the large (a) and small (b) angle regime respectively. A comparison with the angular distribution for the cosine emitter is shown in Fig. 3.3 for different l/a ratios. As for the cosine emitter, we can calculate the flux ϑ' emitted in a cone with opening angle θ by integration of Eq. (3.7b)

$$\vartheta'(\theta) = 2\pi\Theta' \int_0^\theta f'_{\theta<\theta_c}\left(\tilde{\theta}\right) \sin\left(\tilde{\theta}\right) \mathrm{d}\tilde{\theta}, \tag{3.8}$$

for $\theta < \theta_c$ in our case. Numerically we find an efficiency $\eta' = \vartheta'/\Theta' \approx 0.48\,\%$. As a result, by simply replacing the thin-holed aperture with a tube, we can reduce the total number of atoms that are depleted over time by a factor $W^{-1} = 5.5$. This is beneficial in terms of budget and maintenance, since the oven reservoir has to be replaced less often while the portion of atoms that can reach the following parts of an experiment is only diminished by by a factor $W\eta'/\eta = 0.82$. Moreover, when compared to other experiments in our group, one can recognize the advantage of our very compact design that allows larger angles of emission being captured. This simple geometric argument explains η' being larger by a factor of ~ 2 when compared to these setups [91].

[2] When introducing the length of the tube as second length-scale of the apparatus, there exists an intermediate regime between the two aforementioned regimes when $a < \lambda_{\mathrm{mf}} \leq L$. In this so called opaque regime, one has to partially consider atom-atom collisions also.

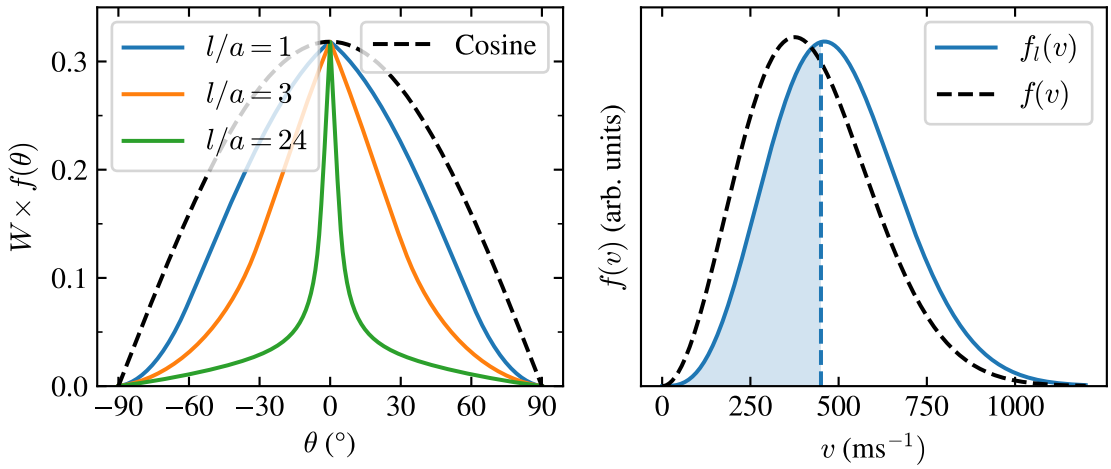

Figure 3.3.: Angular- and velocity distribution of an atomic beam emitted from an effusion cell. On the left, the angular distribution for different length-to-radius ratios is shown and compared to the cosine emitter (dashed line). On the right, the longitudinal velocity distribution $f_l(v)$ is shown in blue and compared with the Maxwell-Boltzmann distribution $f(v)$ inside the cell (dashed line). The blue shaded area represents the fraction of velocities that should be captured by our Zeeman slower for future reference.

3.2.3. Atom Velocity Distribution

The atoms that emerge from the effusion cell in such an angle that they can reach the trapping region of the experiment, exceed the trapping velocity of a typical 3D MOT by a large amount. We therefore slow the longitudinal motion down with a Zeeman slower. For determining the design and efficiency of that following stage, the longitudinal distribution of speed is of great interest. For the atomic beam leaving the effusion cell, it changes from Eq. (3.2) to

$$f_l(v) = 4\pi \left(\frac{m}{2\pi k_B T}\right)^{\frac{3}{2}} v^3 e^{-\frac{mv^2}{2k_B T}}, \tag{3.9}$$

which can be intuitively understood by the fact that atoms with higher velocity have more collisions with the walls of the effusion cell and, thus, a higher probability to hit the aperture [92]. Mathematically, one arrives at Eq. (3.9) when replacing $\bar{v}$ in Eq. (3.3) by its definition as the expectation value of the Maxwell-Boltzmann distribution. One can then directly derive the distribution after the oven from the definite integral. A comparison of the distribution of speeds inside and outside of the oven is shown in Fig. 3.3. The expectation value of Eq. (3.9) is greater than the one of the Maxwell Boltzmann distribution by a factor of $3\sqrt{\pi}/4$. Given the fact that only a small portion of atoms with velocities of a few m s^{-1} can be captured by the following trapping stages, our objective is to alter the distribution (3.9) such that more atoms have velocities in

the desired region. We achieve this by slowing down and compressing the distribution in a permanent magnet Zeeman slower. The details of how this is done are described in the following section.

3.3. Permanent Magnet Zeeman Slower

A Zeeman slower combines strong magnetic fields and an intense laser beam to continuously decelerate atoms by resonant scattering of photons. The magnetic field is necessary to maintain the resonance condition throughout the slowing process as the frequency of the atomic transition changes due to the velocity dependent Doppler shift. The magnetic field is therefore required to have a specific spatial profile, which we will discuss in Sec. 3.3.1. This is most commonly achieved by a tapered solenoid, i.e., different coils wound around the tube along which the atoms propagate. However, more recent work [31] has shown that it is not only possible, but often advantageous to use permanent magnets for this purpose as they offer several advantages. Firstly, permanent magnet setups operate without the need for power supplies and high currents. Also, they avoid water cooling which is mandatory for preventing electromagnets from overheating. Finally permanent magnets, if engineered carefully, produce a smoother field profile which allows for higher values of stable deceleration. These advantages are, however, accompanied by the shortage of possibilities to tune the magnetic field once the device is assembled. Our design includes measures to mitigate this problem to some extent.

3.3.1. Fundamental Concepts

Atomic transitions used for laser cooling are isolated and closed in good approximation. We therefore consider an atom that is modeled by a two level system. When we shine monochromatic light with frequency ω_L on this simplified system, it scatters photons at a rate

$$R_\mathrm{scatt} = \frac{\Gamma}{2}\frac{\Omega^2/2}{\delta^2 + \Omega^2/2 + \Gamma^2/4}, \tag{3.10}$$

where Ω is the Rabi frequency, Γ is the spontaneous decay rate rate and $\delta = \omega_\mathrm{L} - \omega_0$ is the detuning of the light's frequency from the atomic resonance frequency ω_0 which we require to satisfy the condition $\delta \leq \Gamma$. Let the light propagate along an axis $\vec{e}_z$. Every time a photon is absorbed, it transfers its momentum $\hbar\vec{k}$ to the atom, where $\vec{k} = 2\pi/\lambda \times \vec{e}_z$ is the wavevector and λ is the wavelength of the light. Naturally the same amount of momentum is transferred when the photon is re-emitted. However, the direction of spontaneously[3] emitted photons is uniformly distributed over the full

[3]Stimulated absorption and emission do not exert a net force on the atom and are therefore not considered.

solid angle such that their contributions to the longitudinal motion average to zero[4]. Therefore, there is a resulting net force

$$F_{\text{scatt}} = \frac{\hbar k \Gamma}{2} \frac{\Omega^2/2}{\delta^2 + \Omega^2/2 + \Gamma^2/4}, \tag{3.11}$$

in $\vec{e}_z$ direction. This is a dissipative force, i.e., a force that transfers energy from a system of interest to some other system or "bath". In our case, the scattering force transfers energy between the center of mass motion of the atom and the electromagnetic vacuum via the atom's internal degrees of freedom. Now let the atom move at some velocity $\vec{v} = -v \times \vec{e}_z$ opposite to the direction of the light. The resonance frequency of the atom is then Doppler shifted to $\omega_0' = \omega_0 + kv$. One can account for that by changing the laser frequency to again closely match the resonance frequency. Now as the scattering force acts and the atom is being decelerated, its velocity and thus the Doppler-shifted resonance frequency changes until the light is no longer resonant with the transition. To prevent the violation of the resonance condition, a spatially varying magnetic field $B(z)$ is applied that compensates the changing Doppler shift by a counteracting Zeeman shift $\omega_0' = \omega_0 \pm \mu' B(z) \hbar^{-1}$, with $\mu' = \mu_{\text{B}} h^{-1} \left(m_{\text{e}} g_{\text{e}} - m_{\text{g}} g_{\text{g}}\right)$ being the magnetic moment of the transition, where g_{e}, g_{b} and m_{e}, m_{g} are the Landeé g factors and magnetic quantum numbers of the excited and ground state respectively. As the transition can either be σ^+ or σ^- we use the $\pm$ sign. The detuning of the laser light with respect to the atomic transition can therefore be expressed as the sum of some initial detuning δ_0, the velocity dependent Doppler shift and Zeeman shift, such that

$$F_{\text{scatt}}\left(z, v\right) = \frac{\hbar k \Gamma}{2} \frac{s_0(z)}{1 + s_0(z) + 4\left(\delta_0 + kv \pm \mu' B(z)/\hbar\right)^2 / \Gamma^2}, \tag{3.12}$$

where we introduced the saturation parameter $s_0(z) = I(z)/I_{\text{sat}} = 2\Omega(z)^2/\Gamma^2$. This treatment considers a spatially varying light intensity $I(z)$ e.g. Gaussian laser beams [33]. When the total detuning is zero, the maximum deceleration imposed on the atoms is

$$a_{\max}\left(z\right) = \frac{\hbar k \Gamma}{2m} \frac{s_0\left(z\right)}{1 + s_0\left(z\right)}, \tag{3.13}$$

with m being the mass of an atom. However, in practical applications, this ideal scenario is not achievable. This is due to the presence of even small variations in the magnetic field or spontaneous heating processes, which can result in the atoms falling out of resonance. For stable deceleration, we limit ourselves to an effective deceleration $a(z) = \epsilon a_{\max}(z)$ with the safety parameter $0 < \epsilon < 1$. One can translate this condition

[4] In transversal direction the atoms are effectively heated due to the random walk originating from the many spontaneous emission processes. As this effect is smaller for heavy atoms like Dy and short Zeeman slowers we do not further investigate this mechanism in this work.

into an effective detuning

$$\delta_{\text{eff}}(z) = \frac{\Gamma/2}{\sqrt{(1+s_0(z))^{\frac{1-\epsilon}{\epsilon}}}}, \tag{3.14}$$

and then finds for the magnetic field as a function of the position

$$B(z) = \pm\frac{\hbar}{\mu'}\left(-\delta_0 - kv(z) + \delta_{\text{eff}}(z)\right). \tag{3.15}$$

The velocity of the atoms at every position, in this approach, can be found by numerically solving the differential equation

$$\frac{\partial v(z)}{\partial z} = \frac{\epsilon a_{\max}(z)}{v(z)} = \epsilon\frac{\hbar k\Gamma}{2m}\frac{s_0(z)}{1+s_0(z)}\frac{1}{v(z)}, \tag{3.16}$$

for some choice of $s_0(z)$, ϵ and capture velocity $v(0)$. To obtain an intuitive understanding of the resulting magnetic field we may assume a spatially invariant light intensity $s_0(z) = \tilde{s}_0$. Eq. (3.13) can then be solved analytically and results in a constant deceleration $a_{\max}(z) = \tilde{a}_{\max}$ such that we retrieve the general textbook solution [50]

$$B(z) = \pm\frac{hv_0}{\lambda\mu'}\sqrt{1-\frac{z}{l}} + B_{\text{offset}}, \tag{3.17}$$

where $v_0 = v(0)$ is the capture velocity, $l = v_0^2/2\eta\tilde{a}_{\max}$ the length of the Zeeman slower with $\eta = \epsilon(1+\tilde{s}_0)/\tilde{s}_0$ and B_{offset} an additional offset field. Given said quantities we can distinguish three kinds of Zeeman slower designs. The first, termed decreasing field Zeeman slower, is achieved by choosing a σ^- transition and $B_{\text{offset}} \approx 0$ such that the laser light is resonant at the very end of the Zeeman slower and the magnetic field decreases along the active region. This approach keeps the region of high magnetic field well separated from other parts of the experiment at the cost of nearly resonant light intersecting said following stages. Thus, one can, as an alternative, choose a σ^+ transition and let $B_{\text{offset}} \approx hv_0/\lambda\mu'$. The magnetic field is then rising from its minimal value at the entrance of the slower towards its maximum at the end. This increasing field Zeeman slower comes at the cost of higher magnetic fields near the subsequent experimental stages, yet with the benefit of the laser light being far detuned from resonance. An intermediate choice that allows for some detuning from the resonance frequency at zero magnetic field as well as moderate magnetic field strengths is characterized by $0 < B_{\text{offset}} < hv_0/\lambda\mu'$, i.e., a zero crossing of the magnetic field. For this kind of designs the terminology spin-flip Zeeman slower is commonly used. Strictly speaking it is a misleading term as there is no spin-flip happening but a flip of magnetic field.

In our discussion we have, so far, neglected that the magnetic field is a vectorial quantity. However, we have already distinguished between σ^+ and σ^- transitions

which need to be referred to some choice of quantization axis. It has proven feasible to use the direction of magnetic field for this purpose. In the case of the magnetic field being transversal to the direction of propagation of the atomic beam we speak of a transversal field Zeeman slower whereas for the magnetic field being parallel (antiparallel) to the atomic (laser) beam we speak of a longitudinal field Zeeman slower. The latter configuration has long been established as the only design option given that it naturally arises from a tapered solenoid wound around the vacuum tube.

Only when permanent magnets were used to realize the Zeeman slower field the transversal design was considered. The reason for this is the possibility to arrange the magnets as Halbach cylinder, providing a perfectly uniform field at the position of the atomic beam and highly suppressed stray fields at the outside of the apparatus. This facilitates engineering such devices with permanent magnets. However, the major drawback of such designs is the fact that only half of the incident laser power can be used to drive a chosen transition. This is due to the fact that quantization axis and light-propagation axis are perpendicular to each other and the polarization of light can not be engineered to be solely σ^+ or σ^- in the reference frame of the atoms such that, in general, only half of the incident light contributes to the deceleration process. Furthermore a transversal configuration only works for species with negligible Zeeman splitting of the ground-state such as Sr or Yb. It is therefore in general more favourable to work with longitudinal fields [33].

Now that we have set up the basic equations that set the framework for the design of our apparatus we first take a detour into the characteristics and peculiarities of permanent magnets as opposed to tapered solenoids before we discuss our approach in more detail.

3.3.2. Working with Permanent Magnets

At the microscopic level there exist two individual characteristics of matter that are linked to magnetism, namely charge and spin. This distinction manifests itself macroscopically in the existence of two separate kinds of magnets, electric and permanent. In physics laboratories we usually prefer the former sort to generate magnetic fields for several reasons. Firstly, the magnetic field $\vec{B}(\vec{r})$ at any position $\vec{r}$, can easily be calculated for some distribution of electric current using the Biot-Savart law. Secondly, as the field strength scales linearly with the current density, electromagnets offer tunability as it can be switched or swept. Although electromagnets are very capable in producing large magnetic fields up to several T, they are limited by resistive heating which scales quadratically with the current density and hence the magnetic field.

Permanent magnets can thus be an advantageous alternative when static fields have to be maintained without the requiring electric power or active control or when the application imposes constrains on size, weight, portability and simplicity. Nevertheless,

there are certain challenges involved in the design of magnetic assemblies comprising permanent magnets, which pose possible difficulties in engineering and require careful consideration. This section presents the key aspects of magnetic materials and magnetic fields resulting from permanent magnet assemblies. A thorough understanding of these properties is essential for optimizing the design and performance of permanent magnet-based systems. For more insight on the derivation of said properties from basic principles and the microscopic nature of magnetism we refer to Ref. [94].

Permanent Magnet Materials A permanent magnet is characterized by the kind, shape and amount of ferromagnetic material it is composed of. In the framework of classical electromagnetism, the characterization of a material exhibiting ferromagnetic behavior is primarily based on the concept of magnetization, denoted as $\vec{M}(\vec{r})$, which is defined as the local density of magnetic dipole moments at position $\vec{r}$. The response of $\vec{M}(\vec{r})$ to an external magnetic field is characterized by two material-specific parameters, namely coercivity and remanence, which we will briefly introduce in the following. In general, the magnetization in a ferromagnetic material is induced by an external magnetic field. However, many ferromagnetic materials, contingent upon exhibiting a non-zero magnetic coercivity H_C, can also retain a certain amount of magnetization M_r in the absence of an external field. The amount of this remanent magnetization is what one intuitively calls the *strength* of the magnet. One usually expresses the remanent magnetic field or remanence $B_\mathrm{r} = M_\mathrm{r}\mu_0$ in terms of M_r. The coercivity is defined as the measure of a material's resistance to changes in its magnetization. The specific definition of H_C, however, can be ambiguous as in some literature there exist three kinds of coercivity depending on the quantity that is used to describe the term *demagnetized*. There, the normal coercivity H_Cn is given by the magnetic field $\vec{H}$ at which the magnetic flux $\vec{B}$ inside the magnet vanishes. The remanence coercivity H_Cr and intrinsic H_Ci (also H_Cj) coercivity relate to the vanishing of remanence B_r and the magnetization $\vec{M}$ respectively. We exclusively use the latter, intrinsic coercivity, within the scope of this section. Materials with high coercivity are termed magnetically hard, i.e., they show little to no disturbance when exposed to moderate external fields whereas soft magnets change their magnetization easily.

In addition to the aforementioned properties that characterize a permanent magnet in the framework of classical electrodynamics, for practical applications, we also have to consider the material's resistance to high temperature and mechanical stress, both of which tend to deteriorate the magnetization over time. In the most extreme case, a permanent magnet loses its ferromagnetic properties entirely at a fixed temperature T_C, the Curie temperature. However, even at much lower temperatures, there is such a large reduction in magnetization that the magnet is no longer of any use in practical applications. Mechanical stiffness and brittleness also differ significantly between different materials. This becomes particularly important when magnetic parts have to

Table 3.1.: Comparative listing of the relevant parameters for the selection of the right permanent magnet material as described in the main text. These serve as rough reference as specifications usually vary between manufacturers and resellers. The alloy used in our work is Sm2Co17 YXG32 provided by [95].

Material	B_r (mT)	H_C (kOe)	T_max (°C)	T_C (°C)	Ref.
Ferrite HF32/25	420	3.27	300	450	[96]
NdFeB 30UH	1120	25.33	180	310	[95, 96]
NdFeB N52	1434	13.07	60	310	[95, 96]
Sm2Co5 YX22	933	25.73	250	756	[95, 97]
Sm2Co17 YXG32	1111	21.35	350	800	[95, 98]

be machined after being magnetized.

In summary, to produce large magnetic fields as one needs in a Zeeman slower, we have to choose a material with both high coercivity and remanence that is capable of withstanding typical temperatures of a vacuum apparatus close to the effusive oven. Additionally, the material should allow machining without demagnetizing significantly. Given these specifications we opted for the SM2Co17 alloy, provided by HKCM [95] in various shapes and sizes. The aforementioned characteristics for said material, along with other common alloys for comparison, are given in Tab. 3.1.

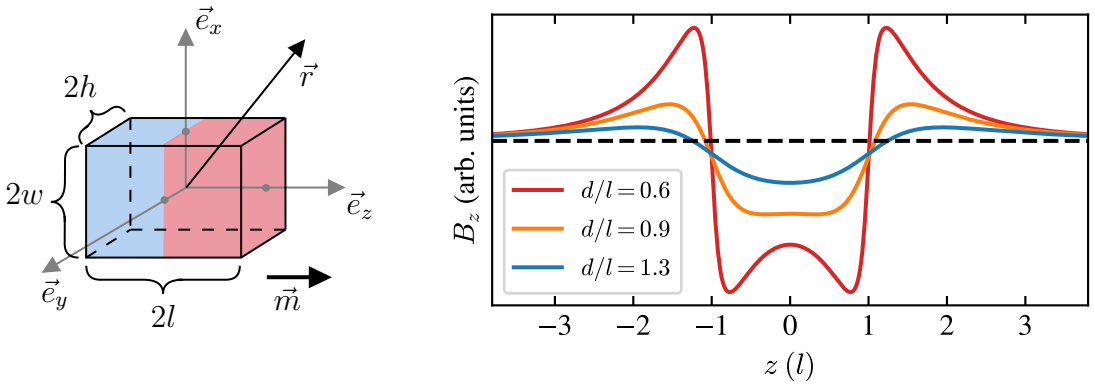

Figure 3.4.: Characteristic of cuboid magnets. The drawing on the left illustrates the dimensions used in the main text. On the right, we show a plot of the $\vec{e}_z$ component of the magnetic field of a cuboid permanent magnet measured along an axis parallel to the $\vec{e}_z$ axis at a radial distance d from the magnet center. The dimensions $h = 0.5$ and $w = 0.5$ as well as d and z are given in units of l. The red (blue) line shows the near-field (far-field) case whereas the orange line represents the intermediate case with flat top.

Fundamental Equations Now that we have introduced the basic quantities that govern the behaviour of permanent magnets we want to take a closer look on how to derive the magnetic fields they generate. For this purpose, motivated by our discussion on the choice of magnetic material, we make further assumptions on the magnetization for the case of hard rare-earth magnets. Let $\vec{M}(\vec{r})$ be uniform across the volume of the permanent magnet, i.e., at a constant value $\vec{M} = B_\mathrm{r}/\mu_0$ inside and zero otherwise. We furthermore assume that $\vec{M}$ is not influenced by external fields hence constant in direction and magnitude at any time. In the absence of charges, the macroscopic formulation of Maxwell's equations yields for the magnetic $\vec{H}$ field

$$\nabla \cdot \vec{H}(\vec{r}) = 0, \tag{3.18}$$

$$\nabla \cdot \left[\vec{M}(\vec{r}) + \vec{H}(\vec{r})\right] = 0. \tag{3.19}$$

We then obtain the magnetic $\vec{B}$-field from the well known relation

$$\vec{B}(\vec{r}) = \mu_0 \left[\vec{M}\left(\vec{r}\right) + \vec{H}\left(\vec{r}\right)\right]. \tag{3.20}$$

Solving the pair of differential equations (3.18, 3.19) for a given geometry may not be inherently difficult but burdensome for shapes that lack significant symmetries. It is therefore common to compose more complex shapes of smaller pieces with simpler geometry. In the case of permanent magnet Zeeman slowers this has been proposed by Ref. [33] for cylindrical pieces. Other approaches have been done with toroidal magnets [99]. In our design, however, we opted for cuboids due to their ease of handling, machining and mounting. Following Ref. [100], the magnetic field generated by a cuboid with dimensions and coordinates defined in Fig. 3.4 (left) is component-wise given by

$$B_x(x,y,z) = \frac{B_\mathrm{r}}{4\pi} \log\left[\frac{f_2(-x,y,-z)f_2(x,y,z)}{f_2(x,y,-z)f_2(-x,y,z)}\right], \tag{3.21}$$

$$B_y(x,y,z) = B_x(y,x,z), \tag{3.22}$$

$$\begin{aligned} B_z(x,y,z) = -\frac{B_\mathrm{r}}{4\pi} \big[&f_1(-x,y,z) + f_1(-x,y,-z) + f_1(-x,-y,z) \\ &+ f_1(-x,-y,z) + f_1(x,y,z) + f_1(x,y,-z) \\ &+ f_1(x,-y,z) + f_1(x,-y,-z)\big], \end{aligned} \tag{3.23}$$

with the auxiliary functions $f_1(x,y,z)$ and $f_2(x,y,z)$ defined as

$$f_1(x,y,z) = \arctan\left[\frac{(x+w)(y+h)}{(z+l)\sqrt{(x+w)^2+(y+h)^2+(z+l)^2}}\right], \tag{3.24}$$

$$f_2(x,y,z) = \frac{\sqrt{(x+w)^2+(h-y)^2+(z+l)^2}+h-y}{\sqrt{(x+w)^2+(y+h)^2+(z+l)^2}-h-y}. \tag{3.25}$$

In the far-field, i.e., for distances that are much larger than the dimensions of the magnet, the solution of Equations (3.21, 3.22, 3.23) simplifies to the solution of a magnetic dipole

$$B_x^{\mathrm{dip}}(x,y,z) = \frac{B_\mathrm{r}}{4\pi}\left[\frac{3xz}{r^5}\right],\ B_y^{\mathrm{dip}} = \frac{B_\mathrm{r}}{4\pi}\left[\frac{3yz}{r^5}\right],\ B_z^{\mathrm{dip}} = \frac{B_\mathrm{r}}{4\pi}\left[\frac{2z^2-x^2-y^2}{r^5}\right], \quad (3.26)$$

with $r = \sqrt{x^2+y^2+z^2}$. The simplified dipole solution, as in Eq. (3.26), represents the magnetic field generated by a magnetic moment $\vec{m} = B_\mathrm{r}V/\mu_0$ where V is the volume of the permanent magnet. This represents the solution in the far field as shown in Fig. 3.4 (right).

In the following section we present the design of an assembly of cuboid magnets to engineer the magnetic field for our Zeeman slower. There we will see that although the latter simplification is convenient to work with, it turns out that, to obtain large enough fields, one has to place the magnets closer to the specific region than the assumptions of the dipole approximation would allow. We thus perform all further calculations with the use of the exact analytic solution for a cuboid in the near field.

3.3.3. Design and Optimization

Several incremental steps of design have been made under consideration of four key requirements. Firstly, the overall device must be as compact as possible. As a figure of merit, we aimed for less than 30 cm of total length. Secondly, a student should be able to assemble the device within less than a day and without having to break the vacuum. Additionally, we require standalone operation over the timescale of an experimental setup, i.e., several years without having to maintain the setup in any way. Lastly the design should also allow for minor corrections of the magnetic field profile to compensate for the possibility of unknown external sources of magnetic field, the magnetization of other parts of the setup or demagnetization effects due to high temperatures or the machining of magnets. In this regard, the intensity and detuning of the laser light provides an additional handle. The very broad 421 nm transition offers the great benefit of being insensitive to small changes in the magnetic field as the natural linewidth of 32.2 MHz equals 22 G of magnetic field[5] However it is also prone to an effect we call overslowing which means that after the active region of the Zeeman slower the atoms get decelerated further and eventually stopped or pushed back into the source. This happens when the detuning of the light with respect to the transition in the region after the actual Zeeman slower is to small.

[5]We convert the linewidth in the frequency domain Δf to magnetic field ΔB by applying the known relation for the Zeeman shift $\Delta B = hf/\mu_\mathrm{B}\,(m_\mathrm{g}g_\mathrm{g} - m_\mathrm{e}g_\mathrm{e})$, where m_g, m_e and g_g, g_e are the magnetic quantum numbers and Landée g-factors of the ground and excited state respectively.

Given this perquisite and motivated by the simulations we will cover shortly, we opted for a mixture between rising field and "spin-flip" Zeeman slower design. Regarding the safety parameter, a rather ambitious $\epsilon = 0.8$ has been chosen to decrease the size of the device while maintaining a capture velocity of $450\,\mathrm{m\,s^{-1}}$. Given the exceptionally high saturation intensity of the slowing transition, we consider 500 mW of laser power and a longitudinal field design. The beam geometry is chosen such that the waist of the Gaussian beam is positioned near the aperture of the effusive oven. The waist is chosen such that the beam diameter at the end of the Zeeman slower tube is as large as the geometry allows. This results in a non-uniform saturation parameter $s_0(z)$ that further antagonizes overslowing.

The magnetic field distribution has been calculated with the use of equations (3.15, 3.16). Let z be the longitudinal axis along which the atoms propagate. At the entrance of the active region $z = 0$ we obtain a minimum value of $-195\,\mathrm{G}$. The magnetic field then reaches its zero-crossing at $z = 7.21\,\mathrm{cm}$ and rises to a maximum value of 530 G at $z = 21.5\,\mathrm{cm}$.

After having agreed on the aforementioned specifications it has been the major part of this master project to design, simulate and built a setup to realize the calculated magnetic field distribution with arrays of permanent magnets. It is an obvious choice to take advantage of the cylindrical symmetry of the apparatus by placing the magnets in a circular pattern around the vacuum tube. Instead of ring-shaped magnets, however, we aimed at optimizing the size and positions of rectangular magnets. This facilitates manufacturing and assembling and is in general the less expensive option. We consider eight similar sets of magnets placed in a circular pattern with an angular spacing of $2\pi/8$. The procedure of determining the free parameters of this setup is described in the following.

Optimization of Magnet Positions The code for the optimization is written in Python and takes a set of $n \times m$ parameters with bounds from a configuration file, where n is the number of magnets and m is the number of variable parameters per magnet. In general $m = 8$, with three parameters for the position and dimension each, the direction of magnetization ± 1 and the angle α, both with respect to the $\vec{e}_z$ axis. We can reduce the complexity by enforcing the rotational symmetry by fixing the y position to 0 and the y dimension to match the dimensions of the magnets we plan to purchase. The set of parameters is then adapted step-wise by a minimization algorithm [101, 102] to minimize the squared deviations of the field calculated from the assembly of magnets and the target field. Any constraints given by the apparatus itself, for example the minimum distance between the magnet and the atomic beam limited by the diameter of the used vacuum tube, must be taken into consideration by choosing appropriate bounds for each parameter.

The final set of parameters that represents our best trade-off between simplicity,

Table 3.2.: Positions and dimensions of the i-th magnet in the setup depicted in Fig. 3.6. The coordinate x_i denotes the radial distance of the magnets center of mass from the longitudinal axis, i.e., the z axis. We give two such values because the values between simulation and experiment differ by a global offset of 2.4 mm. The coordinate z_i denotes the distance of the magnets center of mass along said axis with respect to the first magnet that is placed at $z = 0$. Two magnets are tilted by the angle α_i where negative values indicate a tilt in clockwise direction. The length l_i and the height h_i differ between the magnets, while the width $w = 7$ mm is the same for all of them. The direction of magnetization is given with respect to the z axis. Coordinates are also depicted in Fig. 3.6.

	x_i^{sim} (mm)	x_i^{exp} (mm)	z_i (mm)	α_i (°)	l_i (mm)	h_i (mm)	Magnetization
i=1	47.9	45.5	0	0	36	10	+1
i=2	43.4	41.0	108	−8.6	56	10	−1
i=3	39.0	36.6	186	−8.6	96	20	−1

ease of manufacturing and match with theory is given in Tab. 3.2. The magnetic field calculated from that assembly is shown in Fig. 3.5 and compared to the target field. Additionally, we modeled the system in the commercial finite-element analysis software CST Studio. The results agree with our calculations within the uncertainty specified by the software. We then performed extensive numerical simulations for the propagation of atoms through the calculated magnetic field. These are presented in Sec. 3.4. Before that, however, we will have a closer look at how the magnet assembly is realized experimentally in the following.

3.3.4. Construction of a Tunable Setup

The setup consists of eight rectangular aluminum bars with dimensions 27.1 cm×4 cm× 0.7 cm that have three cutouts each, where the permanent magnets are positioned. These are held in place by two thin sheets of aluminum that are fixed to the side of the bar. At both ends of that, are custom clamps that allow for an adjustment of the distance between the bar and the atomic beam with screws located at the top. Another screw located at the back of the clamp is used to fix the bar in place once the distance has been optimized. In this way we allow for small corrections of the magnetic field to compensate for magnetization of any parts involved or the demagnetization of the magnets themselves due to the manufacturing or aging of the material. The clamps are in turn attached to a half-ring segment on each side that fits the vacuum tube around which the ZS is assembled. Consequently, we have two similar halves with four bars each that are screwed together. This allows for the construction of the ZS around a vacuum tube without the need to disrupt the vacuum. In our case, we use a custom stainless steel (316LN) tube with an inner diameter of 14 mm and an

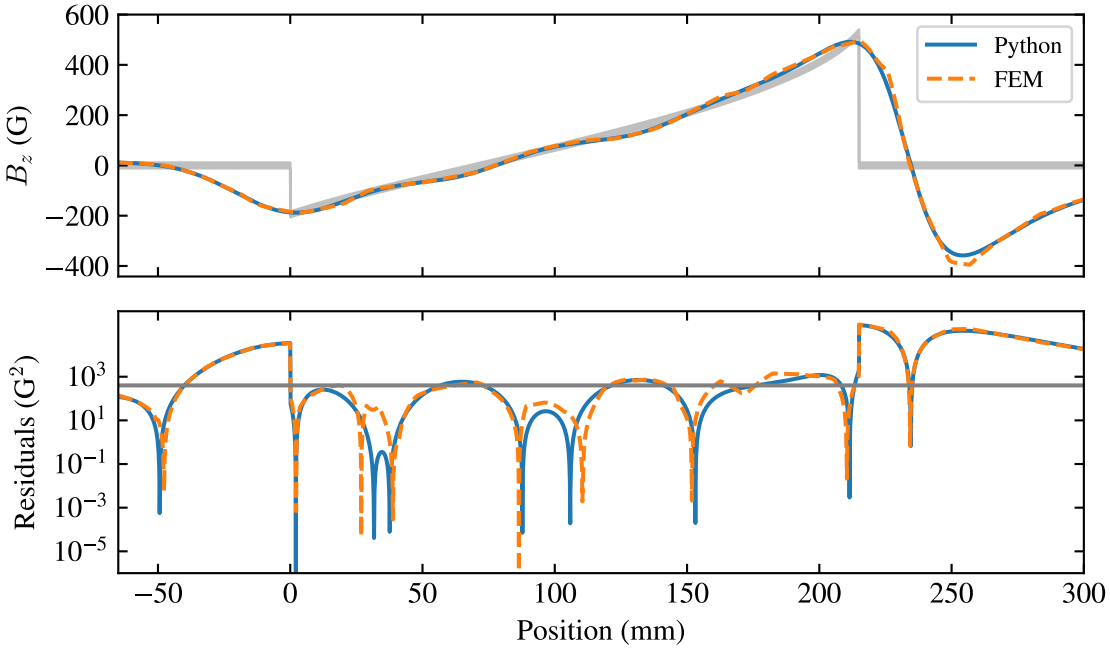

Figure 3.5.: Results of the numeric optimization. Magnetic field (blue) optimized to closely match the target field suggested by theory (gray) using Python and magnetic field obtained by analyzing the magnet configuration for the optimized field with a finite-element method (FEM) using the CST-Studio software. The lower plot shows the respective residuals defined as the squared deviations of the Python and FEM result from theory. The dips are a numeric artefact as they correspond to the data points where the calculated curves intersect with the theory curve. The straight gray line represents the magnetic field deviation that corresponds to the natural linewidth of the slowing transition.

outer diameter of 18 mm. Two CF16 flanges are welded to the tube with one of them being rotatable. The total length of the piece is 396 mm. This provides ample space for tightening the bolts of the vacuum components and the ZS itself.

As already mentioned, the magnets themselves are made from a Samarium Cobalt (SmCo) alloy with a distinctively high Curie temperature which makes them resistant against temperatures up to 350 °C. They are bought in rectangular pieces of 4 mm × 7 mm × 30 mm with the magnetization along the smallest dimension. Those pieces are stacked up to the length and cut to the height specified in Tab. 3.2 by wire electrical discharge machining (WEDM). There, it has been taken care to fix the length of each magnet to an integer multiple of the length of a single magnet piece and the kept the width at 7 mm. This allows us to obtain the desired dimensions with only one cut being made. The approach of stacking multiple small magnets to form bigger pieces has been chosen for maximum flexibility during the design phase. For similar projects in the future one could buy the magnets in custom sizes and thus eliminate the cutting entirely. We then prepare each rod as depicted in Fig. 3.6.

After assembling all the pieces we measured the longitudinal magnetic field B_z with a self-made Zeeman slower scanning device. It consists of a Honeywell SS495A1 Hall probe capable of measuring magnetic fields along a specified direction up to ±600 G with a conversion factor of 3.125(94) mV G^{-1} and a stepper motor that is used to pull the probe through the tube at the center of the assembly at a steady speed of 35.6 mm s^{-1}. After converting time to distance and voltage to magnetic field, we obtain the curves shown in Fig. 3.7 for different positions of the Zeeman slower rods. After optimizing the position of the aluminum bars experimentally, we can reprodue the calculated magnetic field profile within the uncertainty of the Hall sensor and the natural linewidth of the slowing transition. The distance of the magnet assembly from the symmetry axis deviates from our calculation by an offset of 2.4 mm.

3.4. Monte Carlo Simulation

To quantify any magnetic field that has been calculated by our optimization algorithm during the design process, we developed a numeric simulation for the propagation of atoms through the active region of the Zeeman slower. In the simple one-dimensional case, an atom is represented by a two-component state vector $s = (z, v)^{\mathrm{T}}$ with the first component being the position along the trajectory of the atomic beam and the second component being the velocity at a discretized instance of time. Starting at time $t = 0$ and position $z = 0$ the atoms enter the device with some initial velocity $v = v_0$. Now, in timesteps of $\Delta t = 50$ ns, the light-pressure force is calculated from the magnetic field and light intensity at the position of the atom and its velocity via

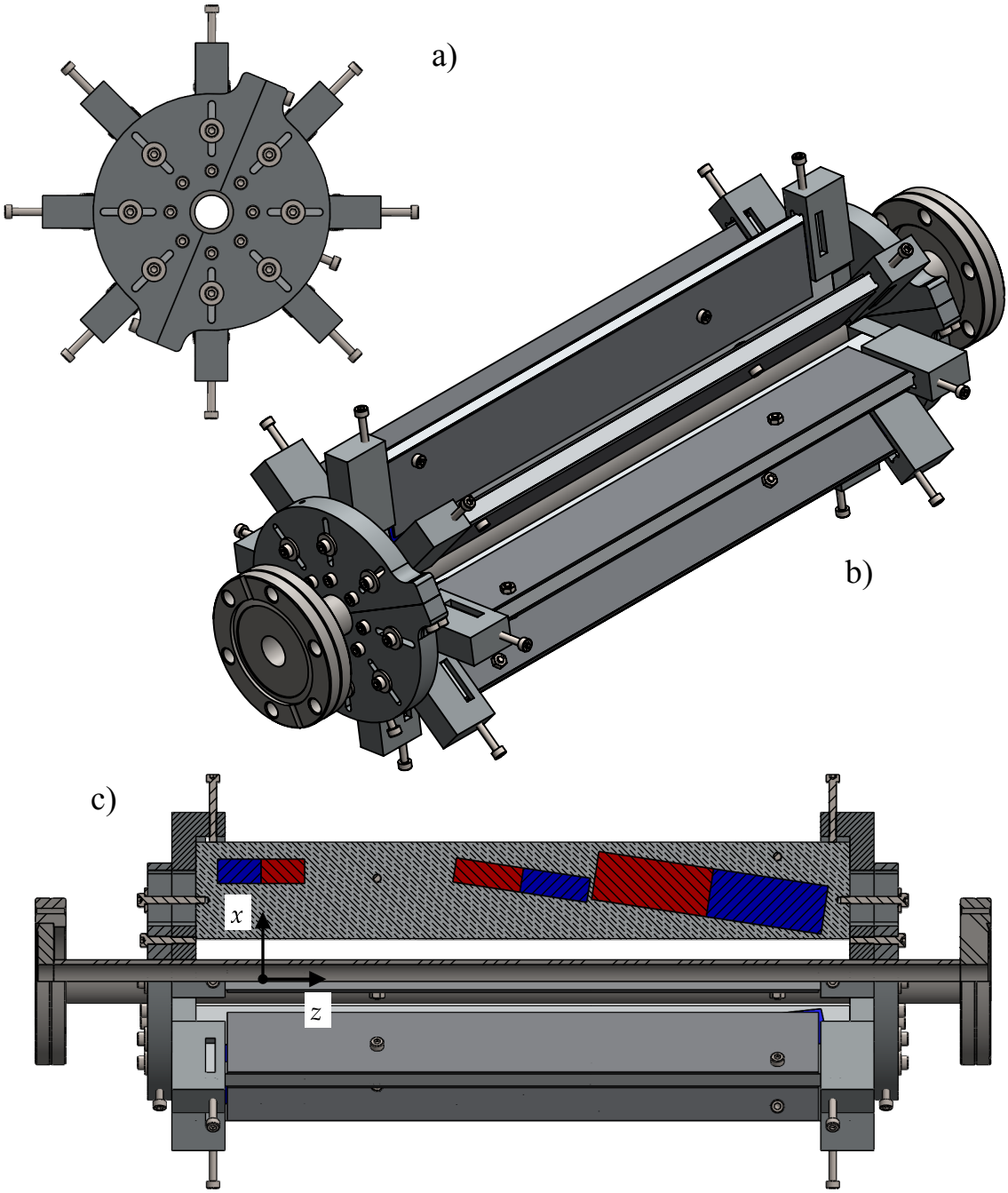

Figure 3.6.: Technical drawings of the Zeeman slower. In (a) we show a frontal view of the device, illustrating the two half-ring segments that are assembled around the vacuum tube. Slotted holes allow continuous adjustment of the assembly. Subfigure (b) shows a perspective view of the structure being mounted onto a vacuum tube with two flanges. The atomic beam is entering via the left flange (rotatable) and leaving the setup via the right flange (fixed). One can nicely see the thin aluminum sheets that are wrapped around the aluminum bars which hold the concealed magnets. Subfigure (c) depicts a side view and a half-cut through the assembly, revealing the clamping mechanism featuring adjustment screws at the top, fixation screws on the side and the magnets with the red (blue) side marking the direction of the north (south) pole. Coordinates are added as a reference.

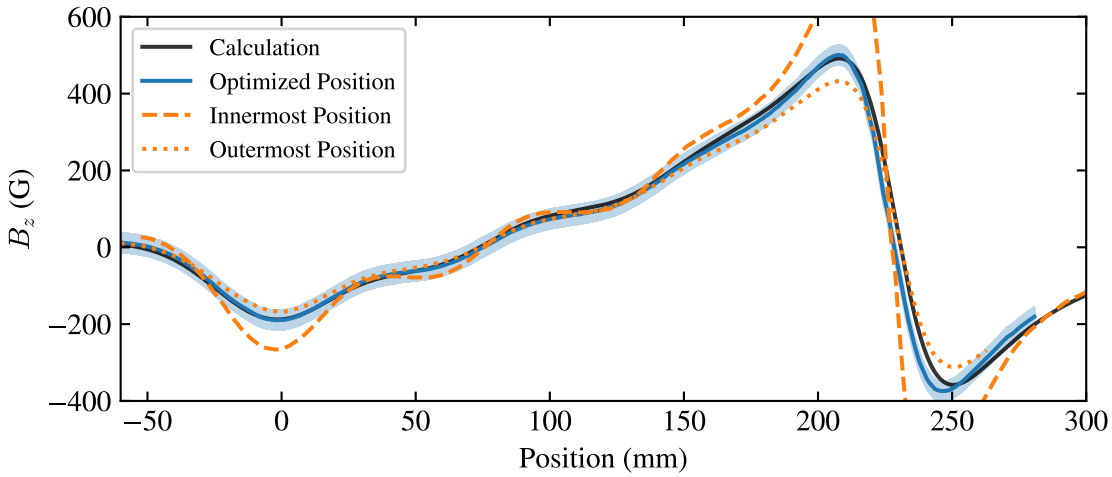

Figure 3.7.: Measured magnetic field as a function of the position along the Zeeman slower. The black line denotes the optimization result presented in Fig. 3.5. In blue, we show the magnetic field for the rods being positioned at a distance of 20.7 mm from the symmetry axis. The shaded area represents the 1σ interval that is dominated by the uncertainty of the Hall probe used. The dashed (dotted) orange line illustrates the magnetic field for the innermost (outermost) position of the rods, again with respect to the symmetry axis. These lines, corresponding to distances of 18.2 mm and 11.7 mm respectively, define the range across which we can tune the magnetic field.

Eq. (3.12). The velocity component of s is changed to

$$v' = v - \frac{F_{\text{scatt}}}{m}\Delta t, \tag{3.27}$$

where m is the mass of the atom. The position of the atom changes according to

$$z' = z + \frac{v + v'}{2}\Delta t. \tag{3.28}$$

This procedure is continued until the atom either reaches a defined position $z = z_{\text{stop}}$ or is completely stopped, i.e., $v < 0$. Firstly, to gain a qualitative understanding of how atoms with different starting velocities are decelerated, we recorded each step of the simulation for a range of evenly spaced velocities up to $500\,\mathrm{m\,s^{-1}}$. The results, separately taking into account the calculated magnetic field and the measured magnetic field with optimized magnet positions (see Fig. 3.7) are shown in Fig. 3.8. For the calculated magnetic field we expect atoms with velocities below $200\,\mathrm{m\,s^{-1}}$ to be overslowed, i.e., stopped before exiting the Zeeman slower. For the measured magnetic field this loss mechanism is calculated to affect velocities up to $250\,\mathrm{m\,s^{-1}}$. The maximum capture velocity is $480\,\mathrm{m\,s^{-1}}$ in both cases. These computations show in particular that small changes in the magnetic field at the end of the Zeeman slower have the greatest impact on the range of usable velocities, final velocities and thus losses due to overslowing.

As the performance of the Zeeman slower is directly linked to the flux of cold atoms available at the following experimental stages, we move on to the quantitative picture. To see how the typical longitudinal velocity distribution, introduced in Sec. 3.2.3, is altered after passing the Zeeman slower we performed a quantitative Monte Carlo simulation. Hereby, we follow the aforementioned approach, yet without tracking individual steps, but instead sampling a large number of initial velocities from the probability density function in Eq. (3.9). A histogram of the longitudinal velocity distribution before and after passing the Zeeman slower is shown in Fig. 3.9. For the measured magnetic field, we see a total reduction in the number of atoms by a factor 46.4 % and a clear signature of slowed atoms centered around $11.04(9)\,\mathrm{m\,s^{-1}}$ and with a FWHM of $22.0(3)\,\mathrm{m\,s^{-1}}$. It has to be pointed out, however, that the presented simulation does not include transversal motion and we can thus not claim to give a complete prediction of the final velocity distribution.

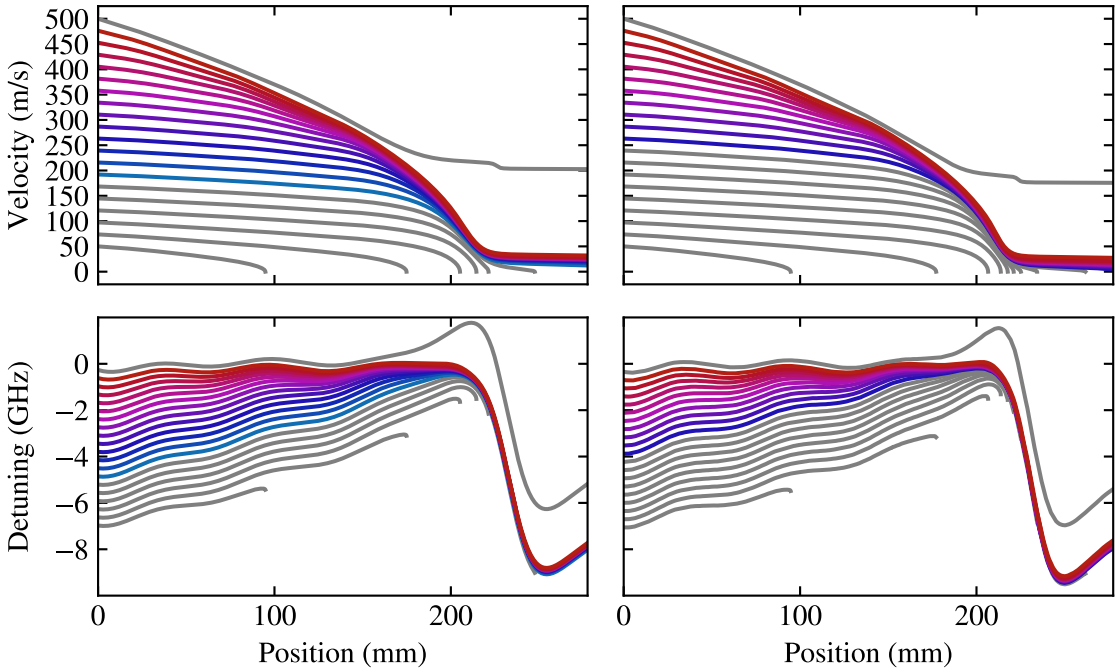

Figure 3.8.: Qualitative simulations of the propagation of atoms through the Zeeman slower. The left column shows the results for the field obtained by optimizing magnet positions in python. The right column shows the same simulation with the measured magnetic field of the Zeeman slower. Both velocity (upper row) and detuning (lower row) are plotted as a function of the position along the atomic beam path defined similar to Tab. 3.2 and Fig. 3.7. The detuning is calculated from the Doppler shifted and Zeeman shifted atomic transition and the frequency of the laser light. Different velocities are distinguishable by color. Grey lines correspond to velocities not being properly decelerated by the Zeeman slower.

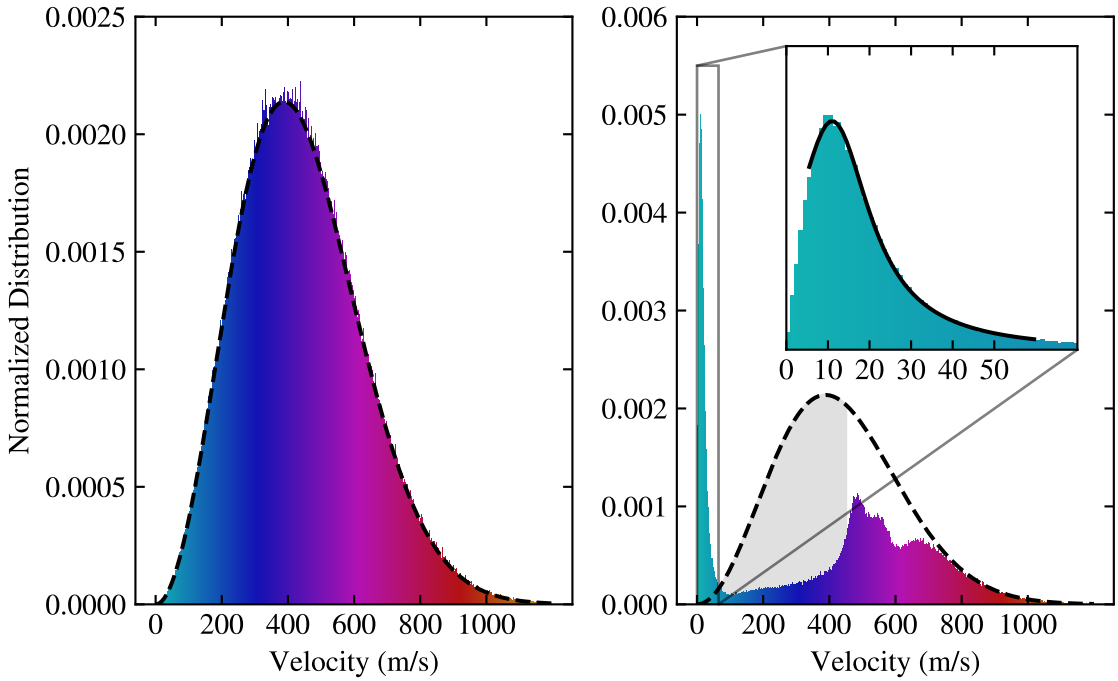

Figure 3.9.: Quantitative simulation on the propagation of 1.4×10^6 atoms through the Zeeman slower. On the left a histogram of the initial sample, following a Maxwell Boltzmann distribution (dashed line), is shown. A histogram of the sample after the ZS is shown on the right. A Voigt profile has been fitted to the peak that appears at small velocities (solid line). The dashed line is the same function as on the left. Velocities that are expected to be addressed by the ZS are shaded in gray.

4. Characterization of the Apparatus

The successful operation of a permanent magnet-based Zeeman slower relies not only on precise engineering of the device itself but also on a meticulously designed vacuum apparatus and well controlled sources of laser light. The latter, in turn, hinge upon the appropriate optical setup, which, while seemingly straightforward, reveals layers of complexity in its execution. To characterize the ZS, we work with two lasers of different wavelengths. The main laser source, used for slowing, operates at a wavelength of 421 nm, delivering a considerable power output of 800 mW. The second laser, emitting 626 nm light, is used to perform fluorescence spectroscopy on the atoms. In the course of our project, it became evident that precise magnetic field cancellation was indispensable as the splitting of Zeeman sublevels is the main broadening mechanism of spectral lines in the spectroscopy region. Following this brief overview, this chapter describes the experimental methodology employed to characterize the performance of the ZS.

4.1. Preparation of the Vacuum Apparatus

The vacuum apparatus has been set up using mostly commercial standard components and following the concept presented in Sec. 3.1. Only the small chamber (cube 1) intended for transversal cooling and probing of the atomic beam prior to the slowing has been omitted. A valve has been added to the only free port on cube 2 and is followed by a turbomolecular pump, which is connected via a flexible bellow. An oil-free scroll pump provides the backing pressure of approximately 10^{-2} mbar. The setup as it is, after several hours of pumping, reaches pressures of a few 10^{-8} mbar, i.e., high vacuum (HV). Although ultra high vacuum (UHV) conditions are not a strict requirement for testing the Zeeman slower, the apparatus was baked at 200 °C for three consecutive days. Following this procedure the oven was left running at a high temperature of 1200 °C for a few hours. Apart from outgassing and breaking the oxide layer on the Dy source material this step entails the deposition of Dy on the inside of the vacuum tubes. As this layer acts as a getter, the amount of residual gas is further reduced such that the final pressure reaches the low 10^{-9} mbar regime. Fig. 4.1 shows respective measurements with a residual gas analyzer (RGA) mounted close to the inlet of the turbomolecular pump. This shows that especially the abundance of water

molecules is strongly suppressed after baking. Other major residual gas molecules are H_2, N_2, CO, O_2 and CO_2.

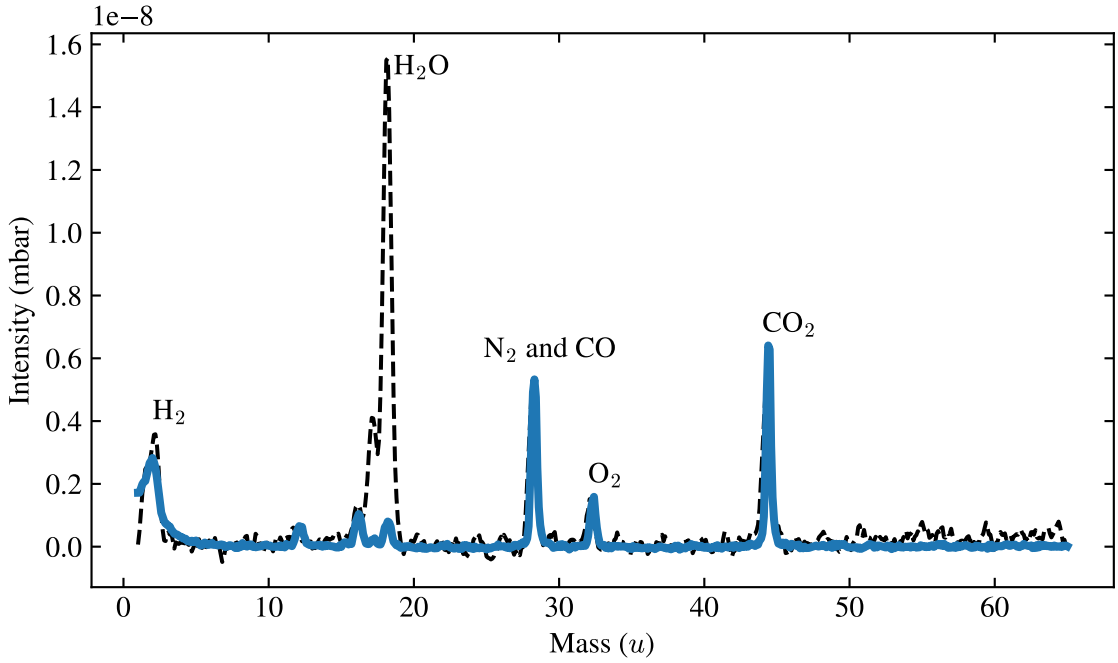

Figure 4.1.: Residual gas analysis. By means of mass spectrometry with an RGA, the absolute amount of typical residual gas molecules was measured before (black dashed line) and after (blue line) baking.

4.2. Optical Setup

The optical setup comprises two distinct components. The primary section, situated on an elevated breadboard, serves as the main setup responsible for manipulating and redirecting both the red and blue laser beams towards the atoms. A schematic overview is shown in Fig. 4.2. The secondary component, discussed in detail in Sec. 4.2.1, encompasses the modulation transfer spectroscopy (MTS), which we use to reference the blue laser to the 421 nm transition. We begin by describing the components and configuration of the blue laser system including the MTS, followed by a brief introduction to the new 421 nm vertical external cavity surface emitting laser (VECSEL) that has only recently been implemented. We then go through the fluorescence spectroscopy setup which has been utilized to perform measurements on the performance of the ZS, which are presented in Sec. 4.4.

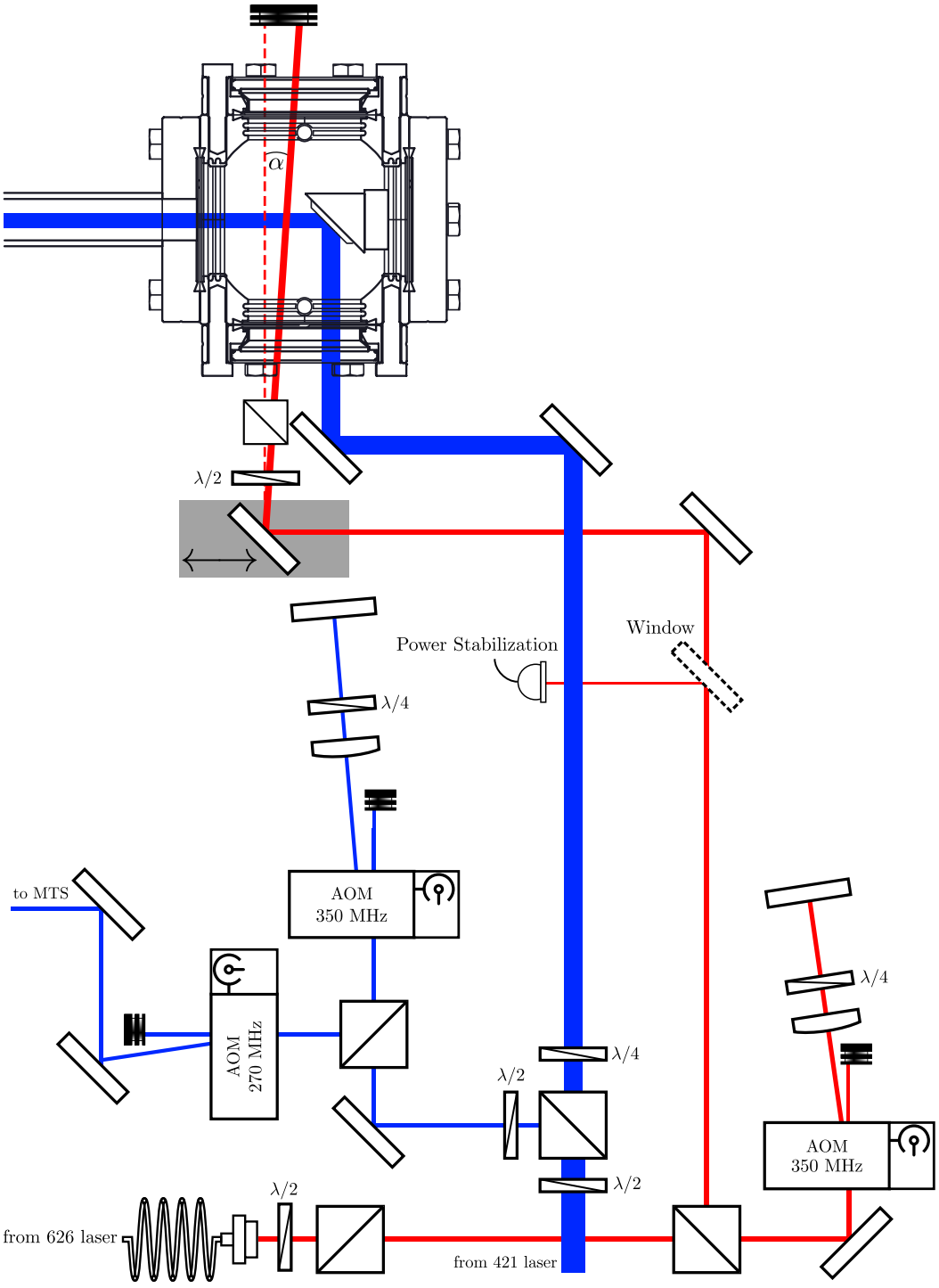

Figure 4.2.: Schematic overview of the main optical setup. The blue beam (slowing beam) enters the setup directly from the 421 nm laser system whereas the red beam (spectroscopy beam) is fibered from the neighbouring DynamiK experiment. Both wavelengths are discussed individually in the main text.

4.2.1. Locking of the Slowing Laser

Having a stable laser frequency available is a crucial perquisite in many atomic physics experiments. Our work is no exception in this regard as we require the frequency of the light for the Zeeman slower to be constant with respect to the 421 nm transition over the timescale of the experiment. However, depending on temperature, acoustic noise and other environmental effects, the frequency of any laser-source tends to drift over time. One can prevent that by active frequency stabilization or *locking* of the laser to a stable frequency reference. This can either be the eigenmodes of an optical cavity or the spectral lines of an atomic or molecular sample. Whilst ultra low expansion (ULE) cavities with high finesse are advantageous when high sensitivity for the realization of very narrow bandwidths is desired, they tend to drift over time and often feature excessive overhead. Appropriate implementations of such systems can be found, amongst others, in the realization of ultra-precise atomic clocks [103]. A commonly used alternative that offers long-term stability and simplicity at the price of higher bandwidth, is the locking to an atomic reference by means of different sorts of spectroscopy. Popular schemes include dichroic atomic vapour laser lock (DAVLL) [104, 105], polarization spectroscopy [106, 107], frequency modulation (FM) spectroscopy [108, 109] and modulation transfer spectroscopy (MTS) [110, 111].

For our purpose, we chose the long-established approach of locking the laser onto the slowing transition directly. This involves the realization of a saturated absorption spectroscopy (SAS) setup on which we perform modulation transfer spectroscopy to generate an error signal. Said signal features a dispersive lineshape that is used to stabilized the laser via a proportional–integral–derivative (PID) controller. With the use of a double pass acousto-optical modulator (AOM) followed by a single pass AOM, a small portion of the blue beam is frequency-shifted by a fixed frequency of 954 MHz before entering the MTS locking setup. This results in the major portion of the beam being detuned by said frequency below the atomic transition. Features, advantages and drawbacks of this technique, as well as the details of the spectroscopy setup, shall be described in the following section.

Theory of an MTS Signal

The technique of modulation transfer spectroscopy (MTS) is not new, but has been used in microwave spectroscopy [112] long before the advent of electro-optical (EOM) and AOM made it transferable to the optical domain. Several factors make an MTS setup a favorable choice for our experiment. Firstly, MTS being a SAS technique, eliminates Doppler broadening, which is a limiting factor in single-beam methods such as DAVLL. Secondly, compared to frequency modulation spectroscopy, where non cyclic transitions are pronounced in the signal, MTS enhances closed transitions. The resulting dominance of closed transitions in the signal of MTS is particularly beneficial,

as Dy offers a plethora of unwanted non-cyclic transitions. Additionally, MTS readily provides a dispersive lineshape that is amenable for locking. And lastly, the technique does not feature a background signal, i.e., the zero crossings of the dispersive lineshape occur exactly at the position of the atomic transition.

Similar to other saturated absorption spectroscopy setups, MTS uses two counter-propagating laser beams of the same source that we refer to as pump- and probe beam respectively. These beams intersect a cell filled with atomic vapor where they overlap. The intensity of the probe beam after the cell is measured by a detector. However,opposite to standard frequency modulation spectroscopy, not the probe, but the pump beam is phase[1] modulated with some frequency ω_m and modulation index β such that sidebands are inscribed on the spectrum. The electric field thus can be written as a sum of frequency components separated by ω_m with proportionality constants given by the Bessel functions $J_n(\beta)$ of order n

$$E_\mathrm{pump}(t) = E_0 \left[\sum_{n=0}^{\infty} J_n(\beta)\sin(\omega_\mathrm{c} + n\omega_\mathrm{m})t] \sum_{n=1}^{\infty}(-1)^n J_n(\beta)\sin(\omega_\mathrm{c} - n\omega_\mathrm{m})t\right], \quad (4.1)$$

where ω_c is the carrier frequency. It is usually sufficient to assume $\beta \ll 1$ and thus only consider the first-order sidebands at frequencies $\omega_\mathrm{c} \pm \omega_\mathrm{m}$. If nearly resonant with an atomic transition, the pump beam interacts with the vapor and the counter-propagating probe beam in a nonlinear manner described by four-wave mixing [113], such that modulation is transferred from the pump beam to the probe beam. The dominant process for modulation transfer is called modulated hole burning. The modulated pump beam saturates distinct parts of the atomic velocity distribution, i.e., "burns" holes. These are separated by the oscillation frequency. The probe beam resonantly interacts with said holes and acquires varying amplitude modulation when the carrier frequency is scanned across the resonance. In first-order sideband approximation and neglecting higher order terms, the result is a signal of the form

$$\begin{aligned} S(\omega_\mathrm{m}) \propto \frac{J_0(\beta)J_1(\beta)}{\sqrt{\Gamma^2+\omega_\mathrm{m}^2}}\big[&(L_{-1} - L_{-1/2} + L_{1/2} - L_1)\cos(\omega_\mathrm{m}t + \phi) \\ &+(D_1 - D_{1/2} - D_{-1/2} + D_{-1})\sin(\omega_\mathrm{m}t + \phi)\big], \end{aligned} \quad (4.2)$$

with $L_n = \Gamma^2/(\Gamma^2 + (\delta - n\omega_\mathrm{m})^2)$, $D_n = L_n(\delta - n\omega_\mathrm{m})/\Gamma$ and δ being the detuning of the laser light from resonance and ϕ being the phase of the signal at the detector with respect to the signal that has been used to modulate the pump beam. The amplitude of the first first (second) term in Eq. (4.2) is referred to as in-phase (quadrature) component. This signal is then mixed with the modulation signal of the form

[1] It should be noted that phase modulation and frequency modulation are equivalent in terms of the resulting electric field. It is however more feasible experimentally to perform phase modulation which is why it is preferably used.

$S_{\mathrm{mod}}(\omega_{\mathrm{m}}) \propto \sin(\omega_{\mathrm{m}} t)$ to eliminate the rapidly oscillating part. One can think of this phase-sensitive detection scheme as a transformation

$$L\cos(\omega_{\mathrm{m}} t + \phi) + D\sin(\omega_{\mathrm{m}} t + \phi) \longrightarrow L\cos(\phi) + D\sin(\phi), \tag{4.3}$$

with L and D being the in-phase and quadrature component respectively. In this way, by adjusting the phase between the modulation signal and the detector signal, one can select either one of these two components or a mix of them. Given that the modulation frequency is smaller than the transition rate of the atomic transition of interest, i.e., $\omega_{\mathrm{m}} \leq \Gamma$, both components show a dispersive-like lineshape with the zero-crossing sitting on resonance. One usually finds the best signal with largest gradient and maximum peak to peak amplitude for an admixture of quadrature and in-phase component. Fig. 4.3 shows examples of MTS signals for different ratios between in-phase and quadrature components. In Fig. 4.4, the gradient and peak-to-peak amplitude of such a signal is shown as a function of the modulation frequency. From an analysis of theoretical peak-to-peak amplitudes and gradients shown, we find that a ratio $\omega_{\mathrm{m}}/\Gamma \approx 0.7$ and a phase $\phi \approx 50°$ is a good choice for laser locking, where we aim at wide capture range and high sensitivity respectively. An optimum for both parameters can not be achieved simultaneously. Also, in the experiment we are required to tune the modulation frequency to the resonance frequency of the EOM to maximize the modulation index in Eq. (4.2). Further considerations for experimental realization, are addressed in the subsequent section.

Experimental Realization

Various problems and delays in the laboratory made it necessary to adapt to different laser sources several times. Thus, the setup is built on a movable 45 cm × 35 cm breadboard but uses up only half the available space. This allows for additional optics being assembled besides, when needed. A schematic of this setup is shown in Fig. 4.6. The light enters the setup from the main optical setup shown in Fig. 4.2. The light is collimated by a lens of focal length $f_1 = 6.2\,\mathrm{mm}$ inside of the fiber coupler and is then guided into a polarizing beam splitter (PBS) after passing a half-wave plate ($\lambda/2$) for adjusting the polarization. In this way one can adjust the relative intensities of the pump beam (horizontal polarization, going straight through the PBS) and the probe beam (vertical polarization, redirected by the PBS).

The pump beam is then coupled into a homemade Brewster-angled EOM, where it is phase modulated at the resonance frequency of the EOM. Said resonance frequency can be determined and tuned by varying the components shown in the circuit diagram of the EOM in Fig. 4.5 (right). The EOM, by definition has a certain fixed capacity C_{c}, where the crystal acts as the dielectric layer. An additional capacitor (inductance) in parallel (series) can be added to form a resonant circuit. The strongest modula-

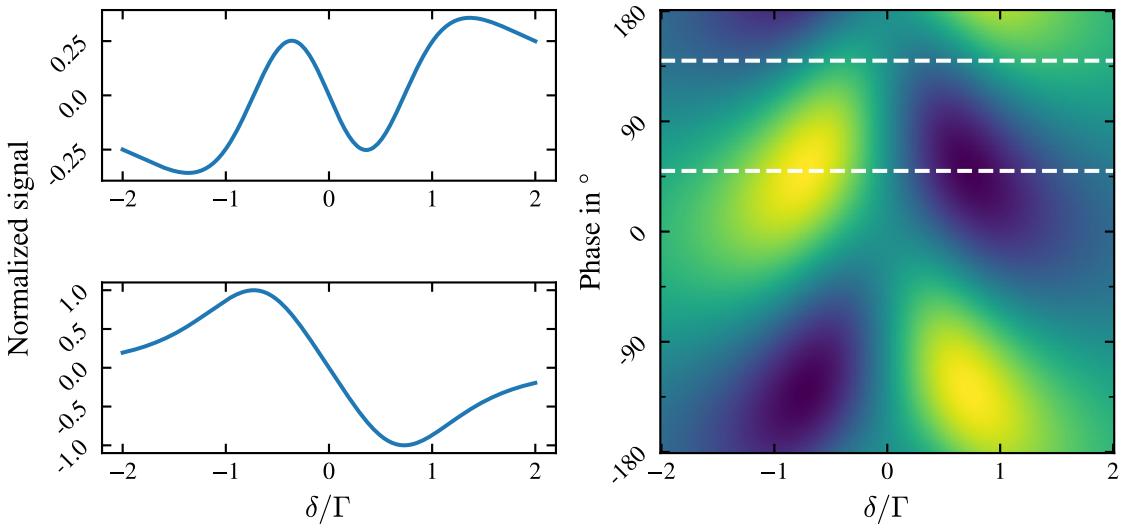

Figure 4.3.: Theoretic MTS signal. The contour plot on the right shows the MTS signal as a function of both the phase ϕ and the detuning from resonance. A modulation frequency of 0.67Γ that we use in the experiment, was chosen. On the left two horizontal cuts show the signal as a function of the detuning at fixed phase. The upper (lower) white dashed line on the right indicates the phase for the upper (lower) plot on the left. The upper plot is an example for a signal not suitable for locking, whereas the lower plot shows the desired characteristics.

tion is possible at the resonance frequency of the circuit and for the total impedance matching the $50\,\Omega$ output impedance of any function generator. Therefore, we also use a resistor R_s in series. The components are chosen such that the resonance approximately satisfies $\omega_\mathrm{m}/\Gamma \approx 0.7$ as justified in the preceding section. The presence of uncontrollable effects, such as the inductance and capacitance of the circuit housing makes some "trial and error" process necessary for finding the correct components. As shown in Fig. 4.5 (left) the resonance is located near 21.3 MHz, i.e., $\omega_\mathrm{m}/\Gamma \approx 0.66$

The laser-beam is now redirected to intersect the hollow cathode lamp. This is a metal-vapor discharge lamp consisting of a cathode made from dysprosium, an anode and argon as a buffer gas. We apply a voltage on the order of 200 V between cathode and anode to generate an atomic vapor that is visible as blue glow. The probe is not modulated and passes through the hollow cathode lamp collinearly, but in opposite direction, such that the beams overlap in the region where the atomic vapor is generated. The probe beam is then picked up by another PBS and focused onto a photodiode (PD). For demodulation, the resulting signal is mixed with the signal that drives the EOM. The phase of said two signals, with respect to each other, can be adjusted. By scanning the laser across the desired 421 nm resonances, we obtain a signal that features a dispersive lineshape and can be used to lock the laser. We shall

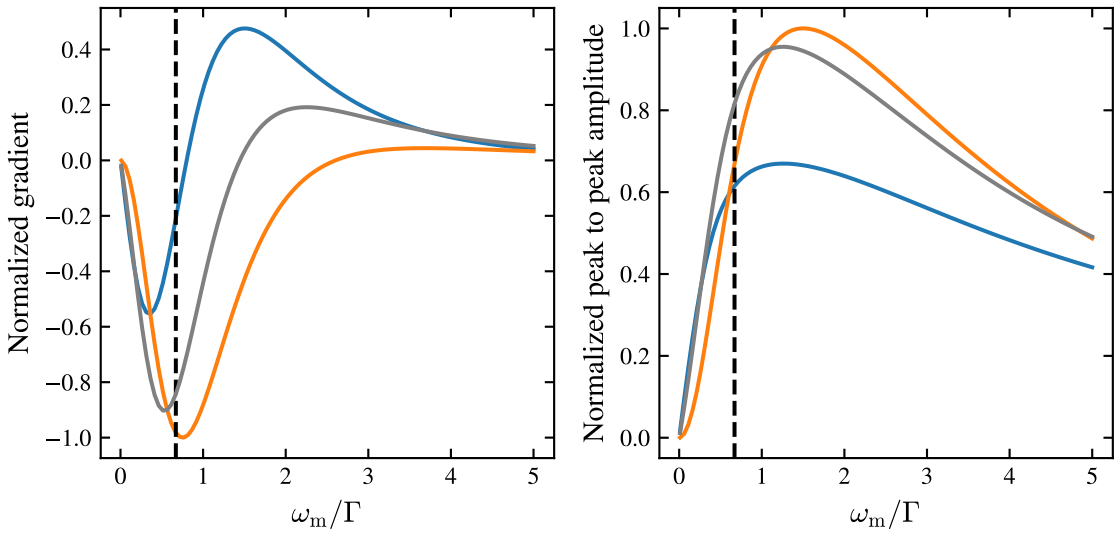

Figure 4.4.: MTS signal characteristics as a function of the modulation frequency. On the left, the normalized gradient at the position of the resonance is shown for the in-phase ($\phi = 0$ blue) and quadrature ($\phi = \pi/2$, orange) component respectively. The grey line represents an equal mixture, i.e., $\phi = \pi/4$. On the right, the normalized peak to peak amplitude is shown for the same three cases. The black dashed line indicates the modulation frequency $\omega_m = 0.67\Gamma$ that is used in the experiment.

have a look at these results in the following section.

Characterization of the MTS Error Signal

Following a careful adjustment of the describe setup, an error signal has been found and optimized such that a pattern as shown in Fig. 4.7 has been observed when scanning the laser frequency across a range of roughly 2 GHz. We find the signal with maximum peak to peak amplitude for a ratio of $P_{\text{Probe}}/P_{\text{Pump}} = 0.76$, where P_{Probe} (P_{Pump}) is the power of the probe (pump) beam. Also, the phase between the signal recorded by the photodiode and the signal used to drive the EOM has been adjusted to maximize the signal as well as the gradient. Its exact value, however, is not accessible due to the design of the device used for demodulation.

Apart from the dominant transitions of the bosonic ^{164}Dy and ^{162}Dy isotopes, which we will mainly use for locking, we are also able to resolve the hyperfine structure of the fermionic ^{161}Dy and ^{163}Dy [52]. A detailed listing of the hyperfine components and isotope shifts has also been given in Tab. 2.2. A fit of the form $V(f) = k(f - f_0)$ has been applied to the two bosonic resonances, where V is the voltage, k is the gradient, f is the frequency and f_0 is the central frequency of the respective transition. For the ^{164}Dy feature, we obtain a gradient, i.e., lock sensitivity of $-0.930(6)\,\text{mV}\,\text{MHz}^{-1}$,

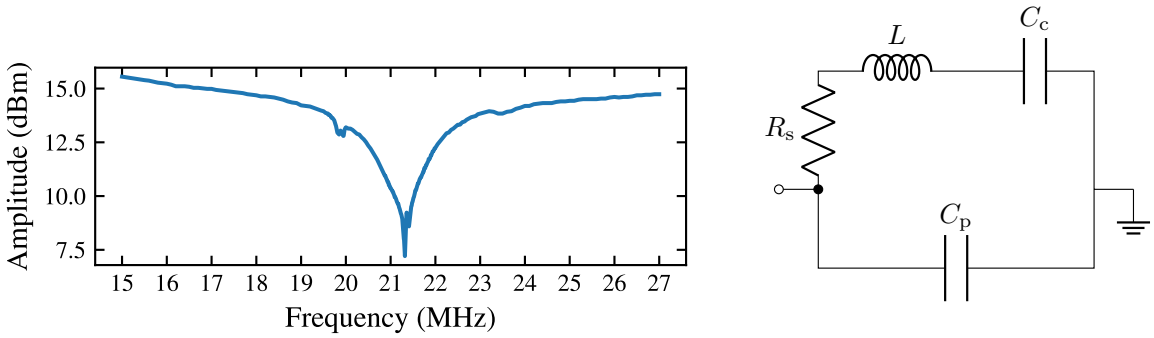

Figure 4.5.: EOM characteristics. The plot on the left shows the amount of reflected RF-signal as a function of the frequency. On the right, a schematic circuit diagram of an EOM is given, with R_s being the resistance of the wires plus some additional resistor for impedance matching, L an inductor, C_c the capacitance of the crystal itself and C_p a capacitor connected in parallel.

whereas in case of ^{162}Dy, we obtain $-0.742(7)\,\mathrm{mV\,MHz^{-1}}$. The peak to peak amplitude is 25.48(5) mV and 32.76(5) mV respectively. We will see in the following section how these signals can be used to lock a laser system to one of the two atomic transitions.

4.2.2. Implementation of the New 421nm Laser System

To replace a malfunctioning Msquared Tisaph laser system that was initially intended to be used for the project, a new commerical VALO SHG SF from Vexlum [114] has been purchased to test the cold atom source and then serve as an integrated part of the NewLanD experiment. This new system is a vertical external cavity surface emitting laser (VECSEL) with intracavity frequency doubling. A schematic of the device is shown in Fig. 4.8 (a). The basic working principle is the following: A precisely temperature controlled gain mirror is optically pumped, typically with a diode laser. The gain mirror consists of a distributed Bragg reflector (DBR), followed by an active region composed of several quantum wells that are spaced at half of the wavelength of 842 nm emitted from the gain medium. The different layers are formed by epitaxy. A schematic of the bandgap as a function of the distance z from the base substrate is shown in Fig. 4.8 (b). The gain mirror, together with a piezo mounted end mirror and fold mirror forms a V-shaped cavity which enforces a circular, nearly diffraction limited beam. Between the end mirror and the fold mirror a crystal[2] is doubling the laser frequency by second harmonic generation (SHG). As the fold mirror is highly reflective for 842 nm but has low reflectivity for 421 nm, the resulting blue beam is emitted from the cavity through the fold mirror. Inside of the cavity there also is

[2]The specific type of crystal used in our commercial system is not known to us. Typically either BBO, LBO, KTP or DKDP is used for SHG in laser cavities.

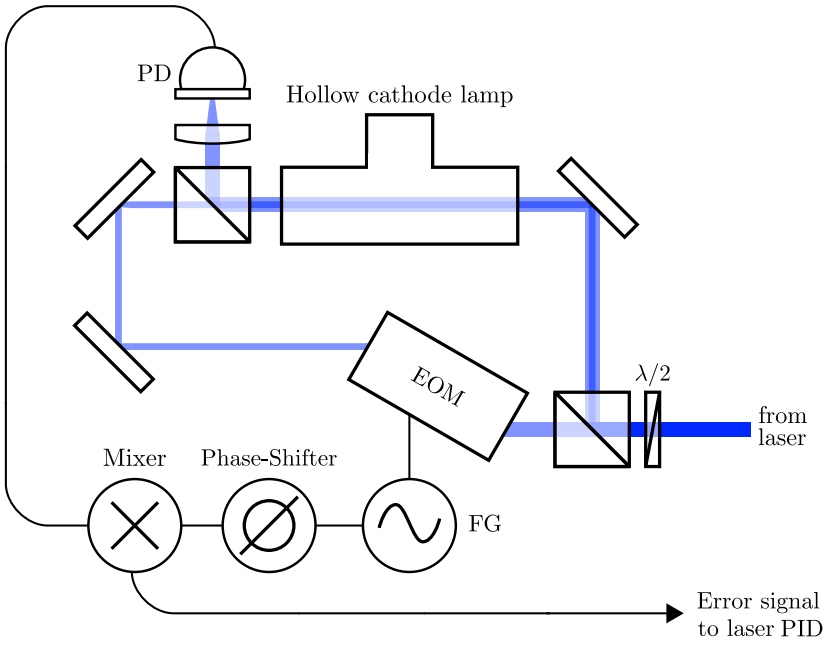

Figure 4.6.: Schematic overview of the spectroscopy setup. The beam, coming from the main setup, passes a half-wave plate ($\lambda/2$) before it is split into the lower (pump) and higher (probe) beam by a polarizing beam splitter (PBS). The pump beam is phase modulated with an electro-optic modulator (EOM) and, after being redirected by two mirrors, intersects the atomic vapor inside the hollow cathode lamp. The probe beam overlaps the pump beam inside of the lamp, where the modulation is transferred, and is then redirected by another PBS before being focused into a photodiode (PD). The signal of the PD is mixed with the eventually phase shifted signal sent to the EOM by a function generator (FG). The resulting signal is fed back into the laser source for active frequency stabilization.

an etalon and a rotatable birefringent filter (BRF) which allow for selection of the desired frequency mode. Both elements, as well as the SHG crystal can be tuned via temperature. Two piezos at the end mirror can be individually addressed for frequency scanning and locking.

With this basic understanding of the blue laser and the aforementioned parameters that can be varied to tune, optimize and stabilize the light's frequency, we performed basic characterization measurements, some of which are shown in Fig. 4.9, to gain further insight into the behaviour of the system [3]. We now go through the various parameters that can be used to tailor the laser to a specific wavelength one by one, beginning with the laser diode driver (LDD). The LDD drives a current of up to 1300 mA through the laser diode used to pump the gain medium optically. One can

[3] A full list of the parameters used for stable operation is given in Tab. A.1.

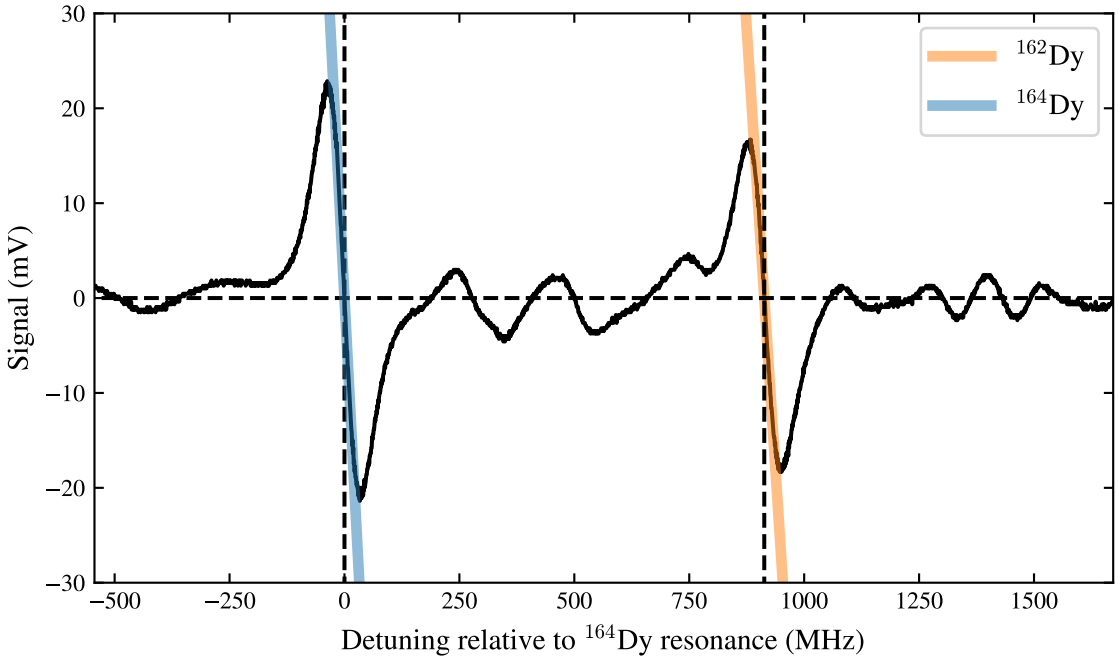

Figure 4.7.: MTS error signal averaged over 16 frames. The most pronounced features represent the 421 nm transition of the two most abundant bosonic isotopes ^{164}Dy (left) and ^{162}Dy (right) where a linear fit has been applied that is shown in blue and orange respectively. The vertical (horizontal) dashed lines indicate the centers of the resonances (zero background). The respective results are given in the main text.

see that the laser tends to modehop to higher wavelengths when the current is ramped up. In general we found that the system is the most stable for maximum current and the LDD current should not be used to tune the wavelength or reduce the output power. It can, however, be ramped down and up again to reset the laser after an undesired modehop to a far-away mode. The laser is specified for being tunable between 421.08 nm and 421.49 nm. For coarse tuning one has to access the BRF from the top of the laser housing. By rotating the BRF by small angles[4] one can tune in steps of 0.3 nm. The temperature of the SHG crystal and the BRF itself should be optimized after such tuning step. For smaller wavelength increments one uses the temperature of the etalon. Only the finest wavelength changes of less than 10^{-3} nm can be done by tuning the piezo voltage with a tuning coefficient of $1.8 \times 10^{-2}\,\mathrm{pm\,V^{-1}}$. We therefore use a home-built laser PID controller with an external pre-amplification stage to enlarge the error signal shown in Fig. 4.7 and an additional high-voltage amplifier after the PID to cover the whole voltage range of 150 V across which we can tune the piezo.

With this scheme, we achieve wavelength stability on the order of the natural

[4]Figure A.1 in the Appendix shows the original position of the BRF.

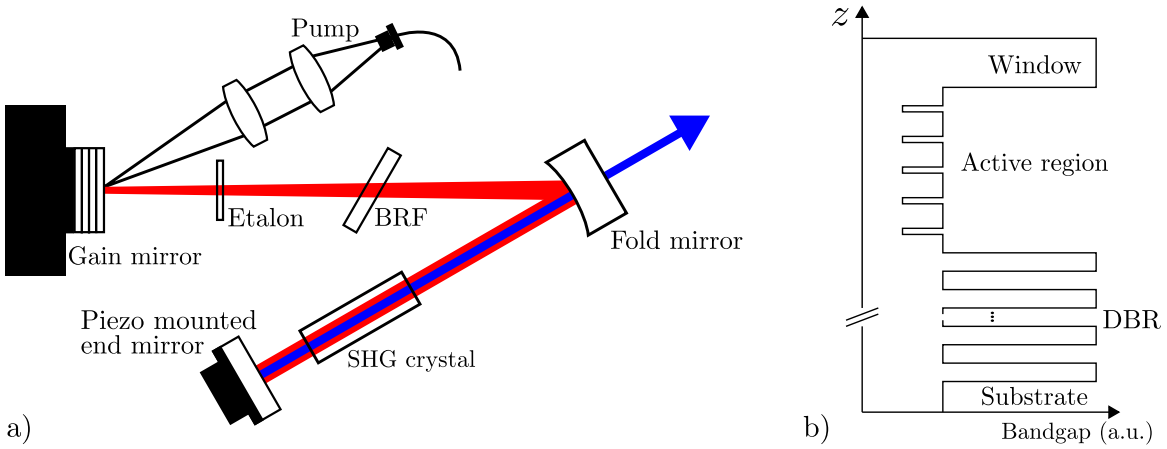

Figure 4.8.: Schematic of a VECSEL laser with intracavity frequency doubling. The components of the V-shaped cavity are shown and labeled in (a). A closeup of the bandgap for the different layers on the gain mirror is shown in (b). A more detailed description and definitions for abbreviations can be found in the main text.

linewidth of the 421 nm transition over several hours. The emitted power is on the order of 800 mW. It should be noted that the laser has been tested for a relative humidity of 18 % and specifications can vary for different laboratory environments.

While a small portion of the beam emitted from the VECSEL system is redirected to realize the aforementioned MTS error signal, the majority of the light coupled into the main chamber where an in-vacuum mirror redirects the light antiparallel to the atomic beam. The polarization is right-handed such that we excite the σ^+ transition at the start and the σ^- transition at the end of the ZS.

4.2.3. Fluorescence Spectroscopy

The red light is generated by sum frequency generation of two high-power infrared beams and stabilized by locking to a high-finesse cavity in the neighbouring Dy-K lab [30]. A small portion of the total output power of said system is coupled into a newly installed fiber link between our laboratories and serves as the starting point for our own fluorescence imaging setup. After a half-wave plate and polarizing beam splitter used to clean the polarization and adjust the power, the beam is frequency shifted by an AOM in double pass configuration. The provided light is locked to 78 MHz below the resonance of the fermionic ^{161}Dy isotope. The AOM thus bridges the isotope shift to the most abundant bosonic ^{164}Dy isotope, but also allows for scanning the frequency of the light to excite atoms with different velocities. To prevent power fluctuations from interfering with the measurement, the beam is power stabilized before being sent to the atoms. As we will see in the following section, both alignment and polarization of the imaging beam with respect to the motion of the atoms is crucial for the measurement.

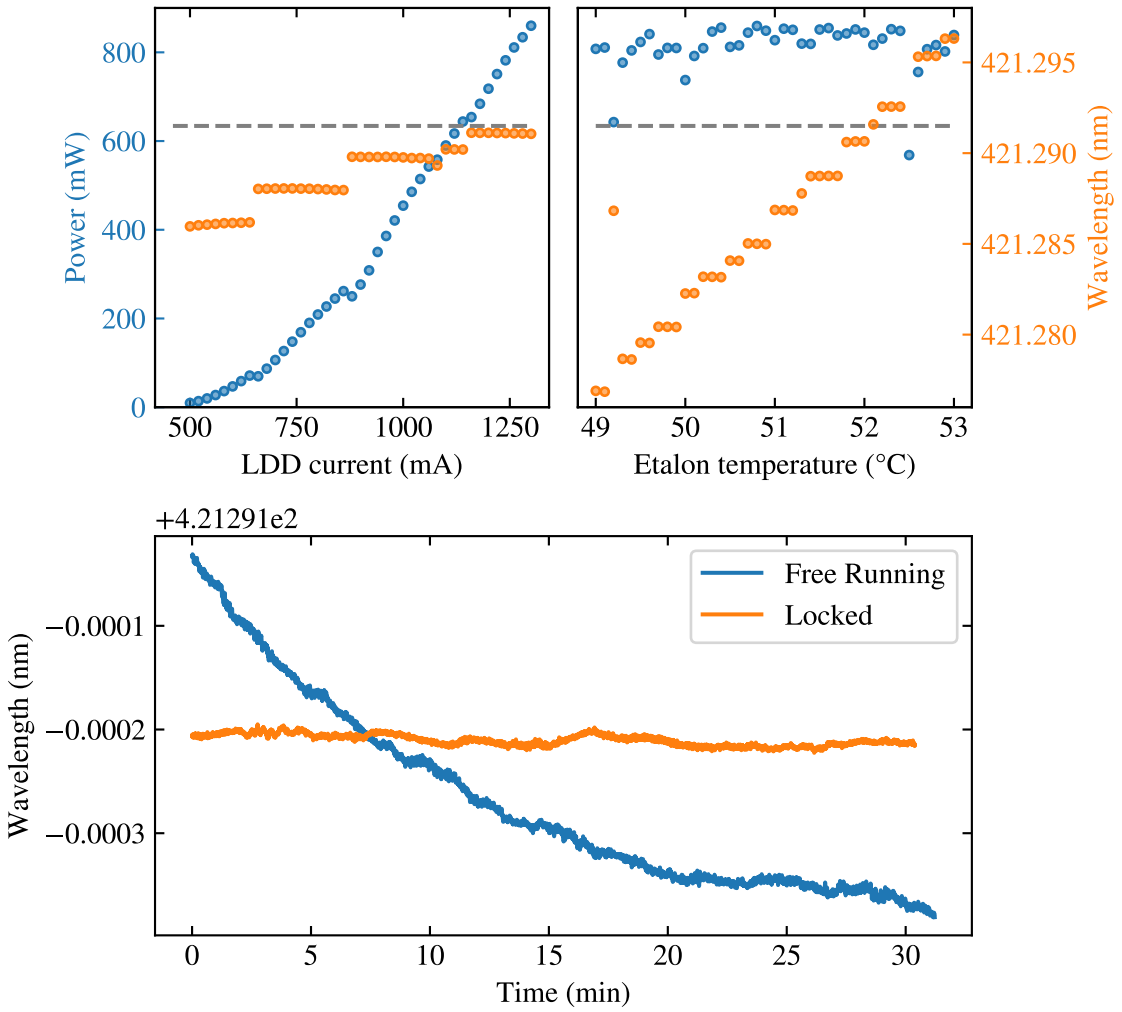

Figure 4.9.: VALO SHG characterization. The power (blue) and wavelength (orange) as a function of the laser diode driver (LDD) current and the etalon temperature is shown on the upper left and right respectively. The gray dashed line indicates the operating wavelength for the Zeeman slower. The lower plot shows the wavelength as a function of time when the laser is freely running (blue) and locked (orange) to the MTS.

We thus place the last mirror on a translation stage to realize different angles α while maintaining a fixed point of intersection with the atomic beam where the fluorescence is tightly focused into a photon multiplying tube (PMT).

4.3. Magnetic Field Cancellation

First attempts on obtaining a fluorescence signal have shown that the red transition is broadened in frequency to an extend where no information can be extracted from the

spectroscopy. We identified the dominant broadening mechanism[5] to be the Zeeman splitting of the magnetic quantum number manifold. By extending the measurements of the magnetic field of the ZS to the region where the spectroscopy signal is obtained, we find that the remaining field is still on the order of several tens[6] of G, as shown in Fig. 4.10. Furthermore, as a minor effect, the magnetic field in transversal direction due to the ZS and the earth's magnetic field is on the order of a few G. Given the Landeé g factor of the ground state, given in Sec. 2.1, and the excited state $g_\mathrm{e} = 1.29$, and $m_\mathrm{g} = \{-8, \ldots, 8\}$ and $m_\mathrm{e} = \{-9, \ldots, 9\}$ for the ground and excited state respectively, we find a frequency shift of $\Delta f = \mu_\mathrm{B} h^{-1} B \left(m_\mathrm{g} g_\mathrm{g} - m_\mathrm{e} g_\mathrm{e}\right)$. As a result, we indeed expect the transition to be spread out over several tens of MHz, as can also be seen in Fig. 4.10.

To cancel the magnetic field to a point where meaningful information can be extracted from the spectroscopy we developed an assembly of coils, shown in Fig. 4.11. For the two transversal directions[7] we use two pairs of small Helmholtz coils wound over 3D-printed structures. These are held by the viewports of the vacuum chamber and are additionally designed such that they block most of the ambient light for a better signal to noise ratio in the spectroscopy. We drive moderate currents on the order of a few A through the small coils. For the longitudinal direction a single coil with a large inner diameter of 16 cm has been constructed. The size has been chosen to be able to mount it around the vacuum apparatus without breaking vacuum. On a test setup we performed the characterization measurements presented in Fig. 4.12 with the large coil. The magnetic field has been measured at the approximate distance of the spectroscopy beam from the coil. The coil is heating up slow enough such that we do not require short pulses of current.

After mounting the coils we set the angle between the atomic beam and the spectroscopy laser beam to $\alpha = 90°$ and minimized the width of the spectroscopy signal shown in Fig. 4.13. This was done by varying the current provided by three individual power supplies to cancel the magnetic field with the compensation coils. A small magnetic field in z direction remains and sets the quantization axis. With the light being polarized horizontally, we thus only excite the π transition. The broadening of the transition is now on the order of the Doppler broadening and could not be further reduced. We account this broadening to a systematic uncertainty in the magnetic field as well as magnetic field noise introduced by the power supply of the large coil.

[5] By collecting fluorescence through an adjustable aperture and by varying the power of the probe beam we could rule out Doppler broadening and power broadening as the main limitation respectively.

[6] A more precise value for the magnetic field can not be given because it can only be measured by removing the ZS from the vacuum apparatus and mounting it separately to have access with a magnetometer. The precise position of the fluorescence spectroscopy beam with respect to the magnet assembly is therefore the predominant systematic uncertainty.

[7] The coordinate system is defined in accordance with Sec. 3.3.4.

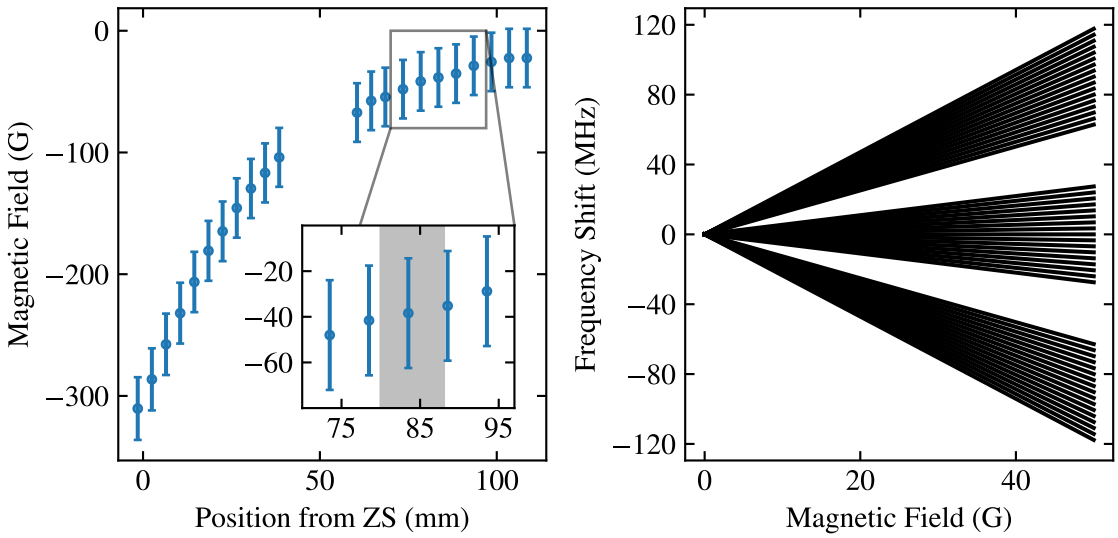

Figure 4.10.: Measured magnetic field and calculated Zeeman splitting for the spectroscopy region. On the left the measured magnetic field is shown as a function of the position after the end of the ZS. The gray shaded area is an estimate for the position of the fluorescence spectroscopy beam. Error bars result from the specified 1σ uncertainty of the magnetometer. On the right we show a calculation of the frequency shift of the 626 nm transition as a function of the magnetic field for each pair of ground- and excited-state magnetic quantum numbers. The lower, middle and upper group of lines correspond to the σ^-, π and σ^+ transitions respectively.

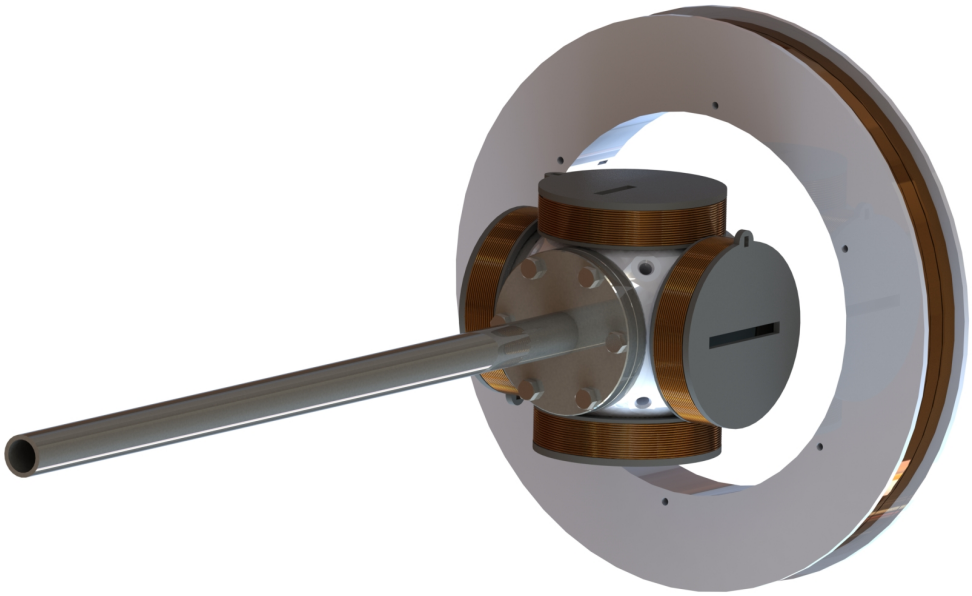

Figure 4.11.: Rendering of the magnetic field compensation coil setup. For better visibility, the ZS that is mounted on the vacuum tube has been removed.

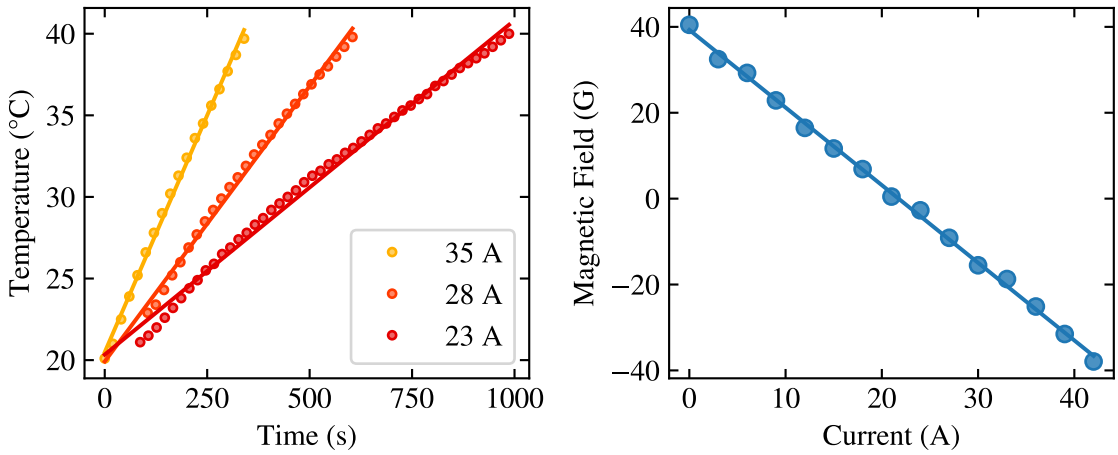

Figure 4.12.: Large compensation coil characterization measurements. The left plot shows the temperature of the coil as a function of time for different currents. Linear fits yield heating rates of $5.81(8) \times 10^{-2}\,°\mathrm{C\,s^{-1}}$, $3.37(5) \times 10^{-2}\,°\mathrm{C\,s^{-1}}$ and $2.05(3) \times 10^{-2}\,°\mathrm{C\,s^{-1}}$ for 35 A, 28 A and 23 A respectively. On the right, we show the magnetic field as a function of the current at the position of the spectroscopy beam with the ZS mounted. We obtain a slope of $-1.808(2)\,\mathrm{G\,A^{-1}}$ and a zero-crossing at 21.73(15) A from the linear fit.

4.4. Results and Limitations

To finally characterize the ZS by means of fluorescence spectroscopy the 626 nm beam is tilted by $\alpha = 1.208(12) \times 10^{-2}$ rad from the transversal direction (see also Fig. 4.2 for reference). The atomic velocity v in longitudinal direction is a function of the laser wavelength λ, the angle α and the light's relative frequency with respect to the atomic transition $f - f_0$ that we obtain from the transversal spectroscopy shown in Fig. 4.13

$$v = (f - f_0)\,\frac{\lambda}{\sin\alpha}. \tag{4.4}$$

After this transformation we obtain the data shown in Fig. 4.14 with and without the blue ZS light in the vacuum chamber. When we compare these results with the simulations presented in Sec. 3.4 we must take into account the fact that, due to the broadening of the signal, the expected velocity distribution is smeared out. By calculating the convolution of the fitted curve, shown in Fig. 4.13 with the simulation initial values and simulation results we get a prediction that is actually comparable to the measurements. The data shows a clear signature of slowed atoms. We find that for velocities higher than $330\,\mathrm{m\,s^{-1}}$ the measured velocity distribution after the ZS qualitatively matches our prediction. For lower velocities we see the effect of the magnetic field compensation that is effectively destroying the magnetic field towards the end of the ZS. As a result, the atoms are decelerated to around $170\,\mathrm{m\,s^{-1}}$ rather than the expected few tens of $\mathrm{m\,s^{-1}}$. This limitation was anticipated and is attributed

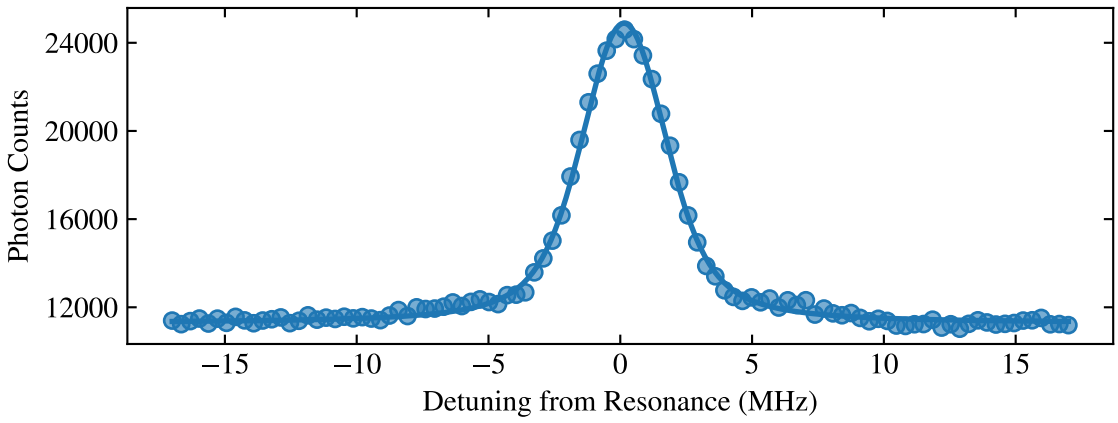

Figure 4.13.: Transversal fluorescence spectroscopy signal. Photon counts in 2 s time-bins are plotted as a function of the detuning of the 626 nm light that is exciting the atoms. The laser beam is perpendicular to the atomic beam. A Voigt profile with a full width at half maximum (FWHM) of 3.86(6) MHz has been fitted to the data points. The error bars arising from a Poissonian distribution are smaller than the data points and therefore not shown.

to the characterization apparatus rather than the ZS itself. Despite this, it is noteworthy that the relative amount of atoms with velocities in the few tens of $\mathrm{m\,s^{-1}}$ is comparable to the simulation, indicating that overslowing is more dominant for the unperturbed magnetic field used in the simulation. This emphasizes that the magnetic field towards the end of the ZS is the critical factor affecting the final velocity distribution. Importantly, our results demonstrate the effective deceleration of atoms and validate the design and simulation approach and serve as a promising proof of principle.

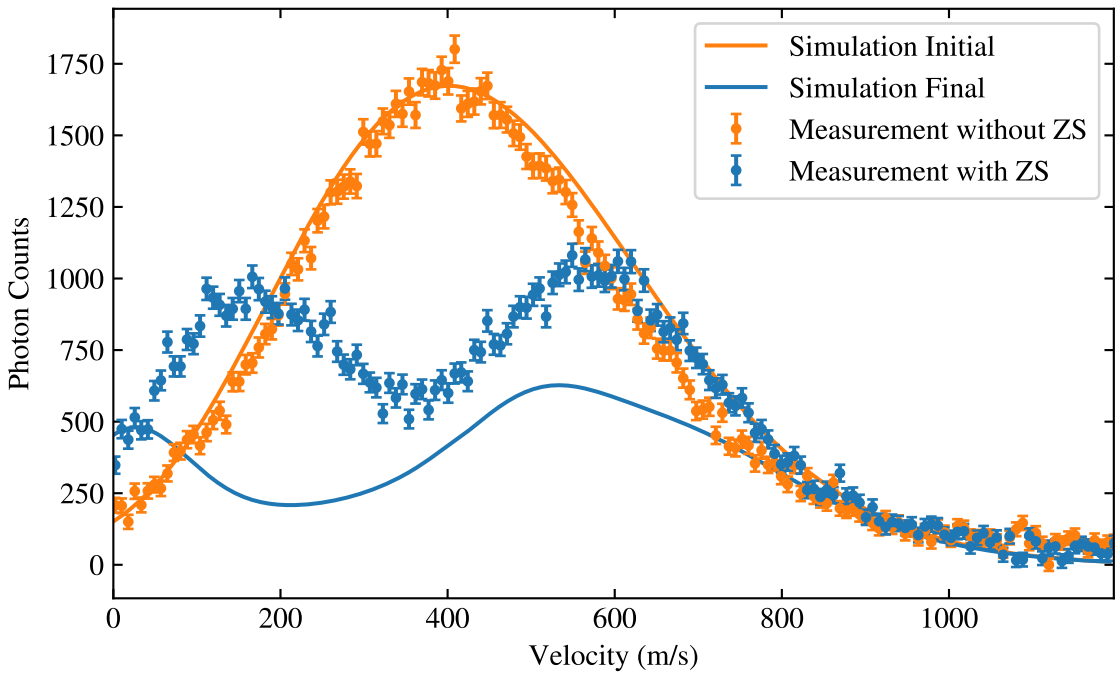

Figure 4.14.: Characterization of the ZS. The data points show fluorescence spectroscopy measurements with the ZS light being off (orange) and on (blue) respectively. A constant background has been subtracted. Solid lines illustrate the initial and final values of the simulation. The simulation has been normalized to the maximum of the orange data points. As the data has been obtained from counting photons, error bars originate from the Poisson distribution.

5. Conclusion and Outlook

Motivated by the rich set of properties of dysprosium, which were briefly laid out in Chap. 2, the aim of this thesis was to describe the design, construction and characterization of a permanent magnet Zeeman slower for this element. The former two topics have been extensively covered in Chap. 3 and supplemented with qualitative and quantitative simulations of the device. Starting from the idea of a stand-alone proof of principle experiment outlined in Sec. 3.1, we discussed each part individually, beginning with the atomic beam emerging from an effusive source in Sec. 3.2. The essential element of this work, the Zeeman slower itself, is then described in Sec. 3.3 and simulated in Sec. 3.4. The use of permanent magnets and the engineering techniques that differ from regular ZS setups have been emphasized. In Chap. 4 the final characterization together with the optical setup, laser systems and stabilization schemes has been described. Especially the implementation of a new 421 nm laser system and the creation of a MTS locking scheme have been covered in detail.

In conclusion, we can report on the realization of a magnetic field profile with a tunable set of permanent magnets that is in good agreement with the calculated field. We furthermore see by means of fluorescence spectroscopy that a portion of atoms, with initial velocities below the capture velocity of the ZS, are decelerated up to a point where the magnetic field compensation of the spectroscopy setup negatively impacts the ZS field. A full characterization of the ZS can, thus, not be given yet.

The easiest approach to overcome this limitation is to lengthen the vacuum tube that holds the ZS to increase the distance from the permanent magnets to the spectroscopy region. A more practical, yet more complex method is to characterize the performance of the ZS by adding a 3D MOT and observing the loading rate instead of measuring the velocity distribution directly. To not compromise the requirement for a highly compact ZS, however, the design process would have to be repeated and optimized for the reduction of stray fields that affect the following experimental stages. This could be done by positioning smaller magnets closer to the atomic beam. Such an approach has been ruled out previously due to the associated need to build the device inside vacuum. Now that many of the technical challenges have been overcome, this could be a realistic possibility.

A. Appendix

A.1. Vexlum Valo Parameters

Table A.1.: Vexlum VALO SHG parameters for stable operation at 421.291 nm for a relative humidity of 18 %.

	Setpoint (°C)	Range (°C)
Gain Medium	13.000	Not to be changed
SHG Crystal	65.000	±2.0
BRF Filter	43.700	±1.5
Etalon	51.550	±1.0

Figure A.1.: Preferred method for coarse tuning of the VECSEL frequency by rotating the BRF. A clean piece of plastic membrane is sticked over the large hatch on top of the laser head. The BRF can be rotated by ±10° with a 2 mm Allen key. The black mark shown on the picture indicates the original position.

A.2. Full Level Diagram of Dysprosium

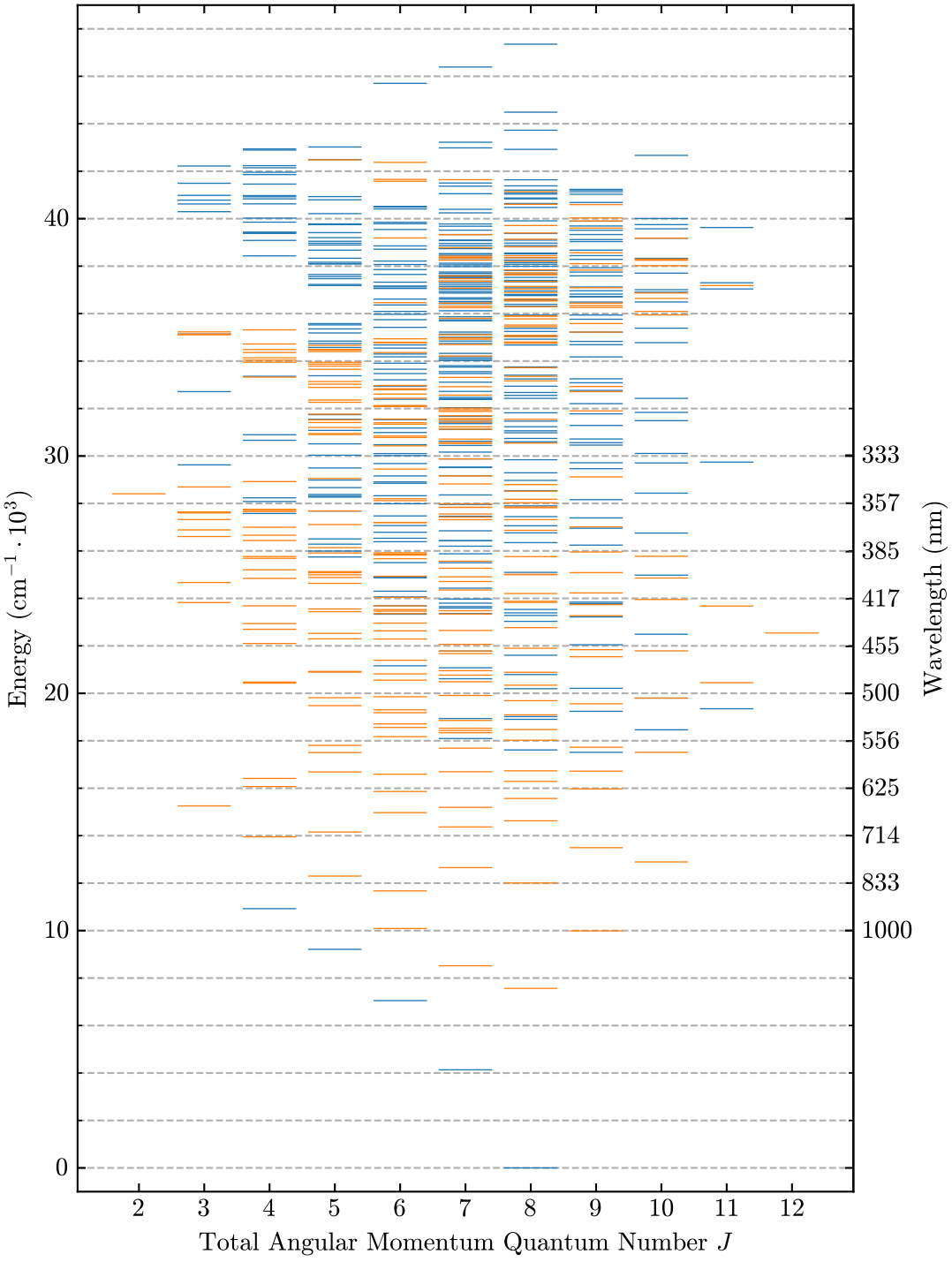

Figure A.2.: Dysprosium full level diagram. Levels with even (odd) parity are shown in blue (orange). All data, conveniently accessible via [55], has been taken from [53, 54].

A.3. Photographs of the Setup

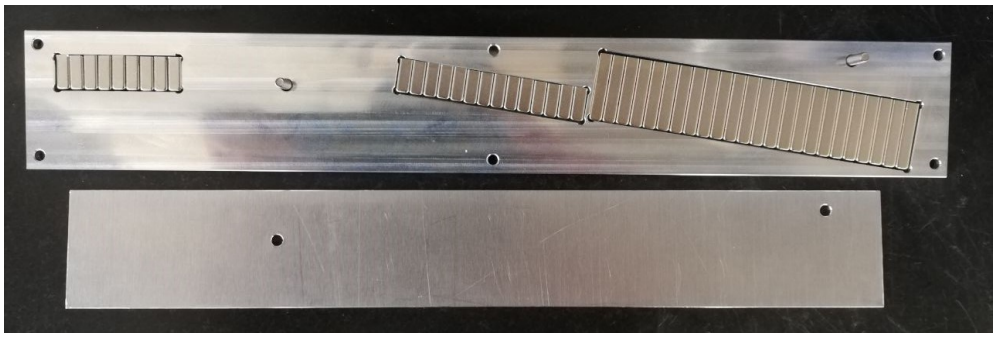

Figure A.3.: Permanent magnet holder. A total number of eight such holders are positioned around the vacuum tube to form the Zeeman slower. For reference see Fig.3.6.

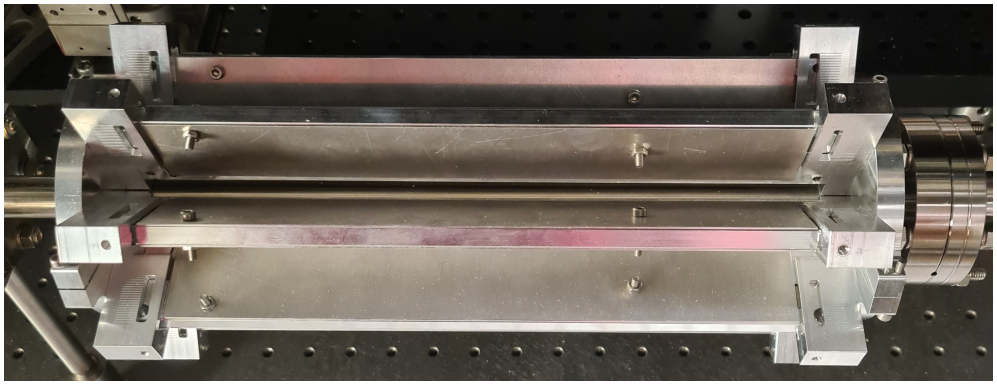

Figure A.4.: Side view of the Zeeman slower mounted on the vacuum apparatus. For reference see Fig. 3.6.

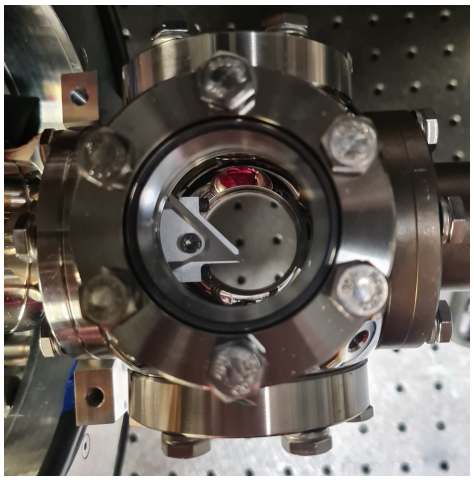

Figure A.5.: Top view of the vacuum chamber (cube 2). The in-vacuum mirror on a custom mount can be seen in the center of the chamber.

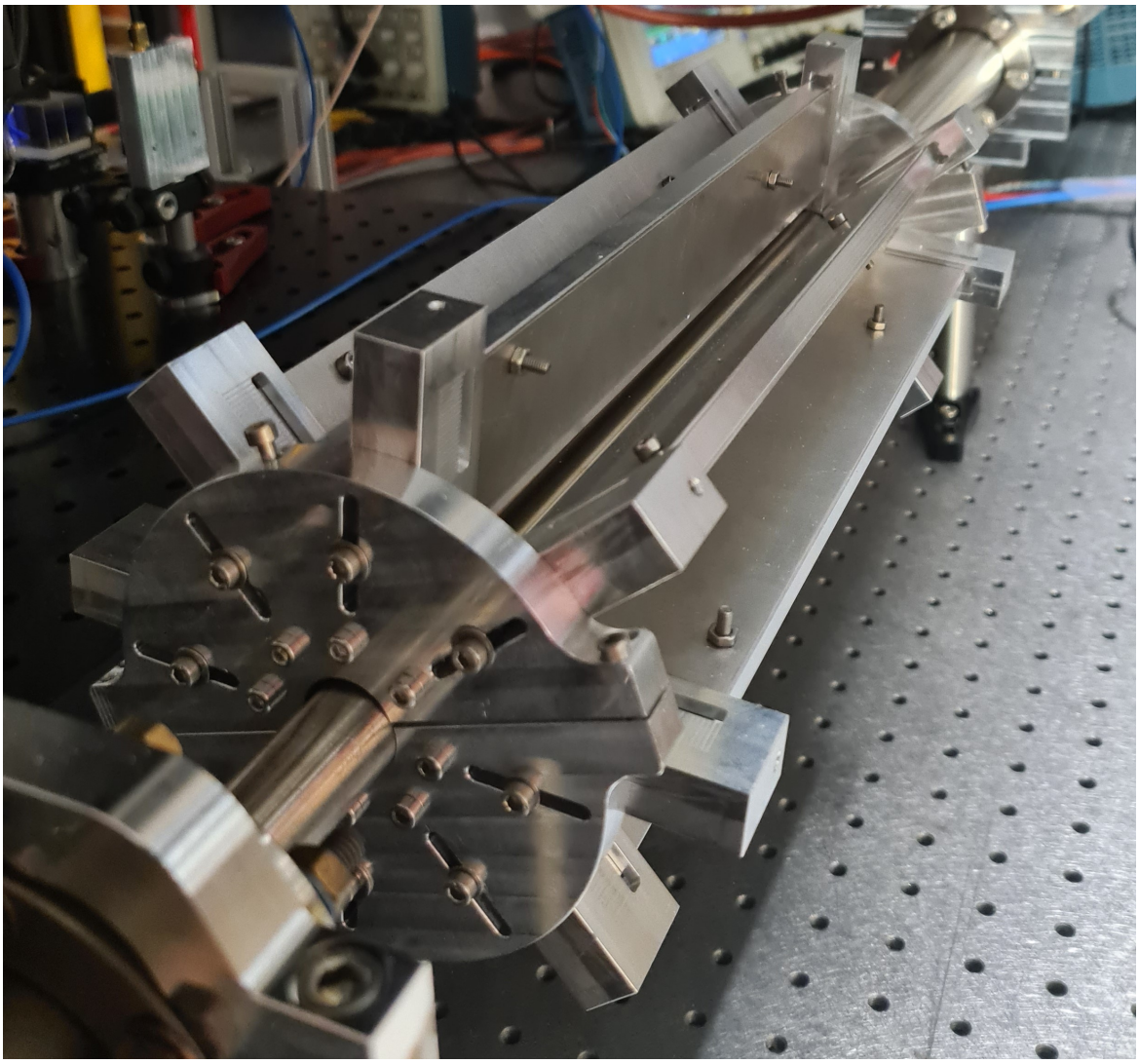

Figure A.6.: Front view of the Zeeman slower mounted on the vacuum apparatus. For reference see Fig. 3.6.

Bibliography

[1] R. P. Feynman. *Simulating physics with computers*. Int. J. Theor. Phys. 21 (1982), cit. on p. 1.

[2] S. V. Andreev, V. I. Balykin, V. S. Letokhov, and V. G. Minogin. *Radiative slowing and reduction of the energy spread of a beam of sodium atoms to 1.5K in an oppositely directed laser beam*. Pis'ma Zh. Eksp. Teor. Fiz. 34 (1981), cit. on p. 1.

[3] W. D. Phillips and H. Metcalf. *Laser deceleration of an atomic beam*. Phys. Rev. Lett. 48 (1982), cit. on p. 1.

[4] M. H. Anderson, J. R. Ensher, M. R. Matthews, C. E. Wieman, and E. A. Cornell. *Observation of Bose-Einstein Condensation in a Dilute Atomic Vapor*. Science 269 (1995), cit. on p. 1.

[5] K. B. Davis, M. O. Mewes, M. R. Andrews, N. J. van Druten, D. S. Durfee, D. M. Kurn, and W. Ketterle. *Bose-Einstein Condensation in a Gas of Sodium Atoms*. Phys. Rev. Lett. 75 (1995), cit. on p. 1.

[6] C. C. Bradley, C. A. Sackett, J. J. Tollett, and R. G. Hulet. *Evidence of Bose-Einstein Condensation in an Atomic Gas with Attractive Interactions*. Phys. Rev. Lett. 75 (1995), cit. on p. 1.

[7] C. C. Bradley, C. A. Sackett, and R. G. Hulet. *Bose-Einstein condensation of lithium: Observation of limited condensate number*. Phys. Rev. Lett. 78 (1997), cit. on p. 1.

[8] K. Aikawa, A. Frisch, M. Mark, S. Baier, A. Rietzler, R. Grimm, and F. Ferlaino. *Bose-Einstein Condensation of Erbium*. Phys. Rev. Lett. 108 (2012), cit. on p. 1.

[9] E. T. Davletov, V. V. Tsyganok, V. A. Khlebnikov, D. A. Pershin, D. V. Shaykin, and A. V. Akimov. *Machine learning for achieving Bose-Einstein condensation of thulium atoms*. Phys. Rev. A 102 (2020), cit. on p. 1.

[10] Y. Miyazawa, R. Inoue, H. Matsui, G. Nomura, and M. Kozuma. *Bose-Einstein Condensation of Europium*. Phys. Rev. Lett. 129 (2022), cit. on p. 1.

[11] S. Jochim, M. Bartenstein, A. Altmeyer, G. Hendl, S. Riedl, C. Chin, J. H. Denschlag, and R. Grimm. *Bose-Einstein Condensation of Molecules*. Science 302 (2003), cit. on p. 1.

[12] M. W. Zwierlein, C. A. Stan, C. H. Schunck, S. M. F. Raupach, S. Gupta, Z. Hadzibabic, and W. Ketterle. *Observation of Bose-Einstein Condensation of Molecules*. Phys. Rev. Lett. 91 (2003), cit. on p. 1.

[13] M. Greiner, C. A. Regal, and D. S. Jin. *Emergence of a molecular Bose–Einstein condensate from a Fermi gas*. Nature 426 (2003), cit. on p. 1.

[14] I. Fritsche, C. Baroni, E. Dobler, E. Kirilov, B. Huang, R. Grimm, G. M. Bruun, and P. Massignan. *Stability and breakdown of Fermi polarons in a strongly interacting Fermi-Bose mixture*. Phys. Rev. A 103 (2021), cit. on p. 1.

[15] C. Ravensbergen, E. Soave, V. Corre, M. Kreyer, B. Huang, E. Kirilov, and R. Grimm. *Resonantly Interacting Fermi-Fermi Mixture of* ^{161}Dy *and* ^{40}K. Phys. Rev. Lett. 124 (2020), cit. on p. 1.

[16] X. Zhou, W.-S. Lee, M. Imada, N. Trivedi, P. Phillips, H.-Y. Kee, P. Törmä, and M. Eremets. *High-temperature superconductivity*. Nat. Rev. Phys. 3 (2021), cit. on p. 1.

[17] C. Chin, R. Grimm, P. Julienne, and E. Tiesinga. *Feshbach resonances in ultracold gases*. Rev. Mod. Phys. 82 (2010), cit. on p. 2.

[18] L. Chomaz, I. Ferrier-Barbut, F. Ferlaino, B. Laburthe-Tolra, B. L. Lev, and T. Pfau. *Dipolar physics: a review of experiments with magnetic quantum gases*. Rep. Prog. Phys. 86 (2022), cit. on pp. 2, 5, 15.

[19] D. Barredo, H. Labuhn, S. Ravets, T. Lahaye, A. Browaeys, and C. S. Adams. *Coherent Excitation Transfer in a Spin Chain of Three Rydberg Atoms*. Phys. Rev. Lett. 114 (2015), cit. on p. 2.

[20] L. D. Carr, D. DeMille, R. V. Krems, and J. Ye. *Cold and ultracold molecules: science, technology and applications*. New J. Phys. 11 (2009), cit. on pp. 2, 14.

[21] I. Bloch, J. Dalibard, and S. Nascimbène. *Quantum simulations with ultracold quantum gases*. Nat. Phys 8 (2012), cit. on p. 2.

[22] F. Schäfer, T. Fukuhara, S. Sugawa, Y. Takasu, and Y. Takahashi. *Tools for quantum simulation with ultracold atoms in optical lattices*. Nat. Rev. Phys. 2 (2020), cit. on p. 2.

[23] S. Kuhr. *Quantum-gas microscopes: a new tool for cold-atom quantum simulators*. Natl. Sci. Rev. 3 (2016), cit. on p. 2.

[24] C. Gross and W. S. Bakr. *Quantum gas microscopy for single atom and spin detection*. Nat. Phys 17 (2021), cit. on p. 2.

[25] L. Asteria, H. P. Zahn, M. N. Kosch, K. Sengstock, and C. Weitenberg. *Quantum gas magnifier for sub-lattice-resolved imaging of 3D quantum systems*. Nature 599 (2021), cit. on p. 2.

[26] G. Anich, R. Grimm, and E. Kirilov. *Comprehensive Characterization of a State-of-the-Art Apparatus for Cold Electromagnetic Dysprosium Dipoles* (2023), cit. on p. 2.

[27] M. Lepers, H. Li, J.-F. m. c. Wyart, G. Quéméner, and O. Dulieu. *Ultracold Rare-Earth Magnetic Atoms with an Electric Dipole Moment*. Phys. Rev. Lett. 121 (2018), cit. on pp. 2, 5, 12.

[28] S. Jin, J. Gao, K. Chandrashekara, C. Gölzhäuser, J. Schöner, and L. Chomaz. *Two-dimensional magneto-optical trap of dysprosium atoms as a compact source for efficient loading of a narrow-line three-dimensional magneto-optical trap*. Phys. Rev. A 108 (2023), cit. on p. 3.

[29] W. D. Phillips. *Nobel Lecture: Laser cooling and trapping of neutral atoms*. Rev. Mod. Phys. 70 (1998), cit. on p. 3.

[30] C. Ravensbergen. *Creation of a Fermi-Fermi mixture of dysposium and potassium with resonant interactions*. PhD thesis. 2020, cit. on pp. 3, 51.

[31] Y. B. Ovchinnikov. *A permanent Zeeman slower for Sr atomic clock*. Eur. Phys. J. Spec. Top. 163 (2008), cit. on pp. 3, 23.

[32] E Wodey, R. J. Rengelink, C Meiners, E. M. Rasel, and D Schlippert. *A robust, high-flux source of laser-cooled ytterbium atoms*. J. Phys. B 54 (2021), cit. on p. 3.

[33] Y. B. Ovchinnikov. *Longitudinal Zeeman slowers based on permanent magnetic dipoles*. Opt. Commun. 285 (2012), cit. on pp. 3, 24, 26, 29.

[34] V Lebedev and D. M. Weld. *Self-assembled Zeeman slower based on spherical permanent magnets*. J. Phys. B 47 (2014), cit. on p. 3.

[35] H. Binder. *Lexikon der chemischen Elemente: das Periodensystem in Fakten, Zahlen und Daten*. Hirzel, 1999, cit. on pp. 5, 6.

[36] P. Patnaik. *Handbook of Inorganic Chemicals*. McGraw-Hill handbooks. McGraw-Hill, 2003, cit. on p. 5.

[37] M. Lu, N. Q. Burdick, S. H. Youn, and B. L. Lev. *Strongly Dipolar Bose-Einstein Condensate of Dysprosium*. Phys. Rev. Lett. 107 (2011), cit. on p. 5.

[38] Y. Zhang, J. R. G. Evans, and S. Yang. *Corrected Values for Boiling Points and Enthalpies of Vaporization of Elements in Handbooks*. J. Chem. Eng. Data 56 (2011), cit. on p. 6.

[39] M. C. Antoine. *Nouvelle Relation Entre les Tensions et les Temperatures*. C. r. held Seanc. Acad. Sci. Paris 107 (1888), cit. on p. 6.

[40] A. Frisch. *Dipolar quantum gases of erbium*. PhD thesis. 2014, cit. on p. 6.

[41] T. Maier. *Interactions in a Quantum Gas of Dysprosium Atoms*. PhD thesis. 2015, cit. on p. 6.

[42] D. D. Gray et al. *American Institute of Physics Handbook*. New York: McGraw-Hill, 1972, cit. on p. 7.

[43] J. R. de Laeter, J. K. Böhlke, P. D. Bièvre, H. Hidaka, H. S. Peiser, K. J. R. Rosman, and P. D. P. Taylor. *Atomic weights of the elements. Review 2000 (IUPAC Technical Report)*. Pure Appl. Chem. 75 (2003), cit. on p. 6.

[44] H. Haken and H. Wolf. *Atom- und Quantenphysik: Einführung in die experimentellen und theoretischen Grundlagen*. Springer-Lehrbuch. Springer Berlin Heidelberg, 2013, cit. on p. 7.

[45] M. Fox. *Quantum Optics: An Introduction*. Oxford Master Series in Physics. OUP Oxford, 2006, cit. on p. 8.

[46] B. R. Judd and I. Lindgren. *Theory of Zeeman Effect in the Ground Multiplets of Rare-Earth Atoms*. Phys. Rev. 122 (1961), cit. on p. 8.

[47] J. Schwinger. *On Quantum-Electrodynamics and the Magnetic Moment of the Electron*. Phys. Rev. 73 (1948), cit. on p. 8.

[48] J. Schwinger. *Quantum Electrodynamics. III. The Electromagnetic Properties of the Electron—Radiative Corrections to Scattering*. Phys. Rev. 76 (1949), cit. on p. 8.

[49] J. Ferch, W. Dankwort, and H. Gebauer. *Hyperfine structure investigations in DyI with the atomic beam magnetic resonance method*. Phys. Lett. A 49 (1974), cit. on pp. 8, 10.

[50] C. Foot. *Atomic Physics*. Oxford Master Series in Physics. OUP Oxford, 2005, cit. on pp. 9, 25.

[51] G. K. Woodgate. *Elementary Atomic Structure*. Oxford University Press, USA, 1980, cit. on p. 9.

[52] N. Leefer, A. Cingöz, and D. Budker. *Measurement of hyperfine structure and isotope shifts in the Dy 421 nm transition*. Opt. Lett. 34 (2009), cit. on pp. 10, 47.

[53] W. C. Martin, R Zalubas, and L Hagan. *Atomic Energy Levels - the Rare Earth Elements*. 1978, cit. on pp. 9, 11, 60.

[54] J. E. Sansonetti and W. C. Martin. *Handbook of Basic Atomic Spectroscopic Data*. J. Phys. Chem. Ref. Data 34 (2005), cit. on pp. 9, 11, 60.

[55] A. Kramida, Yu. Ralchenko, J. Reader, and NIST ASD Team. *NIST Atomic Spectra Database* (2022), cit. on pp. 11, 60.

[56] C. I. Hancox, S. C. Doret, M. T. Hummon, L. Luo, and J. M. Doyle. *Magnetic trapping of rare-earth atoms at millikelvin temperatures*. Nature 431 (2004), cit. on p. 10.

[57] N. A. Leefer, A. Cingöz, D. Budker, S. J. Ferrell, V. V. Yashchuk, A. Lapierre, A.-T Nguyen, S. K. Lamoreaux, and J. R. Torgerson. *Variation of the Fine-Structure Constant and Laser Cooling of Atomic Dysprosium*. In: *Frequency Standards and Metrology*. 2009, cit. on p. 10.

[58] M. Lu, S. H. Youn, and B. L. Lev. *Trapping Ultracold Dysprosium: A Highly Magnetic Gas for Dipolar Physics*. Phys. Rev. Lett. 104 (2010), cit. on p. 10.

[59] M. Lu, S. H. Youn, and B. L. Lev. *Spectroscopy of a narrow-line laser-cooling transition in atomic dysprosium*. Phys. Rev. A 83 (2011), cit. on pp. 10, 12.

[60] T. Maier, H. Kadau, M. Schmitt, A. Griesmaier, and T. Pfau. *Narrow-line magneto-optical trap for dysprosium atoms*. Opt. Lett. 39 (2014), cit. on p. 10.

[61] M. Gustavsson, H. Lundberg, L. Nilsson, and S. Svanberg. *Lifetime measurements for excited states of rare-earth atoms using pulse modulation of a cw dye-laser beam*. J. Opt. Soc. Am. 69 (1979), cit. on p. 12.

[62] D. Budker, D. DeMille, E. D. Commins, and M. S. Zolotorev. *Investigation of nearly degenerate opposite parity states in atomic dysprosium*. Phys. Rev. Lett. 70 (1993), cit. on p. 11.

[63] D. Budker, D. DeMille, E. D. Commins, and M. S. Zolotorev. *Experimental investigation of excited states in atomic dysprosium*. Phys. Rev. A 50 (1994), cit. on p. 11.

[64] N. Leefer, C. T. M. Weber, A. Cingöz, J. R. Torgerson, and D. Budker. *New Limits on Variation of the Fine-Structure Constant Using Atomic Dysprosium*. Phys. Rev. Lett. 111 (2013), cit. on p. 11.

[65] B. M. Roberts, Y. V. Stadnik, V. A. Dzuba, V. V. Flambaum, N. Leefer, and D. Budker. *Parity-violating interactions of cosmic fields with atoms, molecules, and nuclei: Concepts and calculations for laboratory searches and extracting limits*. Phys. Rev. D 90 (2014), cit. on p. 11.

[66] K. Van Tilburg, N. Leefer, L. Bougas, and D. Budker. *Search for Ultralight Scalar Dark Matter with Atomic Spectroscopy*. Phys. Rev. Lett. 115 (2015), cit. on p. 11.

[67] R. Jafari and A. Langari. *Phase diagram of the one-dimensional $S = \frac{1}{2}$ XXZ model with ferromagnetic nearest-neighbor and antiferromagnetic next-nearest-neighbor interactions*. Phys. Rev. B 76 (2007), cit. on p. 11.

[68] F. Pinheiro, G. M. Bruun, J.-P. Martikainen, and J. Larson. *XYZ Quantum Heisenberg Models with p-Orbital Bosons*. Phys. Rev. Lett. 111 (2013), cit. on pp. 11, 14.

[69] M. L. Wall, K Maeda, and L. D. Carr. *Realizing unconventional quantum magnetism with symmetric top molecules*. New J. Phys. 17 (2015), cit. on p. 11.

[70] V. A. Dzuba, V. V. Flambaum, and I. B. Khriplovich. *Enhancement of P- and T-nonconserving effects in rare-earth atoms*. Z. Phys. D. 1 (1986), cit. on p. 12.

[71] K.-K. Ni, S Ospelkaus, D Wang, G Quéméner, B. Neyenhuis, M. De Miranda, J. Bohn, J. Ye, and D. Jin. *Dipolar collisions of polar molecules in the quantum regime*. Nature 464 (2010), cit. on p. 12.

[72] A. Frisch et al. *Ultracold Dipolar Molecules Composed of Strongly Magnetic Atoms*. Phys. Rev. Lett. 115 (2015), cit. on p. 12.

[73] M. Obertegger. *Building a STIRAP Laser for Opposite Parity States in Dysprosium*. Master's thesis. 2020, cit. on p. 13.

[74] S. A. Moses, J. P. Covey, M. T. Miecnikowski, B. Yan, B. Gadway, J. Ye, and D. S. Jin. *Creation of a low-entropy quantum gas of polar molecules in an optical lattice*. Science 350 (2015), cit. on p. 14.

[75] J. W. Park, S. A. Will, and M. W. Zwierlein. *Ultracold Dipolar Gas of Fermionic* ^{23}Na^{40}K *Molecules in Their Absolute Ground State*. Phys. Rev. Lett. 114 (2015), cit. on p. 14.

[76] T. Takekoshi, L. Reichsöllner, A. Schindewolf, J. M. Hutson, C. R. Le Sueur, O. Dulieu, F. Ferlaino, R. Grimm, and H.-C. Nägerl. *Ultracold Dense Samples of Dipolar RbCs Molecules in the Rovibrational and Hyperfine Ground State*. Phys. Rev. Lett. 113 (2014), cit. on p. 14.

[77] P. K. Molony, P. D. Gregory, A. Kumar, C. R. Le Sueur, J. M. Hutson, and S. L. Cornish. *Production of Ultracold 87Rb133Cs in the Absolute Ground State: Complete Characterisation of the Stimulated Raman Adiabatic Passage Transfer*. ChemPhysChem 17 (2016), cit. on p. 14.

[78] F. Seeßelberg, X.-Y. Luo, M. Li, R. Bause, S. Kotochigova, I. Bloch, and C. Gohle. *Extending Rotational Coherence of Interacting Polar Molecules in a Spin-Decoupled Magic Trap*. Phys. Rev. Lett. 121 (2018), cit. on p. 14.

[79] M. Guo, B. Zhu, B. Lu, X. Ye, F. Wang, R. Vexiau, N. Bouloufa-Maafa, G. Quéméner, O. Dulieu, and D. Wang. *Creation of an Ultracold Gas of Ground-State Dipolar* ^{23}Na^{87}Rb *Molecules*. Phys. Rev. Lett. 116 (2016), cit. on p. 14.

[80] A. W. Glaetzle, M. Dalmonte, R. Nath, C. Gross, I. Bloch, and P. Zoller. *Designing Frustrated Quantum Magnets with Laser-Dressed Rydberg Atoms*. Phys. Rev. Lett. 114 (2015), cit. on p. 14.

[81] R. M. W. van Bijnen and T. Pohl. *Quantum Magnetism and Topological Ordering via Rydberg Dressing near Förster Resonances*. Phys. Rev. Lett. 114 (2015), cit. on p. 14.

[82] S. Whitlock, A. W. Glaetzle, and P. Hannaford. *Simulating quantum spin models using Rydberg-excited atomic ensembles in magnetic microtrap arrays*. J. Phys. B 50 (2017), cit. on p. 14.

[83] X. Wu, X. Liang, Y. Tian, F. Yang, C. Chen, Y.-C. Liu, M. K. Tey, and L. You. *A concise review of Rydberg atom based quantum computation and quantum simulation**. Chin. Phys. B 30 (2021), cit. on p. 14.

[84] T. L. Nguyen et al. *Towards Quantum Simulation with Circular Rydberg Atoms*. Phys. Rev. X 8 (2018), cit. on p. 14.

[85] M. Lewenstein, A. Sanpera, V. Ahufinger, B. Damski, A. Sen(De), and U. Sen. *Ultracold atomic gases in optical lattices: mimicking condensed matter physics and beyond*. Adv. Phys. 56 (2007), cit. on p. 14.

[86] Y. Tang, W. Kao, K.-Y. Li, and B. L. Lev. *Tuning the Dipole-Dipole Interaction in a Quantum Gas with a Rotating Magnetic Field*. Phys. Rev. Lett. 120 (2018), cit. on p. 15.

[87] S. A. Will, J. W. Park, Z. Z. Yan, H. Loh, and M. W. Zwierlein. *Coherent Microwave Control of Ultracold* ^{23}Na^{40}K *Molecules*. Phys. Rev. Lett. 116 (2016), cit. on p. 15.

[88] T. Karman, Z. Z. Yan, and M. Zwierlein. *Resonant and first-order dipolar interactions between ultracold* $^1\Sigma$ *molecules in static and microwave electric fields*. Phys. Rev. A 105 (2022), cit. on p. 15.

[89] K. J. Ross and B. Sonntag. *High temperature metal atom beam sources*. Rev. Sci. Instrum. 66 (1995), cit. on p. 18.

[90] Dr. Eberl MBE-Komponenten GmbH. *Standard Effusion Cell WEZ - Datasheet*. URL: `https://www.mbe-komponenten.de/products/pdf/data-sheet-wez.pdf`, cit. on pp. 18, 19.

[91] A. König. *Characterization of a new dual-species atomic source for lithium and potassium*. Master's thesis. 2022, cit. on pp. 19, 21.

[92] N. Ramsey. *Molecular Beams*. International series of monographs on physics. OUP Oxford, 1985, cit. on pp. 20, 22.

[93] H. C. W. Beijerinck and N. F. Verster. *Velocity distribution and angular distribution of molecular beams from multichannel arrays*. J. Appl. Phys. 46 (1975), cit. on pp. 20, 21.

[94] J. Coey and S. Parkin. *Handbook of Magnetism and Magnetic Materials*. Handbook of Magnetism and Magnetic Materials. Springer International Publishing, 2021, cit. on p. 27.

[95] *HKCM Engineering*. Accessed: 2023-03-30. URL: `https://www.hkcm.de`, cit. on p. 28.

[96] *Eclipse Magnetics*. Accessed: 2023-03-30. URL: `https://www.eclipsemagnetics.com/`, cit. on p. 28.

[97] H. Kohlmann, T. C. Hansen, and V. Nassif. *Magnetic structure of SmCo5 from 5 K to the Curie temperature*. Inorg. Chem. 57 (2018), cit. on p. 28.

[98] *SDM Magnetics*. Accessed: 2023-03-30. URL: `https://www.magnet-sdm.com/sm2co17-magnet/`, cit. on p. 28.

[99] S. P. Krzyzewski, T. G. Akin, P. Dahal, and E. R. I. Abraham. *A clip-on Zeeman slower using toroidal permanent magnets*. Rev. Sci. Instrum. 85 (2014), cit. on p. 29.

[100] Z. Yang, T. Johansen, H Bratsberg, G Helgesen, and A. Skjeltorp. *Potential and force between a magnet and a bulk Y1Ba2Cu3O7-δ superconductor studied by a mechanical pendulum*. Supercond. Sci. Technol. 3 (1990), cit. on p. 29.

[101] P. Virtanen et al. *SciPy 1.0: Fundamental Algorithms for Scientific Computing in Python*. Nat. Methods 17 (2020), cit. on p. 31.

[102] R. H. Byrd, P. Lu, J. Nocedal, and C. Zhu. *A limited memory algorithm for bound constrained optimization*. SIAM J. Sci. Comput. 16 (1995), cit. on p. 31.

[103] A. D. Ludlow, M. M. Boyd, J. Ye, E. Peik, and P. O. Schmidt. *Optical atomic clocks*. Rev. Mod. Phys. 87 (2015), cit. on p. 43.

[104] B. Chéron, H. Gilles, J. Hamel, O. Moreau, and H. Sorel. *Laser frequency stabilization using Zeeman effect*. J. Phys. III France 4 (1994), cit. on p. 43.

[105] K. L. Corwin, Z.-T. Lu, C. F. Hand, R. J. Epstein, and C. E. Wieman. *Frequency-stabilized diode laser with the Zeeman shift in an atomic vapor*. Appl. Opt. 37 (1998), cit. on p. 43.

[106] T. Hansch and B. Couillaud. *Laser frequency stabilization by polarization spectroscopy of a reflecting reference cavity*. Opt. Commun. 35 (1980), cit. on p. 43.

[107] C. P. Pearman, C. S. Adams, S. G. Cox, P. F. Griffin, D. A. Smith, and I. G. Hughes. *Polarization spectroscopy of a closed atomic transition: applications to laser frequency locking*. J. Phys. B 35 (2002), cit. on p. 43.

[108] G. C. Bjorklund, M. Levenson, W Lenth, and C Ortiz. *Frequency modulation (FM) spectroscopy*. Appl. Phys. B 32 (1983), cit. on p. 43.

[109] J. L. Hall, L. Hollberg, T. Baer, and H. G. Robinson. *Optical heterodyne saturation spectroscopy*. Appl. Phys. Lett. 39 (1981), cit. on p. 43.

[110] J. H. Shirley. *Modulation transfer processes in optical heterodyne saturation spectroscopy*. Opt. Lett. 7 (1982), cit. on p. 43.

[111] D. J. McCarron, S. A. King, and S. L. Cornish. *Modulation transfer spectroscopy in atomic rubidium*. Meas. Sci. Technol. 19 (2008), cit. on p. 43.

[112] B. Smaller. *Precise Determination of the Magnetic Moment of the Deuteron*. Phys. Rev. 83 (1951), cit. on p. 43.

[113] Ducloy, M. and Bloch, D. *Theory of degenerate four-wave mixing in resonant Doppler-broadened media. - II. Doppler-free heterodyne spectroscopy via collinear four-wave mixing in two- and three-level systems*. J. Phys. France 43 (1982), cit. on p. 44.

[114] *Vexlum LTD*. Accessed: 2023-07-03. URL: `https://vexlum.com/`, cit. on p. 48.

Acknowledgements

On these final pages in concluding my thesis, it is both a tradition and my own heartfelt wish to express my deepest gratitude to those who have made this project possible. Especially given that this work evolved into a much larger and more intricate endeavor than initially anticipated, their unwavering support and guidance have been invaluable. I want to thank Rudi Grimm, who once enthused me to change my major to physics, took us on international adventures and finally welcomed me in his group for my Bachelor and now Master thesis. Apart from his profound understanding of physics and his ability to explain complex phenomena in an intuitive and understandable way, Rudi has always kept our backs free from financial hurdles and provided us with all the infrastructure we could wish for. At the same time I want to thank Emil Kirilov, for taking me under his wings from an early stage on, supervising my work and providing me with most of the practical knowledge I gained so far on my journey of becoming an experimental physicist. Despite being the probably most hard working and busiest person I know, he was always there to give me a hand whilst teaching me pitfalls and tricks not to be found in any textbook.

I also want to thank Marian Kreyer for being the patient recipient of even my most foolish questions and for reading my manuscript at the climbing crag while preparing for another attempt on his project. His honest advice has been an invaluable compass for me and my work, even though he probably thinks I never listen to him anyway. Likewise I dearly want to thank the Dy-K team for providing me with laser light, precious lab equipment and advise on how to use it. I also want to thank the FeLiKx team and especially Isabella Fritsche and Erich Dobler for introducing me to my first high-power laser and fluorescence spectroscopy respectively. Special thanks also goes to the general staff of both the institute of experimental physics and the IQOQI for enabling most of the hardware components and electronics. I also thank Verena Tanzer and Christine Götsch-Obmascher for their kindness and a level of organization that is second to none.

Last, but definitely not least I am immensely grateful for my family and friends, who have accompanied me through all the highs and lows of being a physics student. A complete list of all those involved would go beyond the scope of this acknowledgement. Many thanks to all members of the Master Stammtisch who have concurrently shown

me that I am not alone, even in times of great hardship, and, in particular, to Michael Weinreich, whose humor, enthusiasm and calmness made even the most tedious lectures enjoyable. Thank you for pushing me through even the most intense whiteboard sessions and preparations for theoretical physics exams. A very special thanks goes to my parents Christa and Georg, who gifted me a loving home and encouraged me from an early age that knowledge is a valuable asset. Your inherent and steadfast support has enabled me to go my own way right from the very beginning. Finally I would like to express my sincere appreciation and love to my partner, Vero. Throughout this journey, she has been my unwavering companion, a source of inspiration, and a relentless taskmaster, who managed to turn my procrastination into productivity so that she could show me what living in Innsbruck really means.

Thank you very much.